Improving the Resolution and Sensitivity of Microwave Astronomical Observations

by

Felix Maximilian Thiel

A thesis submitted to the Graduate Program in Physics,
Engineering Physics and Astronomy in conformity with the
requirements for the Degree of

Masters of Science

Queen's University

Kingston, Ontario, Canada

September, 2023

Abstract

Millimetre and microwave astronomy has been an ever-expanding field over the past decades with an improvement in computational power, semi-conductors, super-conductors and readout electronics. This has led to more powerful and sensitive instruments as well as higher resolutions for both single-dish and interferometric observations. In this work I will be giving an overview of my work on one current and one future experiment: TolTEC, a millimetre-wave camera with polarization capabilities on the Large Millimetre Telescope in Mexico currently undergoing commissioning, in particular designing the TolTEC Fields and Filaments survey and BVEX, a K-band balloon-borne Very Long Baseline Interferometry (VLBI) station where I will be presenting my design and sensitivity requirements for the K-band receiver. While TolTEC will deliver science-ready maps of the linear Stokes parameters I, Q, and U in the short term, BVEX will serve as a proof of concept and stepping stone for a future generation VLBI experiment capable of millimetre and sub-millimetre wavelengths.

Co-Authorship

The TolTEC software stack `tolteca` and data reduction pipeline `citlali`, which I used extensively for my work in Ch. 3 and 4 were written by Zhiyuan Ma and Michael McCrackan at the University of Massachusetts Amherst. The priors for TolTEC simulations in Sec. 4.2 were taken from Betti et al. 2021 and Qian et al. 2015 while the priors for the Fields in Filaments simulations in Sec. 3.1.3 were provided by Akanksha Bij (Bij 2022). The results for TolTEC observations of 3C 286 presented in Ch. 4 were compiled by Hailin Wang at Northwestern University. The `minkasi` reductions of M1 were done by Joey Golec, the pointing reduction of M1 which I used for my `citlali` M1 science reductions as well as the creation of array property tables using beammap reductions were done by Michael McCrackan.

Acknowledgements

First and foremost I would like to thank Laura Fissel my supervisor for all her amazing input and patience. I would also like to thank the entire TolTEC collaboration in particular Zhiyuan Ma and Michael McCrackan (UMass) for answering all my questions regarding software usage, as well as Joey Golec (UMichigan) for sharing his `minkasi` reductions with the entire collaboration. I would further like to thank the polarization group at Northwestern University for their input in particular Giles Novak, Dennis Lee and Hailin Wang.

I would also like to thank the BVEX Collaboration in particular Vincent Fish and Ganesh Rajagopalan at MIT/Haystack who have been extremely helpful in laying out the science requirements and receiver design for BVEX.

Last but not least I would like to thank all the members of the QStar team especially fellow students Akanksha Bij, who provided the priors for my TolTEC simulations, and Mayukh Bagchi for being such a great BVEX collaborator.

Contents

List of Figures

List of Tables

Chapter 1

Introduction: Where the Radio meets the Infrared

Observations at millimetre wavelengths have a wide range of applications in astrophysics and cosmology from the Sunyaev-Zel'Dovich effect (Planck Collaboration 2016b) to star-formation (Planck Collaboration 2016c) to the observation of black-hole shadows (Event Horizon Telescope Collaboration 2019; Event Horizon Telescope Collaboration 2022). Millimetre-wavelength observations have properties both typical to the radio spectrum and the far-infrared-spectrum.

Similar to the radio spectrum, we are still operating at diffraction limited resolution

$$\theta \approx \frac{\lambda}{d} \tag{1.1}$$

where λ is the wavelength and d is the size of the primary optics. As implied by Eq. 1.1 we can improve the resolution of our observations by increasing the size of the telescope dish. Due to mechanical constraints there is a limit to the dish size and we therefore have to resort to interferometry to improve our resolution where d in Eq. 1.1 is replaced by the longest baseline between stations. While the resolution is greatly increased, large spatial scales are resolved out based on the closest spacing between stations, making single dish observations an important complimentary measurement. In the millimetre and sub-millimetre, Very Long Baseline Interferometry (VLBI) becomes an extremely powerful tool to resolve small scales as has most recently been demonstrated by the Event Horizon Telescope (EHT) Collaboration (Event Horizon Telescope Collaboration 2019; Event Horizon Telescope Collaboration 2022).

While millimetre and sub-millimetre observations benefit from the diffraction limit defined in Eq. 1.1, they are strongly affected by atmospheric 1/f-noise (Choi et al. 2020 and references therein) which is very dominant in the far-infrared. The combined power spectrum (PSD) of 1/f noise and white noise is dependent on the post-detection frequency f via a power law

$$PSD(f) = C\left(1 + \left(\frac{f_k}{f}\right)^{\alpha}\right) \tag{1.2}$$

where C is the white-noise level, α the spectral index and f_k is the so-called "knee-frequency", which determines the frequency at which the noise appears to be white. As implied by Eq. 1.2, variations therefore are bigger at low frequencies (long time scales) than at high frequencies (short time scales). These time scales map into spatial scales through the telescope scan speed and the noise seen in the map therefore depends on the scan speed. Removing these atmospheric effects requires extensive post-observational processing that affects the recovered spatial scales in total intensity measurements (see Sec. 3.1.2). Therefore at millimetre wavelengths any ground-based total-intensity observation will be spatially filtered.

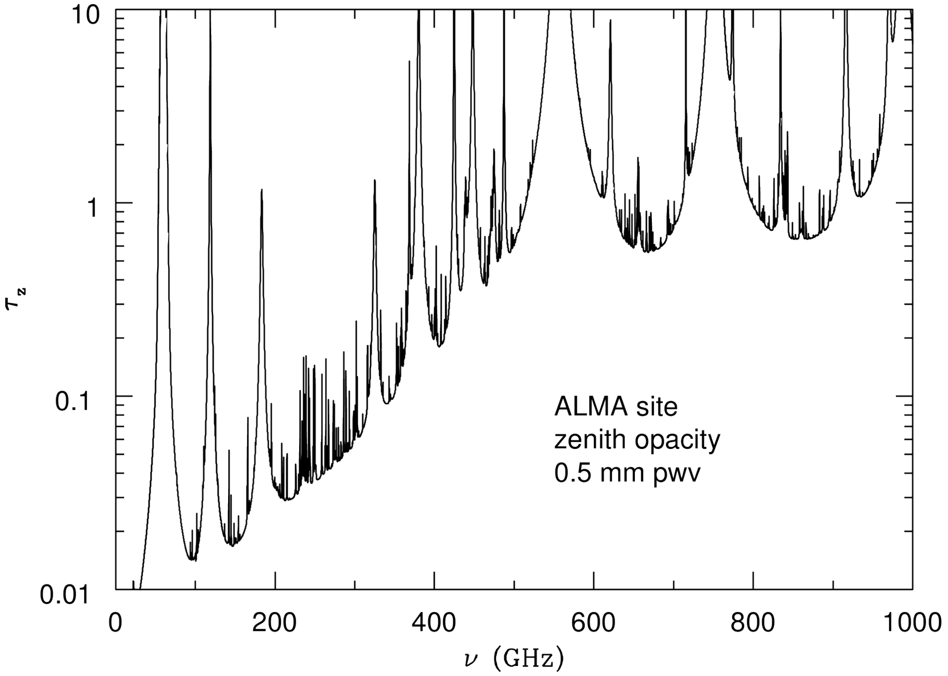

Figure 1.1: Zenith opacity as a function of frequency at the Atacama Large Millimetre Array (ALMA) site in Chile. The higher the zenith opacity the lower the atmospheric transmission. The sharp increases in opacity are due to molecular (water vapour and other species) absorption lines. (Reproduced with permission from: Condon et al. 2016, using data from `https://almascience.eso.org/about-alma/weather/atmosphere-model`)

As shown in Fig. 1.1 there are only few windows that allow for ground-based observations due to the presence of water vapor in our atmosphere from very few locations on Earth. While we can make significant hardware improvements for polarimetric observations, in total intensity this can only be achieved by either using large detector arrays (like the future CCATprime telescope, CCAT-Prime Collaboration 2023) or operating from a near-space environment like BLAST/BLASTPOL (Fissel 2013; Fissel et al. 2016; Pascale et al. 2012) or outer-space like *Herschel* and *Planck*.

The same way that observations at these wavelengths exhibit characteristics from both the far-infrared and radio, we also use backends (i.e the part of the telescope that converts incident light to electronic signals that can be recorded) from both of these portions of the electromagnetic spectrum. For single-dish observations we typically use incoherent detectors (i.e. detectors that measure optical power) which are commonly used in the far-infrared. Examples of these include bolometers in the case of SCUBA-2 on the JCMT (Holland et al. 2013) or Kinetic Inductance detectors (KIDs) that are used on the new NIKA-2 instrument on the IRAM 30 m telescope (Catalano et al. 2014). These detectors have the advantage that we can easily place multiple detectors into a focal plane array increasing the field of view and hence the mapping efficiency, in a regime where the beam size is a few arcseconds. However, for performing interferometry, we need to measure wave-forms and must therefore use heterodyne receivers (see Fig. 5.4) which are backends typically used in the radio spectrum. While heterodyne instruments are extremely useful for spectral line measurements with interferometers and single-dish telescopes alike, due to their high spectral resolutions, they are rather impractical for single-dish continuum observations due to their narrow bandwidths and physical size, restricting the field-of-view to a few beamsizes at most.

The aim in millimetre and sub-millimetre astronomy has been to on one hand improve the resolution of observations and to fill spatial scales that have not been covered by telescopes in the past, and on the other to continuously improve the mapping efficiency by increasing the size of detector arrays and the sensitivity by pushing into the stratospheric/suborbital regime. In this work I will be presenting two experiments that will address the above challenges. One of these experiments is TolTEC which is a new instrument on the Large Millimetre Telescope (LMT) currently undergoing commissioning, and the other is BVEX a balloon-borne VLBI station that is set to launch in the Summer of 2025. For TolTEC, the goal of this thesis was to determine the best mapping strategies for the Fields in Filaments survey using synthetic observations, and to study the expected loss in spatial scales. I will also be presenting some of my analysis on TolTEC commissioning data. For BVEX the goal was to design the K-band receiver and determine the sensitivity requirements for the experiment. I will start by giving an overview of TolTEC and the Fields in Filaments Survey in Ch. 2, then I will continue by presenting my design of the Fields in Filaments survey and TolTEC synthetic observations in Ch. 3, followed by an overview of my analysis on TolTEC commissioning data in Ch. 4. Following this discussion on TolTEC I will be wrapping up this work with a presentation of my K-band receiver design for BVEX in Ch. 5.

Chapter 2

TolTEC and the Fields in Filaments Survey

In this chapter I will be giving an overview of the new TolTEC camera as well as the 100 hour Fields in Filaments Survey, and finally the TolTEC software stack `tolteca` and data-reduction pipeline `citlali` written by Zhiyuan Ma and Michael McCrackan (Ma et al. 2020; McCrackan et al. 2022), which was used to create and reduce synthetic TolTEC observations in Ch. 3.

2.1 The TolTEC Camera

The TolTEC Camera (see Fig. 2.1 for a schematic) is a new instrument on the LMT in Mexico, that observes at three bands, 1.1, 1.4, and 2.0 mm using three arrays that are made up of a total of 7716 polarization-sensitive KIDs (Lunde et al. 2020). Unlike heterodyne radio receivers these detectors measure power rather than the electric field, which allow us to build large detector arrays that can easily be read out increasing the field-of-view and mapping efficiency. This also means that the frequency response of the instrument will be set by the optical elements in the instrument rather than the electronics. This is done using a set of dichoric mirrors, optical elements that transmit one type of wavelength and reflect another and generally have a higher bandwidth (about 50 GHz for TolTEC as shown in Fig. 2.2) than heterodyne radio receivers (see Fig. 5.4).

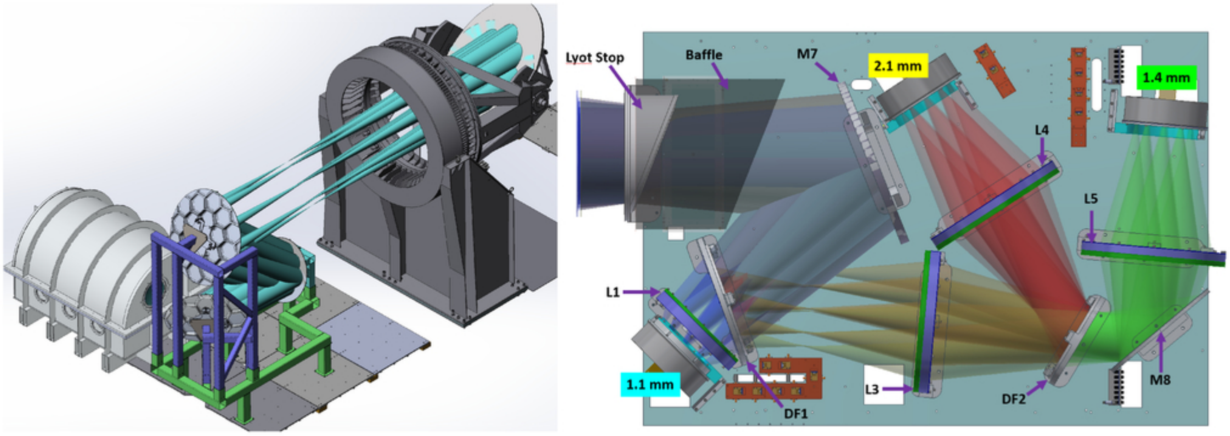

(a) Warm optics.

(b) Cold optics.

Figure 2.1: *Left*: Location of the TolTEC cryostat and the room temperature ("warm") optics in the LMT's receiver cabin in relation to the Nasmyth mount. *Right*: Set up of the TolTEC cryostat. The light enters the cryostat through the top left and is then split into the three bands by the dichroics (DF1 and DF2). These are then detected by the three detector arrays. The continuously rotating half-wave-plate (not shown) is located just outside the cryostat window. (Reproduced with permission from: Lunde et al. 2020)

Because KIDs are superconducting detectors, they have to be cooled to about 100 mK, and hence there are two types of optics for TolTEC. The "warm" optics are located outside the cryostat directing the light from the Cassegrain focus of the telescope to the cryostat as shown in the left panel of Fig. 2.1, and the "cold" optics inside the cryostat which split the incident light into the three TolTEC bands and focus it onto the three detector arrays, using a set of dichroic mirrors and lenses as shown in the right-hand panel of Fig. 2.1. Together

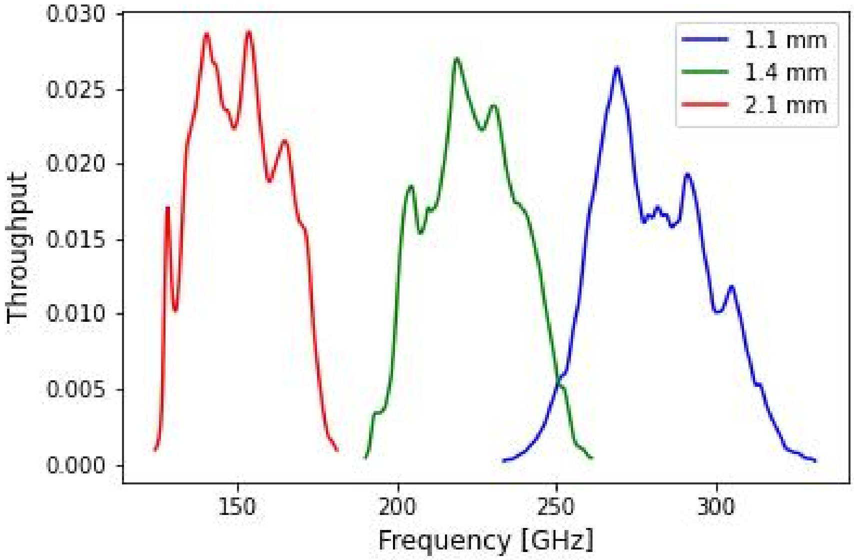

Figure 2.2: TolTEC pass-bands as measured by Nat DeNigris in the laboratory at UMass Amherst. The plots were made using data from Ma 2022. The bandwidth for each band amounts to about 50 GHz.

with the 50-m dish of the LMT, TolTEC will have an unprecedented resolution of 5″ at 1.1 mm and 9″ at 2mm. A detailed overview of the beamsizes, numbers of detectors and projected mapping speeds can be found in Tbl. 2.1.

Band	Beamsize	Detectors	Lower Mapping Speed	Upper Mapping Speed
1.1 mm	5″	4012	2 $\text{deg}^2/\text{mJy}^2/\text{hr}$	12 $\text{deg}^2/\text{mJy}^2/\text{hr}$
1.4 mm	6.3″	2532	3 $\text{deg}^2/\text{mJy}^2/\text{hr}$	20 $\text{deg}^2/\text{mJy}^2/\text{hr}$
2.0 mm	9.5″	1172	10 $\text{deg}^2/\text{mJy}^2/\text{hr}$	69 $\text{deg}^2/\text{mJy}^2/\text{hr}$

Table 2.1: Projected beam sizes and mapping speeds of TolTEC. All mapping speeds assume an atmospheric opacity of 0.5 at 225 GHz. The bandpass response for TolTEC is shown in Fig. 2.2 (`http://toltec.astro.umass.edu/about.php`)

TolTEC will be able to measure the astrophysical signal not only in total intensity (Stokes I) but also the linear Stokes parameters Q and U defined as

$$Q = \langle E_x^2 \rangle - \langle E_y^2 \rangle \tag{2.1}$$

$$U = \langle E_a^2 \rangle - \langle E_b^2 \rangle \tag{2.2}$$

where E_x and E_y are the electric fields in the x-direction (or 0° or north/south in equatorial coordinates) and y-direction (or 90° or east/west in equatorial coordinates) respectively. Similarly, E_a and E_b are the electric fields in the 45° and $-45°$ directions. Angular brackets denote time averages. Unlike the definitions in Eqs. 2.1,2.2 which have units of $\mathrm{V}^2/\mathrm{m}^2$, astronomical Stokes parameters are measured in units of flux (i.e. MJy/sr or mJy/beam). TolTEC measures these Stokes parameters through the use of antenna-coupled detectors at four different orientations, where signals from orthogonal detectors are then subtracted from each other during data reduction. In order to mitigate atmospheric 1/f noise and to make weak polarized sources detectable, TolTEC uses a continuously rotating half-wave-plate (CRHWP), sitting on a set of air-bearings that reduce friction. This has the effect of modulating the polarized sky signal at 4Ω (8 Hz for TolTEC) where Ω is the rotation frequency (2 Hz for TolTEC) of the CRHWP, effectively shifting it to post-detection frequencies beyond the knee-frequency (typically a lot less than 1 Hz), where the noise levels are effectively white (Lee et al. 2022; Lunde et al. 2020).

TolTEC will conduct four legacy surveys: Two related to cosmology (the Large Scale Structure Survey and the Ultra-Deep Survey of Star-forming Galaxies), and two surveys related to star-formation. One of these is the Clouds to Cores survey which will aim at better studying the relation between the inital-mass-function and the core-mass-function, and the other is the Fields in Filaments Survey.

2.2 The Fields in Filaments Survey

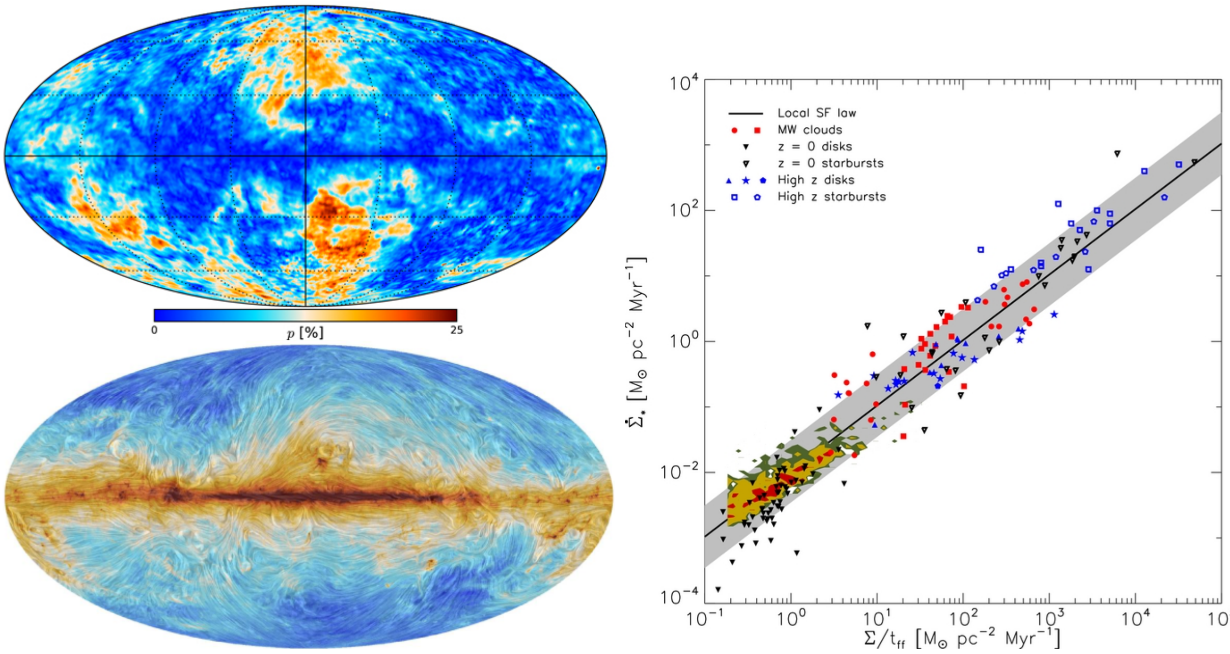

Figure 2.3: *Top Left: Planck* Galactic Map of the polarization fraction at 353 GHz (850 μm) the polarization fraction is low in the galactic plane compared to higher galactic latitudes amounting to at most 5% in star-forming regions (Reproduced with permission from Planck Collaboration 2020). *Bottom Left*: The Galactic magnetic field orientaion as measured by *Planck* at 353 GHz superimposed on a total intensity map (Reproduced with permission from Planck Collaboration 2016a). *Right*: The observed star-formation rate as a function of the gas surface density per free-fall time for different galaxies and Milky-Way molecular clouds. The slope of the graph represents the star-formation efficiency per free-fall time amounting to about 1% (Reproduced with permission from: Krumholz et al. 2012).

Star-formation is an incredibly inefficient process (see Fig. 2.3) only converting about 1% of the interstellar gas into stars per free fall time (Kennicutt 1989; Krumholz et al. 2012). Furthermore simulations demonstrate that the usual mechanisms such as thermal pressure and turbulent pressure don't fully account for the unusually low star-formation rate (Federrath 2015; Li et al. 2019). Thermal dust-emission polarization observations such as those of the Planck satellite (see Fig. 2.3) have shown that the Galactic plane is threaded by magnetic fields, which in turn have the effect of slowing gravitationally collapsing gas

(Planck Collaboration 2016a; Federrath 2015; Li et al. 2019). While there is an abundance of simulations (Federrath 2015; Li et al. 2019) studying the effect of magnetic fields on star formation there is a lack of high-resolution observations tracing the cold phases of the interstellar medium and early stages of star-formation.

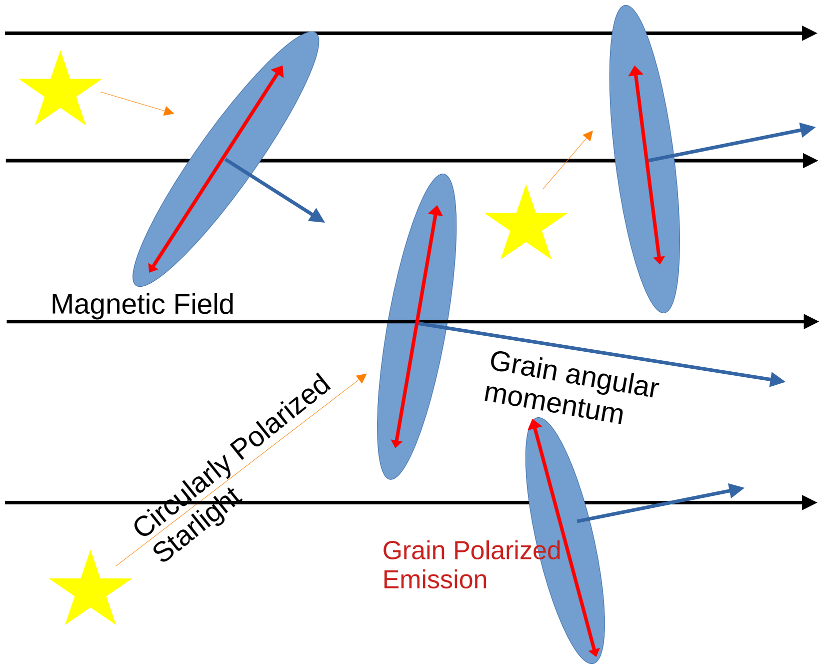

Figure 2.4: High-level diagram of dust alignment mechanism inside the interstellar magnetic field as described in Lazarian 2007 and Andersson et al. 2015. Circularly polarized light from the local radiation field (orange yellow) causes the interstellar dust grains (blue) to spin super-thermally around their minor axis (which corresponds to the lowest energy state preserving angular momentum). These radiative torques will cause an alignment of the angular momentum (blue arrows) with the local magnetic field (black arrows) over time. This alignment results in polarized dust emission perpendicular to the magnetic field (red arrows) due to directional dust opacities.

The lack of observations is mainly due to the way the magnetic field can be studied. Because the magnetic field is a vector quantity we would like to measure the magnitude and the orientation. The line-of-sight magnitude of the interstellar magnetic field can be determined two ways. Either by observing Zeeman-splitting of OH and CN lines (Crutcher et al. 2010;

Crutcher 2012),or through the observation of Faraday rotation of synchrotron radiation at long radio wavelengths (Simard-Normandin et al. 1980; Tahani et al. 2018 and references therein). The former requires a vast amount of telescope time to make a significant detection and we can therefore only make individual sight-line detections rather than extended maps (Crutcher et al. 2010; Crutcher 2012), while the ladder requires assumptions on the electron density (Simard-Normandin et al. 1980).

Measuring the POS magnetic field orientation however is a lot simpler by using the fact that interstellar dust grains will spin around their minor axis due to radiative torques from the local radiation field causing an alignment of the rotation axis with the local magnetic field as shown in Fig. 2.4. This in turn produces a dust opacity that is higher perpendicular to the magnetic field than parallel to the magnetic field resulting in polarized dust emission perpendicular to the magnetic field (Lazarian 2007; Andersson et al. 2015). Therefore, by measuring the polarization angle defined as

$$\chi = \frac{1}{2}\arctan\left(\frac{U}{Q}\right) \tag{2.3}$$

where U and Q are the Stokes parameters defined in Eqs. 2.1 and 2.2, we can then infer the plane-of-sky magnetic field orientation averaged over the volume of the telescope beam by applying a 90 degree rotation. Furthermore, together with a measurement in total intensity we can determine the polarization fraction

$$p = \frac{\sqrt{Q^2 + U^2}}{I} = \frac{P}{I} \tag{2.4}$$

where Q and U again are the Stokes parameters in Eqs. 2.1 and 2.2 and I is the total intensity. The numerator can be grouped into a single term P which is called the polarized intensity. The polarization fraction can be used to probe dust composition and polarization efficiency (Hensley et al. 2023). While measuring the orientation of the magnetic field is significantly easier than the magnitude, it imposes stringent sensitivity requirements on observations as the polarization fraction typically amounts to less than 5% at submillimetre and millimetre wavelengths in the interstellar medium (Planck Collaboration 2020, also see Fig. 2.3). Since dust emission is best observed at sub-millimetre and millimetre wavelengths atmospheric noise adds another challenge to observations. While the magnitude of the interstellar magnetic field is a more direct measure, the orientation also gives the observer useful information. For instance, under the assumption that the ionization fraction of interstellar gas is high enough, and that the local magnetic field dominates over gravity and turbulence, interstellar gas flows will be constrained to move along the magnetic field (Nakamura et al. 2008). Therefore, the magnetic field can give valuable information on the direction from which star-forming cores accrete material.

The majority of star-formation happens in dense cylindrical structures of gas and dust called filaments (André et al. 2014; Pineda et al. 2022). Dense filaments (with hydrogen column densities greater than $10^{21.7}$ cm^{-2}) tend to align perpendicular to the magnetic field, suggesting a gravity dominated gas flow onto the filament (Fissel et al. 2019,Planck Collaboration 2016c). Most recently, there have also been indicators that on smaller sub-filamentary scales the magnetic field starts aligning parallel to the ridges of the filament, again suggesting gas flows towards dense protostellar cores the progenitors of stars (Arzoumanian et al. 2021). While there are some observations of this effect, more high-resolution data are required to perform a more detailed study. Moreover the critical density and length scale where gravitational collapse dominates over magnetic support is yet to be determined mainly due to a lack of high-resolution polarization data.

The TolTEC camera on the LMT will have almost 3 times the resolution of existing polarimeters, for example, POL-2/SCUBA-2 (850 μm) on the JCMT has $14''$ resolution, and the HAWC+ polarimeter (214 μm) on SOFIA had $18''$ resolution. TolTEC will therefore have sufficient resolution to image nearby star-forming regions on sub-filamentary (<0.1 pc) scales. For instance, in nearby star-forming regions such as B211/213 in Taurus at a distance of 140 pc, TolTEC will be able to resolve structures that are 700 AU in size at 1.1 mm. Hence, TolTEC is the ideal instrument to perform the Fields in Filaments Legacy survey a 100 hour survey mapping nearby star-forming and infrared-dark filaments (see Tbl. 2.2) in total intensity (Stokes I) and the linear Stokes parameters Stokes Q and U. This survey will help answering the question of when gravity dominates over the magnetic field and the effect of the magnetic field on the evolution of star-forming filaments. On top of this it will also provide well needed publicly available data that bridges the gap in spatial scales between the resolution of the *Planck* satellite and the largest angular scale of the Atacama Large

Target	Distance (pc)	Total Time (h)
Serpens South	430	20
B211/213 in Taurus	140	24
B1 in Perseus	290	20
OMC 2 and 3	414	10
Rho Ophiuchus C, E and F	137	12
Snake Filament	3300	10
Milky Way Bone Candidate 5	2400	5.1

Table 2.2: List of all the targets for the 100 h Fields in Filaments legacy survey as well as their distances and total time on target (`http://toltec.astro.umass.edu/science_bfields.php`).

Millimetre Array (ALMA).

2.3 Detector Readout

As mentioned in Sec. 2.1 the TolTEC camera uses three arrays of so-called KIDs. This very new kind of detector as opposed to a heterodyne radio receiver measures power rather than electric field. A KID can be thought of as a superconducting LC-resonator circuit (a circuit that is mostly sensitive to one frequency) that changes its resonance frequency as a function of incident optical power. Therefore, by determining the shift in the resonance frequency we can determine the change in optical power seen by the telescope.

In practice, the shift in the resonance frequency is determined through the measurement of the scattering parameter

$$S_{21} = \mathcal{I} + i\mathcal{Q} \tag{2.5}$$

where $\mathcal{I}$ and $\mathcal{Q}$ are the in-phase and quadrature components of the signal, that is the real and complex parts of the KID output signal (not to be confused with the Stokes parameters). Before observation, a so-called “frequency” or “Vector Network Analyzer (VNA)” sweep is performed at known optical loading on each KID to determine the KID-model

$$S_{21}(f_p) = G\tilde{S}_{21}(f_p; f_r, Q_r) + Kf_p + M \tag{2.6}$$

where f_p is the probing frequency, G,K and M are complex parameters that depend on the read-out circuit and

$$\tilde{S}_{21} = \frac{Q_r}{1 + 2iQ_r\frac{f_p - f_r}{f_r}} \tag{2.7}$$

where Q_r is the quality factor (a measure of how broad the resonance is) and f_r is the resonance frequency of the KID. The S_{21} is recorded at different probing frequencies and is then fit to the model in Eq. 2.6 and all the parameters and data are stored to disk. The detectors are grouped into so-called networks in which all the detectors (usually about 600) are read out at the same time. The 1.1 mm array is divided into 7 networks, the 1.4mm array into 4 and the 2.0 mm array into 2 networks (Ma et al. 2020; Lunde et al. 2020). A detailed overview of the TolTEC array morphology can be seen in Fig. 2.5

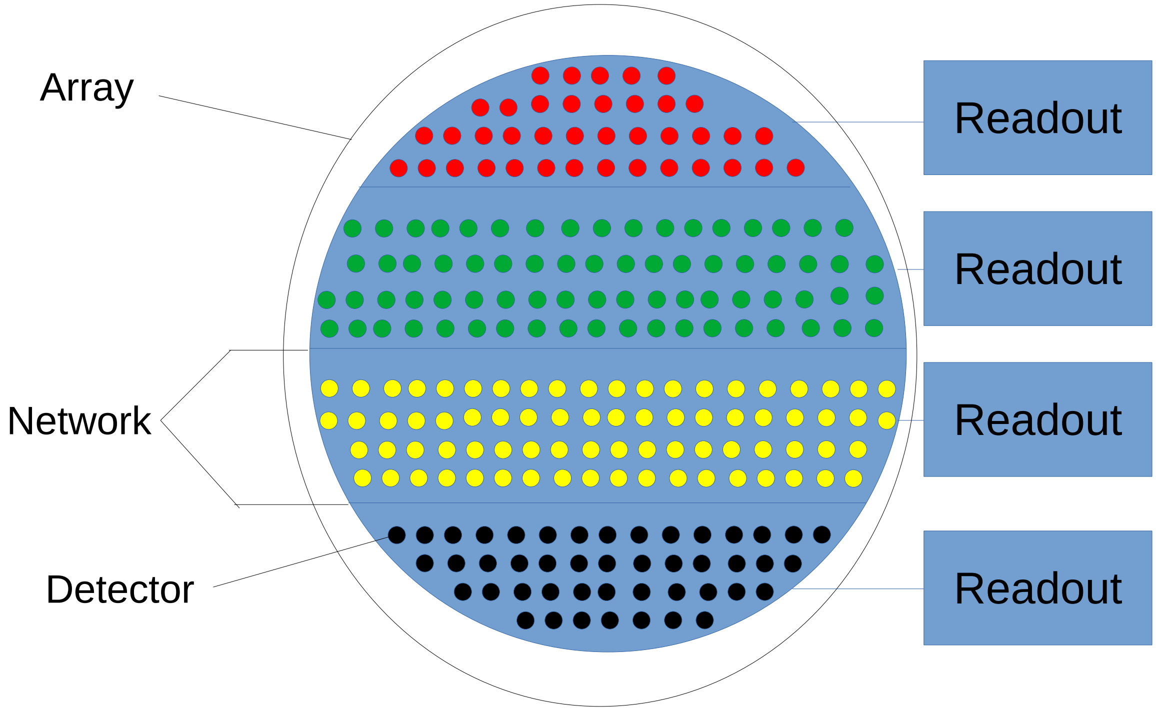

Figure 2.5: Morphology of a TolTEC focal plane array. For reading out data the array is divided into slices called networks (color-coded). Detectors of the same network are then part of the same readout, through frequency domain multiplexing.

When observing, all the KIDs are then probed with a frequency comb containing all the resonance frequencies determined in the frequency sweep and the S_{21} is recorded as a function of time for each detector and saved to disk for further processing. These data are from here on referred to as an S_{21} time-stream. In order to get this into a unit proportional to flux we make use of the parameter

$$X = \tilde{S}_{21}^{-1} = r + xi \tag{2.8}$$

where

$$r = \frac{1}{2Q_r} \tag{2.9}$$

and

$$x = \frac{f_p - f_r}{f_r} \tag{2.10}$$

which is also known as the detuning parameter and is a quantity proportional to the optical loading. The S_{21} time-streams together with the model in Eq. 2.6 as determined by the frequency sweep can then be used to determine the detuning parameter in Eq. 2.10 (Ma et al. 2020).

2.4 Data Reduction

In order to turn the time-streams from the instrument into science-ready maps three more data-items are needed. The first is the telescope pointing which is recorded as a function of time by the telescope computer. Secondly, we need to determine the relative position of each detector to the telescope bore-sight (i.e. the pointing the telescope would have if it had a single beam) in order to recover the individual detector pointing. This is done in so-called beammap observations which consist of making maps in azimuth and elevation for each detector of a bright point source. These are then used to measure the source offset from telescope bore-sight giving the detector offset. Furthermore this also allows us to determine the conversion factor between the detuning parameter and source flux in mJy/beam. All this information is then stored in a table referred to as the array property table (APT) (Ma et al. 2020; McCrackan et al. 2022). Lastly, for polarization observations the orientation of the HWP is also stored in order to demodulate the polarized signal later in the reduction process (Lee et al. 2022; McCrackan et al. 2022).

In order to facilitate the planning and reduction of TolTEC observations we use the python-based package `tolteca` (Ma et al. 2020). This package has two main functionalities, a simulator (which will be described in more detail in Ch. 3) and a reduction function, which gathers all the relevant file paths and reduction parameters in a high-level configuration file and places these in a low-level file which is then passed to the C++-based data reduction pipeline `citlali` (Ma et al. 2020,McCrackan et al. 2022). All in all, `citlali` takes five inputs: The low-level configuration file from `tolteca`, the raw S_{21} time-streams, the APT, the telescope pointing file and the half-wave-plate file which contains the angle of the CRHWP. The overall workflow of the data-reduction pipeline can be divided into two steps: time-stream processing and map-making.

2.4.1 Time-stream Processing

The first step in the data reduction process involves taking the raw S_{21} time-stream and solving for the X parameter defined in Eq. 2.8 using Eq. 2.6 together with the frequency sweep data. The imaginary part of these solved time-streams will be given by the detuning parameter x in Eq. 2.10, which is proportional to the flux.

In the case of reducing the data in polarization mode the time streams of adjacent orthogonal detector pairs (there are four orientations in total 0°, 45°, 90° and 135°) are differenced and demodulated (as in Novak et al. 1989) to determine the Stokes parameters in the frame of the instrument and are then rotated from the telescope reference frame into the International Celestial Reference System (ICRS) frame. In the case where data are reduced in total intensity only, no demodulation and rotation is performed.

Next, the time stream is de-spiked to remove any effect of cosmic rays striking the detectors. After this the timestreams are low-pass filtered, due to the fact that the LMT has a maximum scanning speed. Signals above the post-detection frequency associated with that scanning speed are not of cosmic origin and therefore should be filtered. Similarly we can also choose to high-pass filter the signal at this stage to remove low-frequency noise. Before passing to the final stage, of atmospheric cleaning the time-stream is down-sampled as the sampling rate of 488 Hz is more than sufficient to fully sample the beam. At the same time, this helps in reducing the computational time during atmospheric removal.

Lastly, for total intensity, the atmosphere is removed using Principle Component Analysis (PCA), where the covariance matrix is computed across a group of detectors. Typically the grouping is done by network, however, for the newest version of `citlali` which is compatible with real TolTEC data, detectors can also be grouped by array. This covariance matrix is then diagonalized to get the eigenvalues (also referred to as eigenmodes or principle components). Assuming that the atmospheric signal dominates, we expect the largest eigenmodes to approximate the atmospheric contribution. Therefore, the dominant eigenmodes are zeroed out. The number of eigenmodes that are removed are set by the user. PCA will not be applied to polarized time-streams because a major portion of the signal is removed by Eqs. 2.1 and 2.2 and due to the fact that the atmosphere is mostly unpolarized. Any residual 1/f is expected to be mitigated by modulating the polarized signal using the CRHWP (Lee et al. 2022).

In order to track the effect of time-stream-processing on an unresolved point-source after polarization demodulation, `citlali` generates a set of time streams that map out a point-source in the same way the actual signal is mapped. All data cuts that are applied to the real signal are also applied to the fake signal (also referred to as the kernel). This kernel can then be used to correct for the loss in point-source flux.(McCrackan et al. 2022)

2.4.2 Map-making

The current implementation of `citlali` only includes a so-called naive mapmaker. This mapmaker uses the telescope pointing file to assign each sample in the time-stream a map pixel, that it is binned into. Therefore each pixel then represents the weighted average of all time-ordered-data (TOD) samples in that bin.

For astronomical observations it often is the case that data are taken in batches over the course of several nights for efficient time-allocation and due to long integration times, which is why `citlali` also includes a co-addition routine which takes maps from different observing nights and computes a weighted average. After all the maps have been created there also is an option to apply a Wiener filter to the finished maps to remove any pixel-to-pixel noise.

Once the map-making stage is finished Flexible Image Transport System (FITS) images for each of the three TolTEC bands are written to disk containing signal maps, weights (inverse of the variance), signal-to-noise ratios, and coverage maps for total intensity, Stokes Q and U (McCrackan et al. 2022).

Chapter 3

TolTEC simulations

In this section I will be giving an overview of preparatory work that I have done for the Fields in Filaments survey, such as designing mapping strategies and testing the pipeline for bugs. The Fields and Filaments survey requires both total intensity and Stokes Q/U maps to determine the polarization fraction (Eq. 2.4) and angle (Eq. 2.3) and it is therefore important to study both.

3.1 Simulations and Surveying Strategies

In order to facilitate the planning of observations with TolTEC the software package `tolteca` (written by Zhiyuan Ma, Ma et al. 2020) also includes a simulator function to create synthetic observations of prospective targets. This simulator function takes as input a configuration file which sets all the simulation parameters such as sampling rate mapping patterns, atmospheric models, and a FITS image of the target to be observed. The simulator returns outputs of similar format as the real instrument, which can then be fed into the data-reduction pipeline `citlali`, to recover the signal. This allows us to study the effect of mapping strategies, atmospheric filtering and map-making but also facilitates the debugging effort (Ma et al. 2020). On top of this there also is an online observation tool (the TolTEC ObsPlanner[1]) available to generate simulator configuration files as well as observing scripts for the telescope control system (TCS).

3.1.1 Mapping patterns

When making observations at millimetre wavelengths in total intensity, the main consideration when choosing a mapping pattern is the effect of atmospheric noise which follows a 1/f profile as in Eq. 1.2. This implies that atmospheric variations on large time-scales are worse than on short time scales. These time-scales are mapped into spatial scales via the scan speed. If the scan speed is high, then the sky-noise predominantly maps into large spatial scales (which may be comparable to the map size) giving a lower root-mean-square (RMS) along the scan-direction than at slow scan-speeds. This dependence on the scan speed also implies that noise becomes directional in the map, making the directionality of the pattern another consideration. Generally speaking, when making total intensity maps we want a fast and non-directional mapping-pattern (Kovács 2008).

For polarization observations with the CRHWP, atmospheric noise is mitigated by default making the directionality of the pattern less important. The main consideration here is to ensure proper modulation of the beam while scanning. For the Fields in Filamnents survey we set a threshold of at least three power modulation cycles per TolTEC beam at 1.1mm. The CRHWP rotates at a frequency of 2 Hz giving a modulation frequency of 8 Hz. Therefore,

---

[1] `https://toltec.lmtgtm.org/toltec_obs_planner`

the requirement of modulating the beam three times gives an upper-bound for the scan speed of 13 arcsec/s. Given this bound different mapping patterns will have to be used for total intensity and polarization observations.

Other considerations for mapping patterns include desired map size and coverage (i.e. where the data points in the map are located). As it stands right now there are four different mapping patterns for the LMT, the lissajous, the double lissajous, the raster scan, and the rastajous scan.

The Lissajous

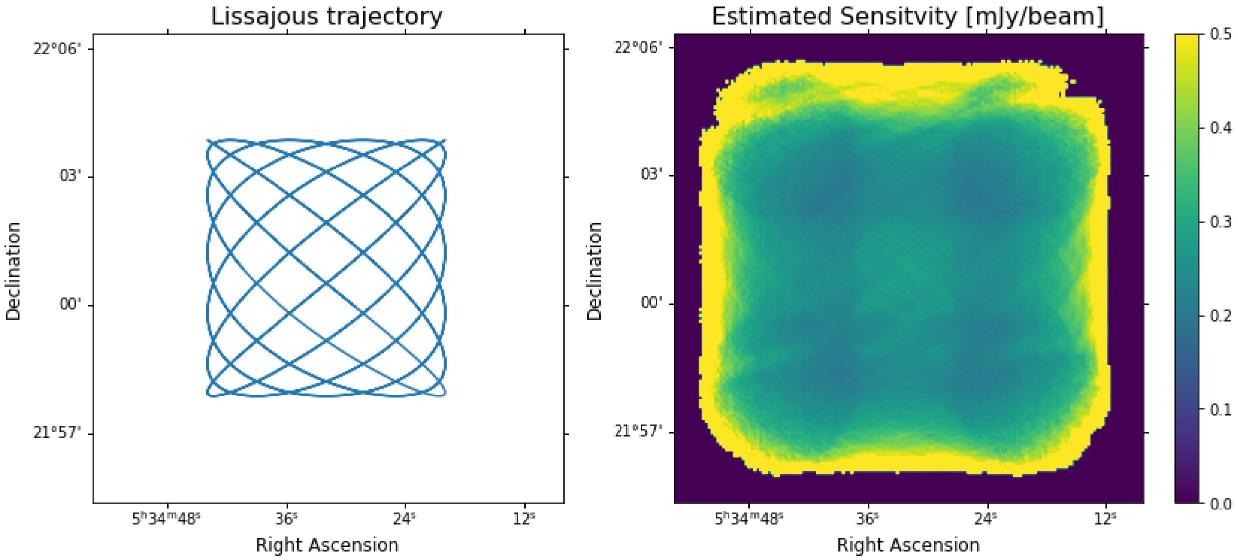

Figure 3.1: *Left:* Trajectory of a $6' \times 6'$ lissajous in the RA/DEC coordinate frame, only the first 15 seconds are plotted out. *Right:* Map RMS in mJy/beam as estimated by the TolTEC ObsPlanner for a 10 minute pattern. The drop in sensitivity at the centre of the map arises from the fact that the telescope spends most of its time at the corners, hence the lower RMS in the 4' lobes at the corners. If the pattern size is decreased to less than or equal to the field of view the corners overlap giving uniform coverage.

The Lissajous (depicted in Fig. 3.1, also see Kovács 2008) is a mapping pattern with a trajectory parameterized by two sines which are slightly out of phase, where the x and y coordinates as a function of time are given by

$$\begin{cases} x = A\sin(\omega_1 t + \phi) \\ y = B\sin(\omega_2 t) \end{cases} \tag{3.1}$$

where A and B are the amplitudes and correspond to half the dimensions of the map, ω_1 and ω_2 are the angular frequencies of the sine, and ϕ is the phase offset. The ratio of the two angular frequencies determines how tightly the Lissajous is woven. Because the Lissajous essentially behaves like a harmonic oscillator the scan-speed is not constant and is bounded from above by

$$v_{max} = \sqrt{(A\omega_1)^2 + (B\omega_2)^2}. \tag{3.2}$$

Therefore, the maximum scan speed increases with map area. Furthermore, this implies that the telescope will spend more time at the edges of the map than at the centre, giving low coverage in the middle of the map and a lot of coverage at the edge of the map as shown in Fig. 3.1. This mapping pattern should therefore only be used for regions that are less than or of order the field-of view (FOV) which is about $4'$ in diameter for TolTEC. Nonetheless, the low directionality of this mapping strategy and the high scan speeds make it a favorable mapping pattern to use for small-scale total intensity maps.

The Double Lissajous

As the name implies the double Lissajous (see Fig. 3.2) scan is parameterized by the sum of a major and a minor Lissajous as follows:

$$\begin{cases} x = A_0 \sin(\omega_{x0} t + \phi + \phi_0) + A_1 \sin(\omega_{x1} t + \phi_1) \\ y = B_0 \sin(\omega_{y0} t + \phi) + B_1 \sin(\omega_{y1} t) \end{cases} \tag{3.3}$$

where A_0, A_1, B_0 and B_1 are the x and y amplitudes of the major and minor patterns respectively, ω_{x0}, ω_{x1}, ω_{y0} and ω_{y1} are the angular frequencies of the patterns. The phase offsets ϕ_0 and ϕ_1 are the x-y phase offsets for the major and minor patterns respectively and ϕ is the phase offset between the major and the minor patterns.

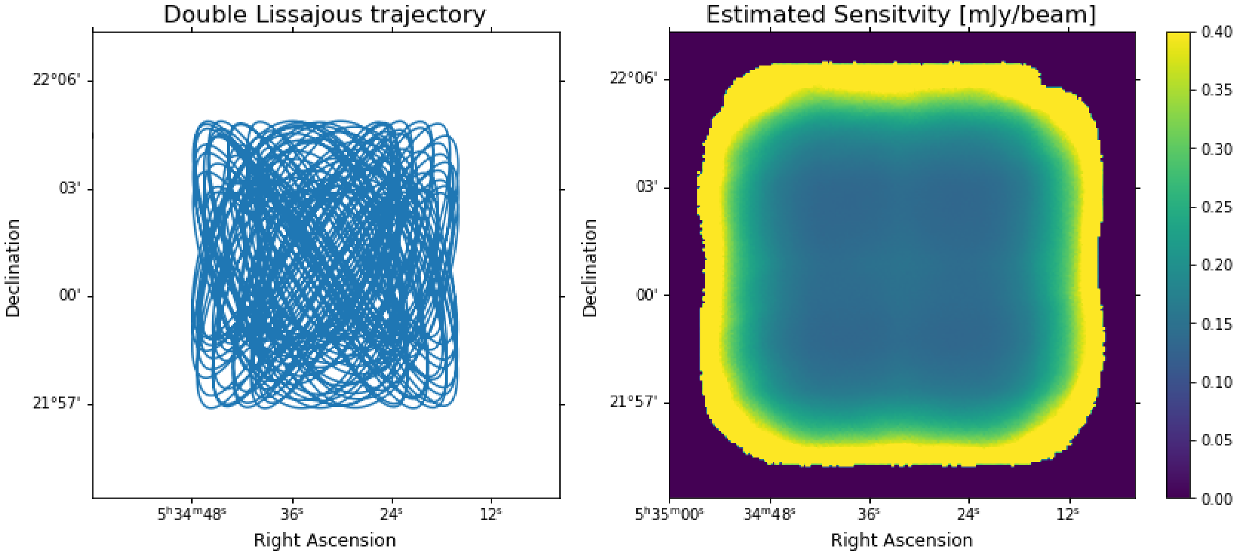

Figure 3.2: *Left*: The first 100 s of a double Lissajous scan with a $6' \times 6'$ major pattern and a $2' \times 2'$ minor pattern. *Right*: Expected sensitivity for a 30 minute total intensity double lissajous scan as computed by the TolTEC ObsPlanner. The coverage is more uniform over an extended area than for the lissajous scan, nonetheless there still is a slight drop in the coverage at the centre of the map.

The main advantage of this pattern is that through the addition of another Lissajous the coverage gets more uniform for bigger map-sizes, however not uniform enough for large-scale maps. The other advantage of this pattern is that it is less directional than the Lissajous which helps in reducing 1/f-noise. All in all, the Lissajous and double Lissajous mapping patterns should therefore only be used for small intensity maps. Since polarization scans with the CRHWP require a slow and steady pattern for proper beam modulation Lissajous scans should not be used for this kind of observation.

The Raster Scan

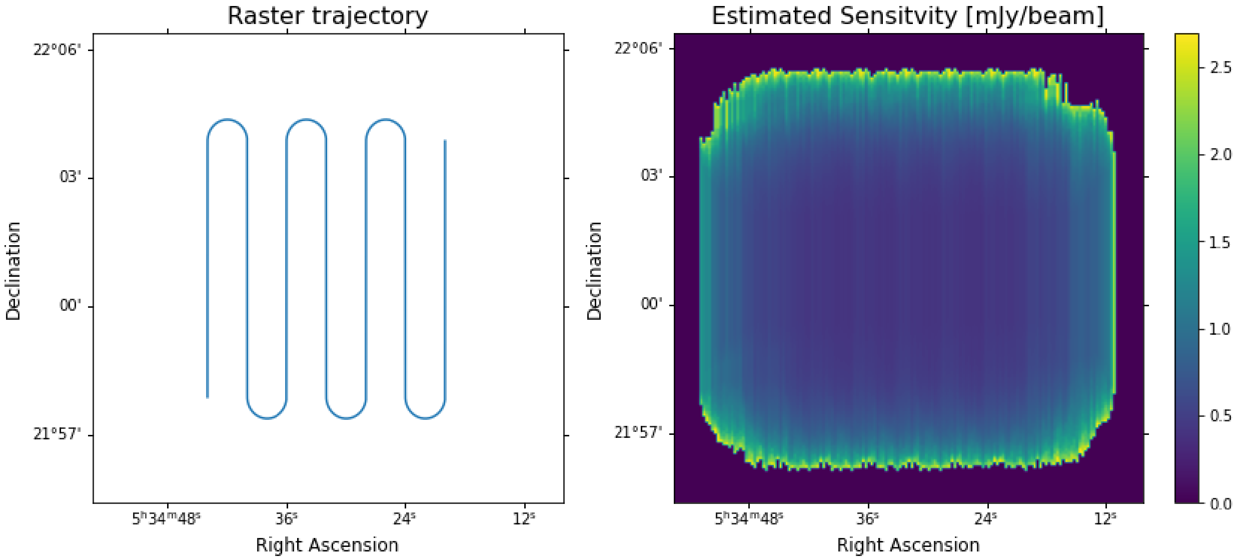

Figure 3.3: *Left*: Trajectory of a $6' \times 6'$ vertical raster scan with a $1'$ spacing the data at the turnarounds are discarded in the map-making process. *Right*: Estimated polarized sensitivity for an 8 arcsec/s raster scan using the trajectory on the left. The streaking in the RMS is due to dark or inactive detectors in the array. For a real observation one would coadd vertical and horizontal scans.

The third mapping pattern used by TolTEC is the raster scan, which is the most commonly used scanning strategy for large scale intensity mapping in cosmological surveys (Irfan et al. 2023). For this strategy, the region of interest is scanned keeping one coordinate fixed while moving in the other coordinate at some constant scan speed v for some scan length L.

This is then repeated until the map is completed using a scan spacing Δy. An example of this can be seen in Fig. 3.3

The main advantage of the raster scan is the more or less uniform coverage in the region of interest. For total intensity, however it is favorable to move the telescope as fast as possible to mitigate the effect of 1/f noise. For small and medium-sized maps this would result in a lot of co-addition to bring up the effective integration time rendering this strategy impractical. This is the reason why this pattern often only is used to map large square-degree sized fields. The other challenge with this pattern is the fact that it is uni-directional. For instance, the average scan speed in Fig. 3.3 along the RA direction is 8 arcsec/s while the average scan speed along the DEC direction is 1.3 arcsec/s (not accounting for turnaround). This means that the noise experienced perpendicular to the scan direction will be worse than noise parallel to the scan direction manifesting itself as streaks along the scan direction. This effect can be reduced but not completely eliminated by coadding raster scans in different directions.

For polarization measurements with the CRHWP however, the directionality of the pattern no longer is a problem due to the absence of 1/f noise. In this case the pattern becomes favorable to use because of its steady and easy to control scan speed giving good beam modulation.

The Rastajous Pattern

So far in this section we have touched on two types of patterns: Lissajous patterns which become extremely useful for small total-intensity maps due to their high scan speeds and non-directionality, and raster scans which are extremely useful for polarization measurements.

While the raster scan can be used for large scale intensity mapping where the scan speed is high, the directionality of the raster scan causes streaking in the final map due to atmospheric 1/f noise. This is why a fourth mapping pattern is used with TolTEC which is called the rastajous pattern (see Fig. 3.4). As the name suggests it is parametrized by the sum of a raster scan and a Lissajous or double Lissajous. The advantage of this is that we get the uniform coverage of a raster scan but remove the directionality through the superimposed Lissajous pattern. This pattern therefore is extremely favourable for intermediate size maps that are larger than the field of view but still less than square-degree sized fields. Because the underlying raster scan for a rastajous has a scan speed of a few arcsec/s it generally takes a long time to complete one scan which is why this scan is not favorable for large fields. Otherwise, this would require mosaicing which again renders the coverage non-uniform.

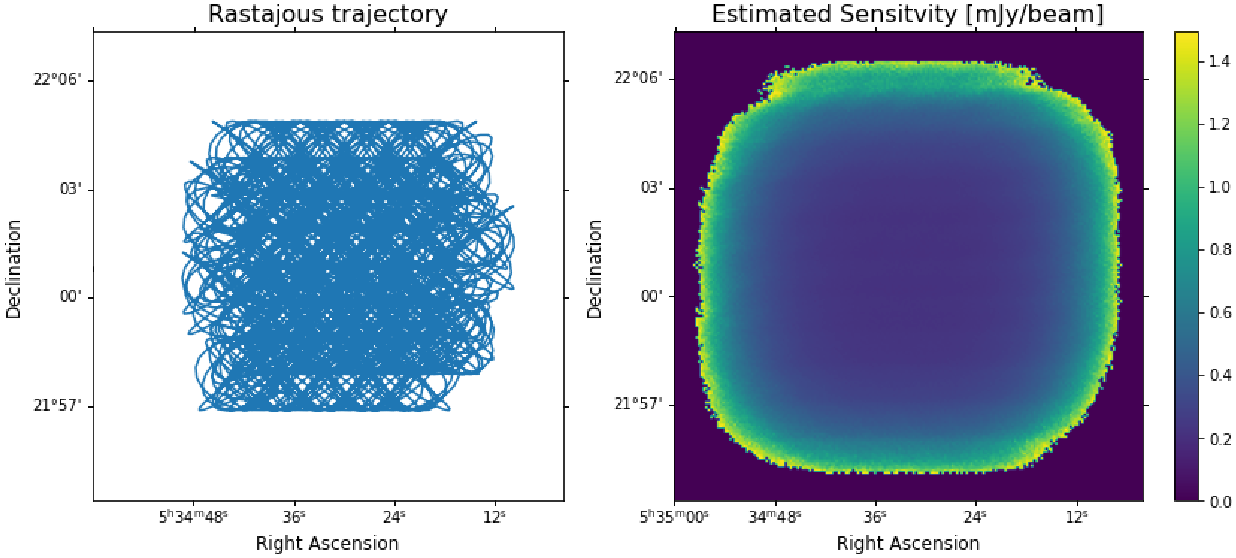

Figure 3.4: *Left*: Trajectory of a rastajous scan with six 5 arcsec/s raster scans spaced apart by $1'$ and a $2' \times 2'$ superimposed lissajous pattern. *Right*: Expected sensitivity as estimated by the TolTEC ObsPlanner. The underlying raster scan makes the coverage in the region of interest extremely uniform.

For the Fields in Filaments Survey we will be making maps ranging in side length from about 10' all the way up to 30' which are highly rectangular. Given these size scales we will be using rastajous scans for total intensity maps, and due to the superimposed Lissajous pattern greatly reducing streaking effects from 1/f noise. Simulations in Figs. 3.5,3.8 and 3.11 demonstrate that the rastajous scan indeed has the desired effect in terms of eliminating streaking features. Since the rastajous scan, just as for the Lissajous scan has a non-uniform scan speed we will be using simple raster scans both along and orthogonal to the filament for polarization measurements, where 1/f noise will be negligible. Therefore this requires us to make total intensity observations and polarization observations in separate observing runs. The raster scan speed for both the rastajous and the raster scan is then adjusted such that each observation is below the 1h time-limit per observing run, imposed by focus drifts of the telescope. For polarization measurements we have another constraint imposed by the beam modulation giving an upper bound of 13 arcsec/s on the scan speed. Therefore, the strategy will be to make multiple 0.5-1 hour maps which are then coadded to effectively increase the integration time.

	Pattern	Raster speed	Raster spacing	Max. Lissajous speed
Stokes I	Rastajous	5-8 arcsec/s	1 arcmin	50 arcsec/s
Stokes Q/U	Raster	<13 (typ. 5-8) arcsec/s	1 arcmin	n/a

Table 3.1: Table of mapping guidelines for the Fields in Filaments survey, the raster speed is chosen based on the map size and 1h time limit per pass. For polarization this should not exceed the upper bound of 13 arcsec/s. The $1'$ spacing was deemed as sufficient based on simulations and given the $4'$ field-of-view, but can be reduced without compromising map quality, this should not exceed the TolTEC field of view. The mapping patterns are then supposed to be repeated until the desired integration time is reached.

On top of this the Lissajous pattern in the rastajous should be kept as fast as possible, which currently is 50 arcsec/s, imposed by the LMT (however for simulations a faster Lissajous speed of several arcmin/s was assumed) in order to keep 1/f noise to a minimum.

The speed of this Lissajous does not affect the coverage so long as the raster speed stays the same and is much slower than the Lissajous speed. Similarly, the Lissajous extent (typically $1'$ or $2'$) for this pattern should be much less than the map size to keep the coverage uniform. A list of recommended mapping parameters for the Fields in Filaments survey based on the requirements outlined in the previous paragraphs as well as simulations can be seen in Tbl. 3.1. These parameters may have to be adjusted depending on the region size, and detector yields after commissioning.

3.1.2 Effects of atmospheric removal on the Stokes I signal

One important astronomical goal for TolTEC will be to recover scales down to the $5'$ (850 μm) *Planck* resolution. As mentioned in Sec. 2.4 the data reduction pipeline `citlali` uses PCA to remove atmospheric 1/f noise from total intensity data. This method removes the largest eigenmodes in the detector covariance matrix under the assumption that these are dominated by sky noise. At the same time, the largest eigenmodes also contain small amounts of large-scale astrophysical signal and we therefore expect a loss in large scale structure in the final map when applying PCA. This spatial filtering will change depending on how many eigenmodes we choose to remove.

In order to investigate this effect, I made synthetic TolTEC observations with `ORION` simulated maps (which are high-resolution adaptive-mesh-refinement, gray-flux limited diffusion radiative transfer hydrodynamic simulations) from Betti et al. 2021 and Qian et al. 2015 (and references therein) that were kindly provided by Rob Gutermuth as priors. The reason `ORION` maps were chosen as a “truth” was because they exhibit typical dust emission in star-forming regions at the TolTEC bands as well as spatial scales beyond the TolTEC beam at 1.1 mm. Before simulating, we convolved the raw `ORION` images with their appropriate TolTEC beamsizes to account for diffraction limited angular resolution (see left panel in Fig. 3.5). Lastly, we synthetically observed them with a $15' \times 15'$ rastajous pattern which is the preferred total intensity mapping pattern for the Fields in Filaments Survey (see right panel in Fig. 3.5), together with a synthetic time-varying atmospheric signal generated by the TOAST3 module[2] which simulates 1/f noise due to the atmosphere.

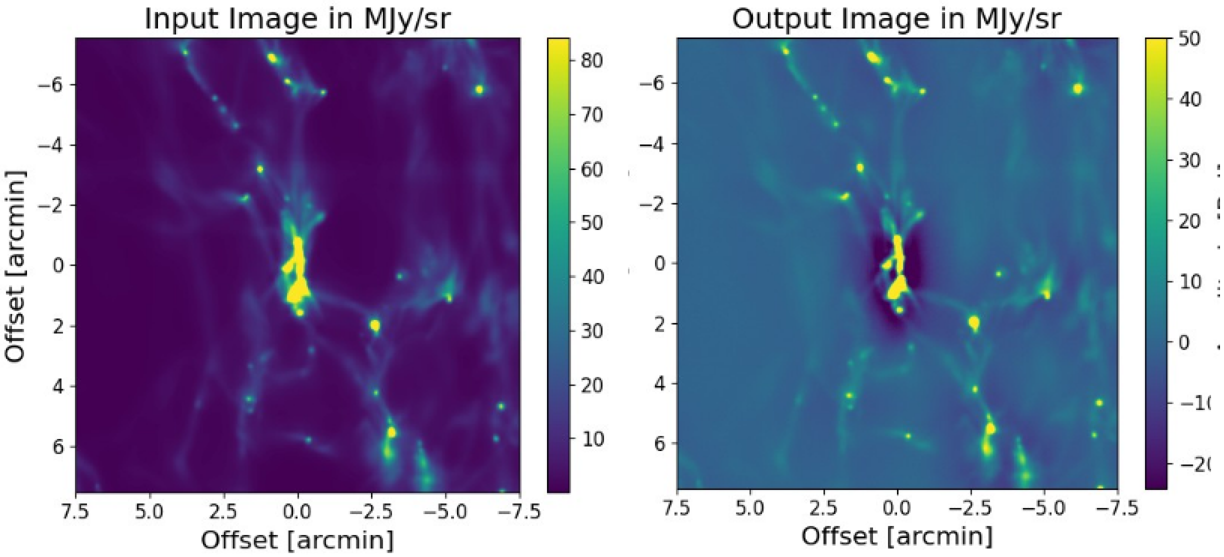

Figure 3.5: *Left*: The input total intensity `ORION` (Betti et al. 2021,Qian et al. 2015) simulated image at 1.1 mm convolved with a $5''$ beam. *Right*: Synthetically observed output image removing 3 eigenmodes at the PCA cleaning stage. The dark, negative regions are due to spatial filtering of large scales. This map corresponds to about 1.5 hours of data and was created with a $15' \times 15'$ rastajous scan.

To quantify the loss in spatial scales which is evident in the rightmost panel of Fig. 3.5 I wrote a Fourier analysis software package based on the Numpy FFT library to compute the average radial Fourier amplitude by azimuthally averaging the 2D Fourier amplitude for the input and output images as depicted in the left panel of Fig. 3.6.

---

[2] `https://github.com/hpc4cmb/toast`

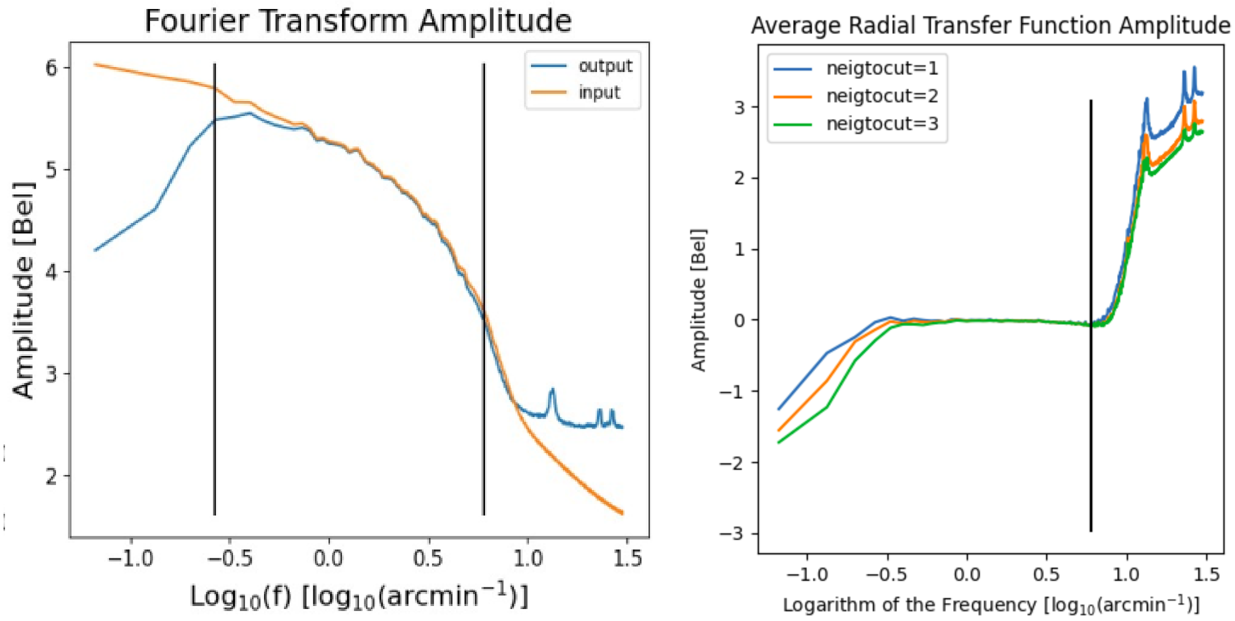

Figure 3.6: *Left*: Average radial Fourier amplitude for the input and output images in Fig. 3.5 at 1.1 mm. Note the drop in power for large spatial scales. The almost constant power-level beyond the right most black line representing a TolTEC beam are due to pixel-to-pixel noise. The leftmost black line indicates the 3dB cutoff scale of 1.9′. *Right* Average radial transfer function amplitude for the `ORION` TolTEC maps removing 1, 2 and 3 eigenmodes (neigtocut parameter in the legend) at the PCA cleaning stage. The sharp increase at small spatial scales is due to noise. Large spatial scales are attenuated more and more and noise power levels drop with an increase in removed eigenmodes.

Using the input and output Fourier transform we can compute the transfer function

$$H(f) = \frac{F_{out}(f)}{F_{in}(f)} \tag{3.4}$$

where F_{out} and F_{in} are the output and input Fourier transforms. The transfer function therefore quantifies the expected response of the telescope and data reduction pipeline. A plot of the average radial transfer function amplitude can be seen in the right panel of Fig. 3.6. Therefore, at low spatial scales we lose structure and at spatial scales beyond the beamsize we accumulate white noise added by the simulator. The spikes at high spatial frequencies are a consequence of streaking caused by 1/f noise. As shown in Fig. 3.6, the number of spatial scales we lose, depends on the number of eigenmodes that are removed during PCA. The transfer function allows us to estimate this by determining the angular size where the power drops 50 %, which for this simulation is given by $2.7'$, $2.5'$ and $1.9'$ removing 1, 2 and 3 eigenmodes respectively. A factor of 2 was divided out in the conversion to length to account for the fact that in order to represent structures of size L we need a sine wave of wavelength $2L$. Similarly, in order to uniquely sample a sine wave of frequency $1/2L$ we need to sample at at a rate $1/L$. While we loose spatial scales in PCA-cleaning we also see a reduction in noise which is demonstrated by the drop in noise power levels beyond the beamsize with an increase in removed eigenmodes. This can be seen in the transfer function plot in Fig. 3.6. PCA-cleaning therefore has to be weighed carefully when reducing data. On one hand, there is a reduction in atmospheric noise and on the other there is a loss in spatial scales.

As demonstrated by this analysis, the current combination of PCA-cleaning and naive map-making is not sufficient to recover spatial scales down to the resolution of *Planck* for Stokes I (total intensity), however a future investigation into maximum likelihood map-makers may improve these bounds.

For polarization measurements there is no need for PCA due to half-wave-plate modulation and due to the fact that the emission of the atmosphere is mostly thermal and hence unpolarized. As demonstrated by Fig. 3.7 we will therefore be able to recover more large scale structure in polarization measurements than in total intensity measurements, which is something that has to be taken into account when analyzing science data. This could potentially be done by combining TolTEC Stokes I data and *Planck* data, applying techniques (such as feathering) typically used for combining interferometric with single-dish observa-

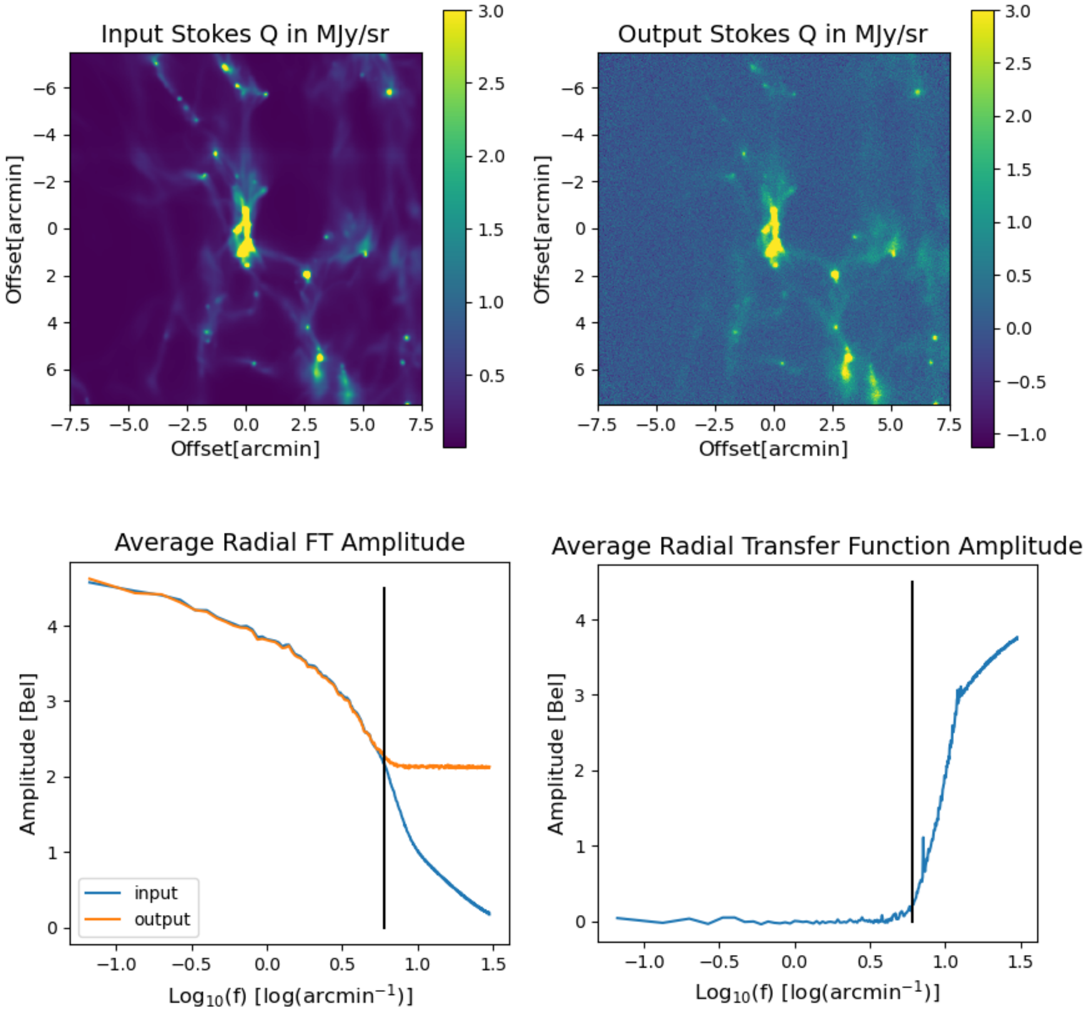

Figure 3.7: *Top Left*: The input Stokes Q image to the simulator. The image is based on `ORION` simulations from Betti et al. 2021 and Qian et al. 2015 assuming a constant polarization fraction of 5 % and a constant polarization angle of 22.5° (i.e. Stokes Q and U positive and equal). *Top Right*: Synthetically observed Stokes Q output consisting of the co-addition of 15 orthogonal $15' \times 15'$ raster scans using a scan speed of 5 arcsec/s. No PCA cleaning was applied to the output in this image, note the absence of holes in the map. *Bottom Left*: Average radial FT amplitude for both the input (blue) and output (orange) Stokes Q signal. *Bottom Right*: Average transfer function amplitude, note how the transfer function is flat indicating that we are recovering more large scale structure than for Stokes I.

tions in the radio, such as the methods outlined in Hoffman et al. 2018 and Dirienzo et al. 2015. Nonetheless the results in Fig. 3.7 should be taken with caution because the simulator assumes perfectly correlated detector noise which may not be the case for the real instrument. If the noise is not perfectly correlated then the 1/f noise levels of the polarized signal would increase degrading map quality. Further investigation on real data is therefore required.

3.1.3 Simulations of Fields in Filaments targets

As discussed in Sec. 3.1.1 we will be using two very different mapping strategies for polarization and total intensity measurements even though the information for both of these observations can be collected in one observing run. We therefore have to determine what fraction of the total time allocated to the Fields in Filaments targets in Tbl. 2.2 will be used towards total intensity measurements which are necessary to determine the polarization fraction. In order to determine this fraction there are multiple considerations to be taken into account. I will be illustrating this for two Fields in Filaments targets Rho Ophiuchus C, E and F, which represents an extended filament, as well as OMC 2/3, which represents a dense filament.

As demonstrated in Sec. 3.1.2, the final noise-levels in total intensity maps depend on how many eigenmodes are removed during PCA cleaning, at the same time, there is a loss in spatial scales which reduces the visible flux. While the former increases the signal-to-noise ratio the latter degrades it. Furthermore, while for white noise we expect the RMS to decrease as $t^{-1/2}$, where t is the integration time, this may not be the case for residual 1/f noise where the RMS increases as t^α where α is the spectral index of the noise power spectrum in Eq. 1.2, causing the noise to integrate down slower than white noise. We therefore cannot make this assumption for total intensity maps. Furthermore, we have to take into account that the polarized signal only is a few percent of the un-polarized signal and that due to the design of TolTEC we only have half as many samples for polarization observations, because we require a pair of detectors for one value of each Stokes Q or U. We therefore expect to integrate longer for polarization measurements than for total intensity measurements.

Apart from keeping track of the sensitivity as a function of integration time it is important to keep the science requirements in mind. For the Fields in Filaments survey there are two quantities of interest, the polarization fraction given in Eq. 2.4 and the polarization angle in Eq. 2.3. Therefore, the first requirement is to get at least a 3σ detection on the polarization fraction and an error of less than 10° on the polarization angle. Because we are dealing with extended emission it is impossible to satisfy these requirements on the entire map due to the fact that not all of the map contains signal. We therefore are interested in the percentage of the map satisfying the science requirements. Hence, this analysis becomes a matter of error propagation.

The error in the polarization fraction is given by

$$\delta p = p\sqrt{\left(\frac{\delta I(t_I)}{I}\right)^2 + \left(\frac{\delta P(t_{tot} - t_I)}{P}\right)^2} \tag{3.5}$$

where I and P are the polarized and total intensities, t_I is the integration time on Stokes I and t_{tot} is the total time allocated for the target. Therefore if the integration time on total intensity is increased, the first term in the square-root decreases and the second term increases and vice versa, which allows for optimization. The error in the polarized intensity is given by

$$\delta P = \frac{\sqrt{(Q\delta Q)^2 + (U\delta U)^2}}{P} \tag{3.6}$$

where Q and U are the Stokes parameters. In the case of TolTEC it is a fair assumption to assume that $\delta Q = \delta U$ in which case $\delta P = \delta Q = \delta U$, this therefore greatly simplifies the error propagation. Next, for the polarization angle (in radians) the error is given by

$$\delta \chi = \frac{\sqrt{(U\delta Q)^2 + (Q\delta U)^2}}{2P^2}. \tag{3.7}$$

Note here that if we assume $\delta Q = \delta U$ this simply becomes

$$\delta \chi = \frac{\delta P}{2P}. \tag{3.8}$$

It therefore is sufficient to simply consider the polarized and total intensities for this analysis. Next, we have to consider what we use as an estimate to determine the expected total and polarized intensities.

In order to get a ball-park estimate for total intensity we use 250 μm Herschel maps of the FiF targets extrapolated to the TolTEC bands assuming a dust spectral index β of 2 and assuming a modified black body in total intensity proportional to

$$I_\nu \propto B(\nu, T)\nu^\beta \tag{3.9}$$

where ν is the frequency and T is the dust temperature, and $B(\nu, T)$ is the Planck black-

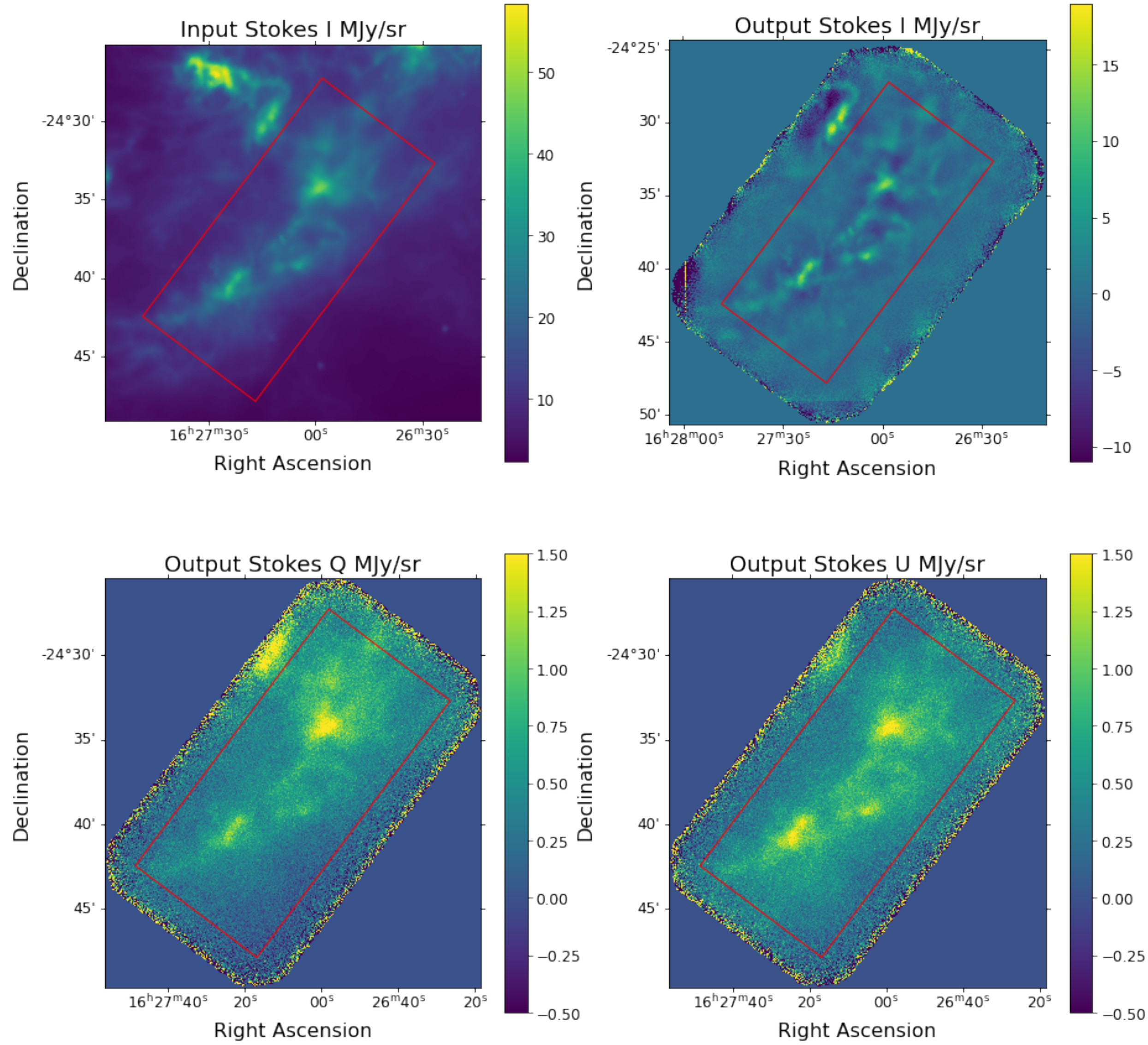

Figure 3.8: TolTEC synthetic observations of 1.1 mm Stokes I, Q and U for Rho Ophiuchus C, E and F which is one of the Fields in Filaments targets. The Stokes I input to the simulator was taken to be a 250 μm Herschel map extrapolated to 1.1mm using a dust spectral index of 2 (Roy et al. 2014,Bij 2022), for Stokes Q and U we assumed a 5% polarization fraction across the input map with a 22.5° angle giving equal Stokes Q and U. The total intensity map was created using two coadded rastajous patterns giving an effective integration time of about 1.3 hours. The Stokes Q and U maps were synthetically observed using 18 orthogonal raster scans giving a total integration time of about 11.7 hours. These integration times are slightly longer but comparable to what would be used for a Fields in Filaments map. The slight gradient running across the polarization maps is due to a software bug in `tolteca` that occured when correcting for the parallactic angle which is described in more detail in Sec. 3.2 .

body function. Details about the procedure can be found in Roy et al. 2014 and Bij 2022. Because the Herschel maps have a resolution coarser than the TolTEC beam the flux loss due to spacial filtering will be slightly higher than at TolTEC resolution. However, since the Herschel resolution of $18''$ is still smaller than the cutoff scales in Sec. 3.1.2 and therefore still is in the flat part of the transfer function in Fig. 3.6, we expect that the flux loss will still be comparable to real TolTEC data. For the polarized signal we then assumed a constant polarization fraction of 5% with equal contributions from Stokes Q and U giving a constant angle of 22.5°. This was done to keep the signal simple, due to the presence of a bug in `citlali` and the simulator which is discussed in further detail in Sec. 3.2. Note that for the purpose of determining errors we only need the polarized and total intensity and we can therefore make an arbitrary choice for the polarization angle. These maps were then synthetically observed using the TolTEC simulator together with a rastajous pattern for total intensity and a raster scan for polarization measurements. An example of this for Rho Ophiuchus C, E, and F can be seen in Fig. 3.8.

Now that we have an estimate of what the signal looks like we now need to determine a way to estimate the average RMS in the map as a function of time. The challenge here in particular lies in the total intensity maps. We can't simply compare the input with the output due to spatial filtering induced by PCA cleaning, furthermore, due to the presence of residual 1/f noise we can't assume the $t^{-1/2}$ dependence of the RMS on integration time. We therefore use the scheme in Fig. 3.9 where we compute the RMS by computing the difference between a map containing an average of multiple observation with that of a single observation of known integration time. The number of maps in the average was chosen such that the noise in this model (left hand column in Fig. 3.9) was much less than the noise in the map for which we want to compute the RMS (right hand column in Fig. 3.9). Furthermore we do a 5σ cut on outliers to mitigate effects of misalignments that arise (especially for the first data point in Fig. 3.9) from rotating the pixel axes of each domain for analysis.

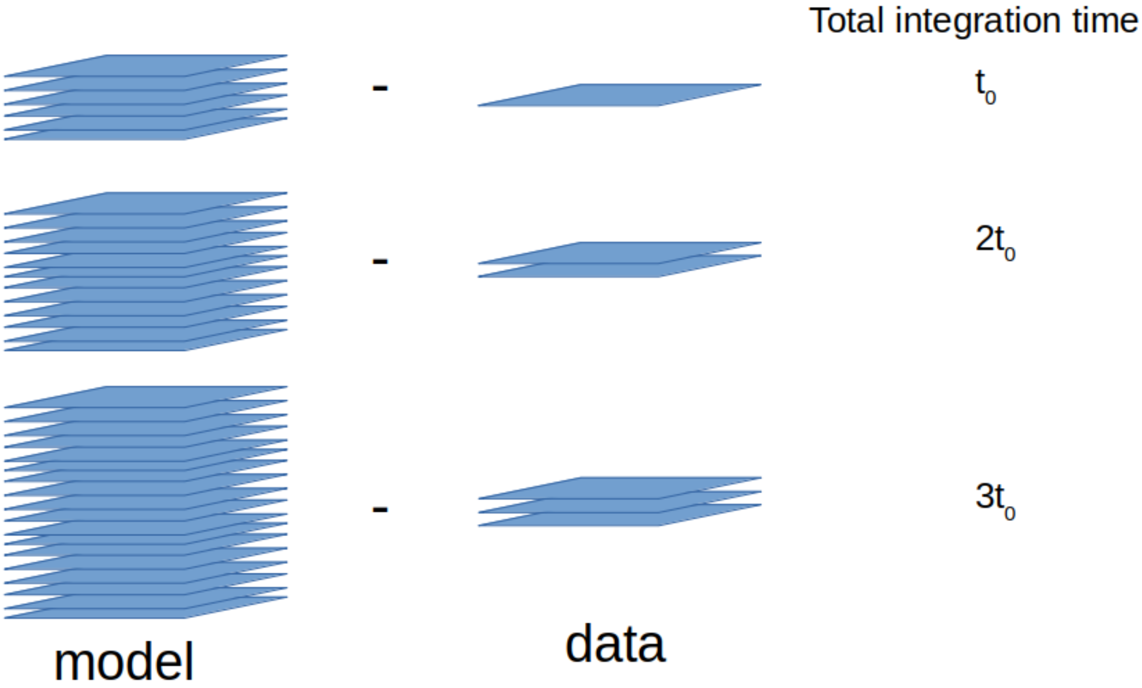

Figure 3.9: Procedure for computing the RMS. The stacked maps in the cartoon represent coadded maps (that is, a weighted average of multiple observations), which serve as the model. The number of coadded maps in the model is adjusted to ensure that the noise in the model is significantly lower than the data to avoid inducing any bias in the RMS computation. Each single map (one slice in the cartoon) has integration time t_0. This procedure was repeated for each subset of data in the model stack to get a representative guess for the RMS. The ratio of model to data maps was determined based on computation time for the simulations.

For total intensity data we then use the RMS for all three integration times in Fig. 3.9 and fit a power law of the form At^b to it to determine the time dependence. This was repeated for maps reduced with different PCA settings to investigate the effect on the signal-to-noise. Because the CRHWP modulates the polarized signal at a frequency much greater than the 1/f-knee the noise is effectively white and we may assume a $t^{-1/2}$ dependence for the RMS for Stokes Q and U and hence only need one data point to determine the proportionality constant. In this case the second data point in Fig. 3.9, to remove the effect of the polarization bug in Sec. 3.2.

With the time dependence established, the evolution of the signal-to-noise on the polarization fraction and the error in the angle as a function of Stokes I integration time can be computed using Eqs. 3.5 and 3.8 and keeping the total amount of time (on Stokes I and Stokes Q/U) for that target fixed. This computation was done for every pixel in the region of interest (red box in Fig. 3.8) for each point in Stokes I integration time to compute the fraction of pixels satisfying the science requirements. A plot of how this fraction evolves with time for Rho-Ophiuchus C,E and F can be seen in Fig. 3.10.

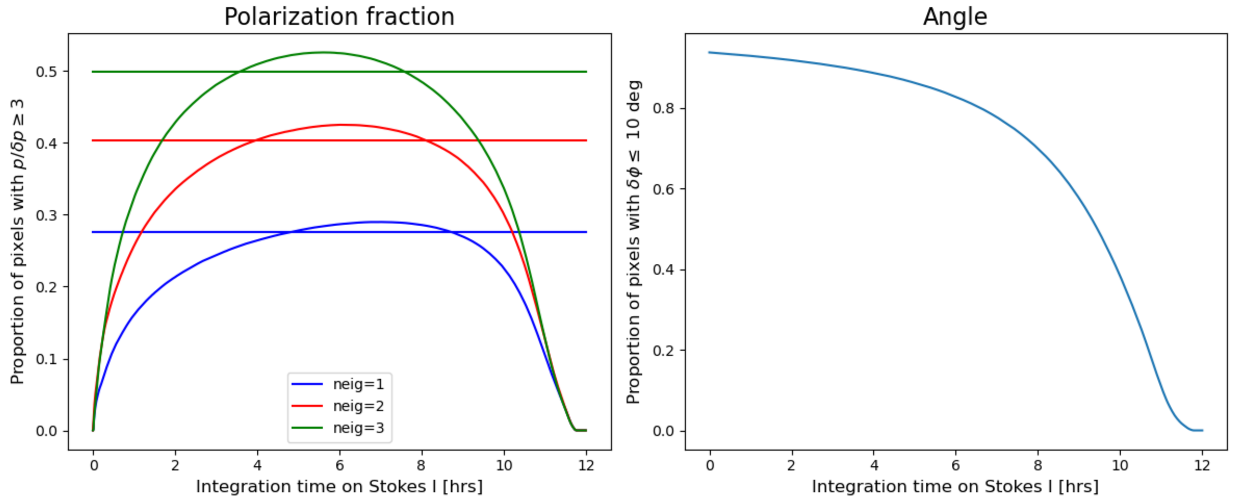

Figure 3.10: Fraction of map-pixels satisfying the science requirements for the Fields in Filaments survey for both the polarization fraction and angle in the simulations for Rho Ophiuchus C, E and F as a funtion of integration time on Stokes I (i.e. the time on Stokes Q/U will be given by 12 h $-\ t$ in this case). The total allocated time for this target is 12 hours. For the polarization fraction this computation was done removing 1(blue), 2(red) and 3 (green) eigenmodes. For the angle there is only one curve since there is no PCA applied when reducing polarization data. The horizontal lines indicate 95% of the maximum which was used as a guideline for the fraction of time to spend on Stokes I integration.

There are a couple of comments to be made about the plots in Fig. 3.10. The first point to note here is that there is no need to maximize the number of “good” pixels in the polarization fraction as not the entire map is of interest to us, moreover for Rho Ophiucus C, E and F the filament of interest only makes up about 20-30% of the map. However, in order to stay consistent with determining thresholds across targets we picked the ”optimal” Stokes I integration time to be the time when the polarization fraction curve is within 95% of its peak, which amounts to about 3.5 hours assuming that we remove 3 eigenmodes during PCA cleaning. The next most obvious aspect is that we can (at least for this target) improve the measurement in the polarization fraction dramatically by increasing the number of removed eigenmodes during PCA cleaning. Lastly, the estimate from the 95% threshold should only be considered a guideline, mainly because the assumptions about the signal are rather crude due to our assumption of the dust spectral index (which still is highly debated in the literature) used for the simulated total intensity maps. Furthermore, the assumption of a constant polarization fraction is equally crude as the polarization fraction usually tends to be lower in brighter parts of the map.

Rho Ophiuchus C,E and F is a very extended target and the signal-to-noise therefore improves greatly when applying PCA to raw data. This is because PCA removes low frequency variations from time streams and therefore large scale variations in the final map we therefore expect to see more improvement in signal-to-noise on large scales than on small scales. It therefore is important to also study the behaviour of targets that contain mostly small scale structure. The best example of a target with an abundance of small-scale structure is OMC 2/3 and of all the Fields in Filaments targets this one is the brightest. Synthetic TolTEC observations of this target are shown in Fig. 3.11.

If we now repeat the analysis in this section for a target like OMC 2/3 we get a result that

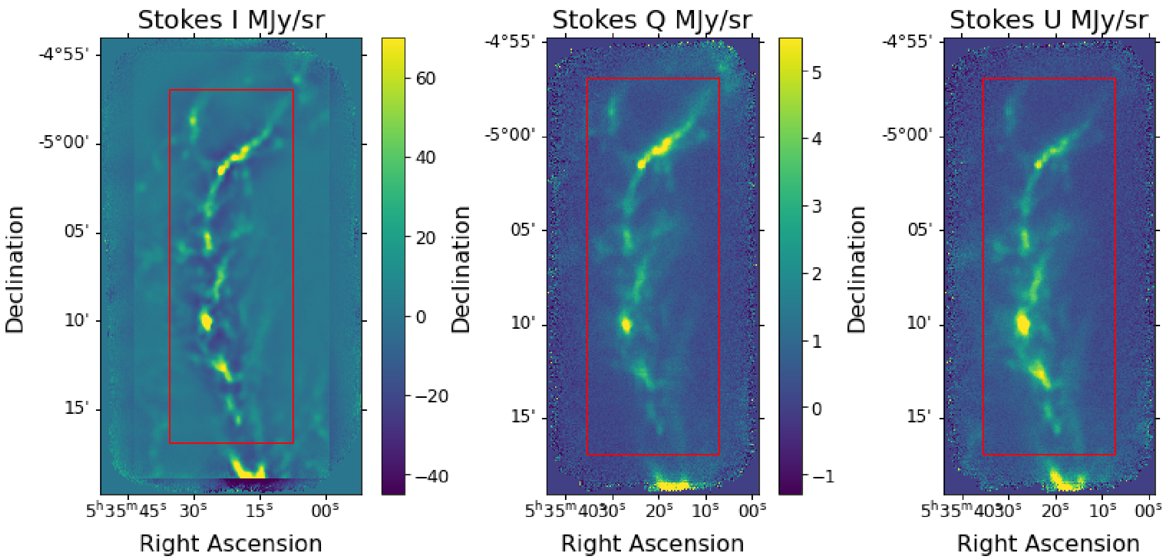

Figure 3.11: Synthetic 1.1 mm TolTEC observations of OMC 2 and 3 also known as the integral filament. The priors for these simulations were also based on 250 μm Herschel data. The Stokes I map corresponds to about 1.5 hours of data and the polarization maps correspond to about 9 hours of data. Just as for all Fields in Filaments targets the total intensity map uses a rastajous scan and the polarization maps use a raster scan. The boundaries of the region of interest are indicated by the red rectangle.

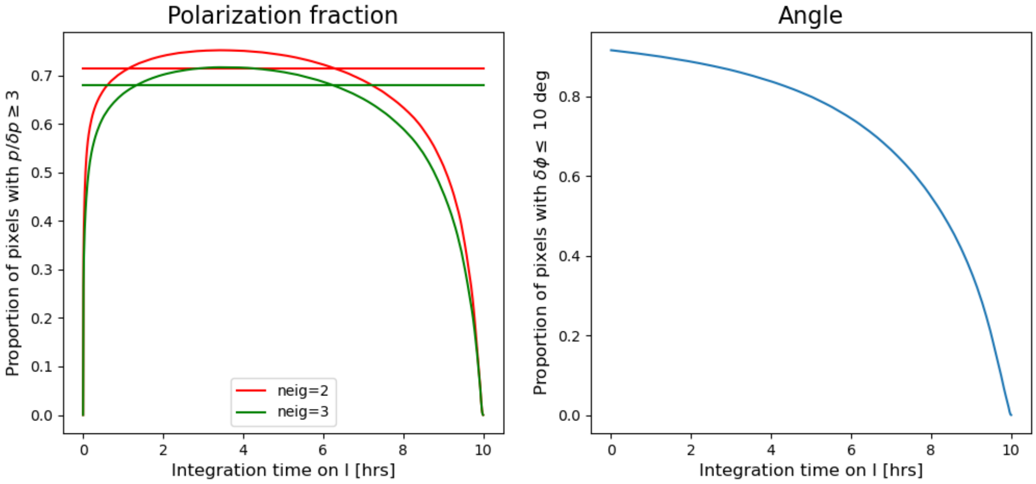

Figure 3.12: Proportion of “good” map pixels as a function of Stokes I integration time. Note how the quality of the polarization fraction map degrades with an increase in removed eigenmodes during PCA cleaning. The horizontal line again indicates 95% of the peak value.

may at first seem surprising. Fig. 3.12 implies that the quality of the polarization fraction measurement degrades with an increased number of removed eigenmodes. While the actual map RMS does decrease there at the same time also is a loss in signal. The signal-to noise ratio of the polarization fraction depends on the signal-to-noise in the total and polarized intensities and the graph in Fig. 3.12 therefore implies that we lose more signal in Stokes I than we can make up for by improving the RMS. Furthermore, the difference between removing 2 or 3 eigenmodes is marginal for this kind of target. This can also be seen in the 95% threshold which is reached after 1.1 hours removing 2 eigenmodes and 1.4 hours removing 3 eigenmodes.

To conclude, the PCA implementation in `citlali` removes large scale, high amplitude map variations that contain both noise and signal. PCA therefore is a double-edged sword which has to be taken into account when considering the signal-to-noise ratio which ultimately affects the error on the polarization fraction. In this limit of very faint and extended structures the largest eigenmodes are primarily dominated by atmosphere and PCA therefore affects the noise more than the signal. As expected we have to allocate more time for Stokes I for the faint case. For compact and bright structures the largest modes will contain a non-negligible amount of authentic sky signal which as a result gets cut by PCA. Furthermore, PCA affects noise mostly on large scales than on small scales and it therefore marginally improves the signal-to-noise on small filamentary scales. However in the bright and compact limit we can, as expected, allocate less time than in the faint case. PCA therefore is highly adaptive where the behavior depends on the type of signal that is fed into the filter. While the results in this section should be taken with caution mainly due to the assumptions on the polarized signal, as well as the perpetual over-estimation of the RMS in this section (in particular for the first data point which artificially steepens the RMS trend), it is fair to assume that about 10-25% of the total allocated time has to be spent on Stokes

I observations (See Tbl. 3.2) , depending on the nature of the target. We hope to mitigate this fraction through the use of maximum likelihood map-makers that will be implemented into the reduction process. Lastly, depending on what the results for commissioning will bring this will have to be adjusted. This analysis could not be done for all targets because not all Fields in Filaments targets have usable Herschel maps, furthermore I focused on the brightest targets and spring/winter targets in this work as these are likely the first legacy targets to be observed, and the procedure outlined in this section is computationally quite intensive making it rather unwieldy when applied to multiple targets. Lastly, the newest version of `citlali` could not reduce simulated data putting a stop to this effort.

Target	Pattern Size	Pattern rotation	Stokes I time	Stokes Q/U time
OMC 2/3	$20' \times 7'$	0 deg	1.4 h	8.9 h
Serpens South	$29' \times 12'$	25 deg	4.5 h	15.5 h
Rho Oph C, E and F	$19' \times 9'$	37 deg	3.6 h	8.4 h
NGC 1333	$14' \times 12'$	350 deg	1.4h	10.6 h

Table 3.2: Projected integration times on Stokes I and Stokes Q/U (assuming 3-eignemode PCA) for three of the seven Fields and Filaments targets as well as NGC 1333 a potential polarization commissioning target. Furthermore, brighter targets and winter/spring targets have been prioritized for this analysis due to time constraints.

3.2 Testing `citlali` with simulations

As shown in Fig. 3.8 the simulated maps (assuming the CRHWP) showed a gradient running diagonally along the map, which suggested that the software did not correct for the parallactic angle (the angle between equatorial and azimuth/elevation coordinates) properly and as a result did not transform the polarization angle from the instrument frame to the sky frame correctly.

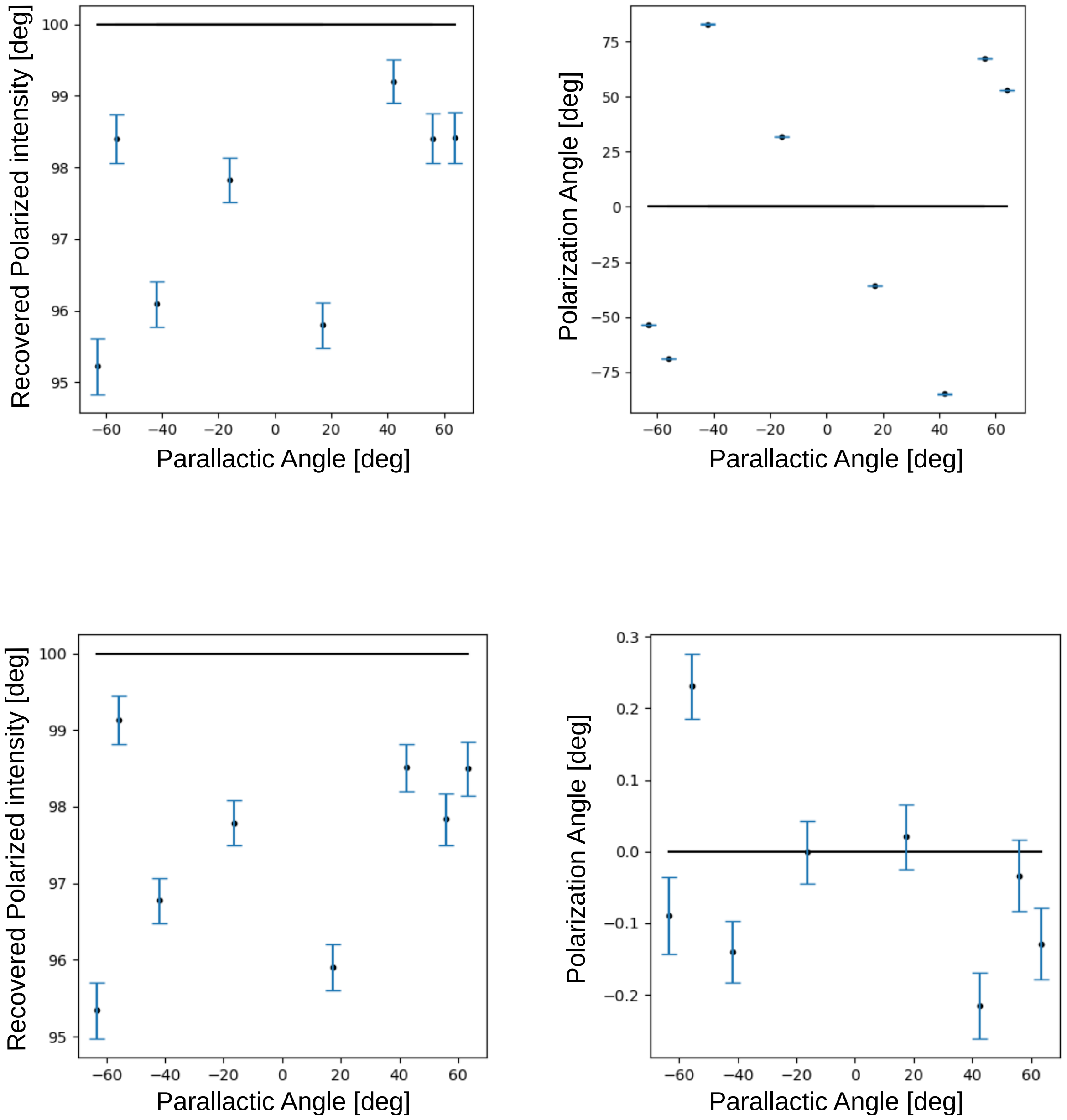

Figure 3.13: *Top:* Simulation results of a single fully polarized point source at different parallactic angles with the CRHWP before the bug was identified. For these simulations a static atmospheric model was used to simplify the simulation and to restrict the noise contributions to detector noise. While the recovered polarized intensity (*Left*) is mostly independent of parallactic angle the polarization angle (*Right*), up to a 180° phase, has a linear dependence on the parallactic angle, the discrepancy from the expected value (black line) is about twice the parallactic angle. *Bottom:* Recovered polarized intensity(*Left*) and polarization angle (*Right*) after matching sign conventions between the simulator and `citlali`. In this case there no longer is a clear dependence on parallactic angle in the polarization angle.

In order to track this bug in the simulation/reduction process the observation of a fully polarized 0° (Stokes Q positive, Stokes U 0) 100 mJy point source was simulated at different parallactic angles (i.e. on ascent and descent, the parallactic angle of a source is zero during transit). The resulting flux in Stokes Q and Stokes U was then determined using aperture photometry. From there, the polarization angle and polarized intensity was determined as a function of parallactic angle.

The results of this analysis can be seen in Fig. 3.13 and clearly demonstrate that this is an effect restricting itself to the polarization angle measurement because the polarized intensity is recovered up to 95 % across all angles. The small discrepancy in the intensity values is due to a known bug in the simulator. Moreover, the discrepancy in the polarization angle (up to mathematical artefacts from keeping the phase wrapped) is linear with a slope of about 2 (i.e the discrepancy is twice the parallactic angle) suggesting a misplaced sign somewhere in the simulation and reduction process.

It turns out that after careful inspection of the code by the developers (Zhiyuan Ma and Michael McCrackan) a discrepancy in sign conventions for the parallactic angle between the simulator and `citlali` was indeed identified. Because this bug restricted itself to the polarization angle and not the polarized intensity the signal-to-noise and error-propagation results in Sec. 3.1.3 remain unaffected as they only depend on the polarized intensity and not Stokes Q and U separately. After the above changes were made the same test was performed again (see Fig. 3.13, bottom row). This modification successfully removed the parallactic angle dependence. Nonetheless, this only makes the simulator and `citlali` self-consistent (assuming a CRHWP) and we therefore need real TolTEC data to check that the overall sign is correct.

Chapter 4

TolTEC Commissioning

In this section I will be presenting some of my analysis on TolTEC commissioning data, including time-ordered data analysis as well as observations of both point sources and extended targets.

4.1 Time-ordered Data

The commissioning phase for TolTEC began in the December of 2022, and in order to study the data on the lowest level it is instructive to analyse time ordered data at the raw time chunk (RTC) phase (after de-spiking, low-passing, and downsampling) and the processed time chunk (PTC) phase after PCA cleaning. Moreover during commissioning the option of array-level PCA cleaning was also implemented in `citlali` and it therefore is important to compare this PCA cleaning approach with network-level PCA cleaning. In this section I will be discussing data from a beammap observation of the quasar 1159+292. This observation was chosen because it, apart from the source, mostly contains blank sky making it an excellent choice for studying noise of TolTEC detector data.

4.1.1 Raw Time Chunk Data

Because the beammap observation for quasar 1159+292 is mostly blank except for the time when a single detector crosses the source and the timestreams themselves are mostly noise, it is more instructive to look at the power spectral density (PSD). An example of this for one of the networks on the 1.1 mm array can be seen in Fig. 4.1.

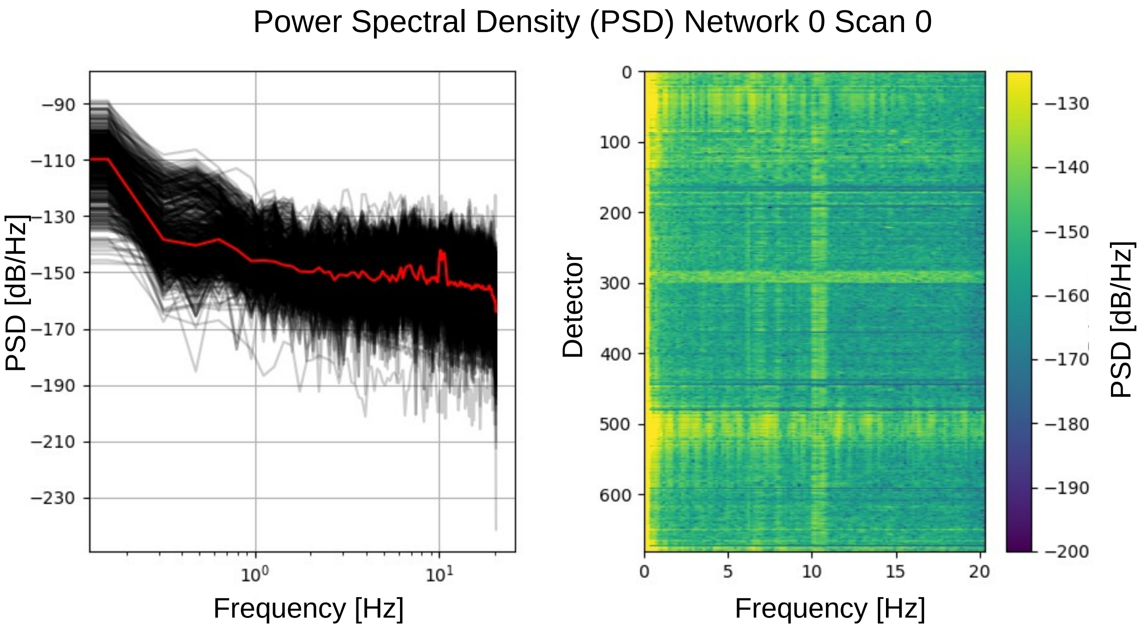

Figure 4.1: Power spectra for the first scan of the beammap of quasar 1159+292 for Network 0 on the 1.1 mm array. The data has been low-passed at 20 Hz, which is why we see a drop in levels beyond that frequency in the PSD. The red curve in the plot on the left shows the median PSD across the entire Network (each black line corresponds to a single detector). The plot on the right shows the PSD as a function of detector number on Network 0 in a waterfall format. All the data has been down-sampled by a factor of 3 from an original sampling rate of 122 Hz to facilitate PCA cleaning later on.

The data shown in Fig. 4.1 exhibit the clear 1/f profile that is expected for raw time chunk data at low frequencies. By noting that the 1/f profile in Eq. 1.2 doubles relative to the white noise level at the knee frequency (the frequency where the spectrum starts to be dominated by the 1/f component) we can estimate the median knee frequency of the scan shown in Fig. 4.1 to be about 1 Hz. One very prominent feature at 11 Hz keeps reappearing throughout the entire data set and across all TolTEC arrays, suggesting that the source of this is external to the instrument. Because this observation is mostly mapping blank field this likely is a vibrational mode in the warm optics or electronic noise from other experiments in the LMT receiver cabin. The exact source for this signal has yet to be determined. As shown in the rightmost panel of Fig. 4.1 there is variation in the noise levels and 1/f profiles across detectors, which demonstrates that there not only is a contribution of the atmosphere to 1/f noise but also the detectors themselves contribute due to thermal variations. Most of the noisier detectors were flagged later on in the beammap reduction, this will be described in more detail in Sec. 4.1.3.

4.1.2 Processed Time Chunk Data

In order to mitigate the 1/f profile in Fig. 4.1 we need to apply PCA to the time-stream. For the current implementation of `citlali` there are two ways of doing this, the first one is to group detectors by network the other is to group them by array (see Fig. 2.5) when applying PCA. A comparison of these two approaches can be seen in Fig. 4.2

The graphs in Fig. 4.2 show that PCA cleaning in any form mitigates 1/f noise as expected, indicated by the fact that the spectra became flat after cleaning. The more interesting result for these plots is that we achieve a similar effect in both the network-level and array-level approach even though we only remove 10 eigenmodes for the network-level case

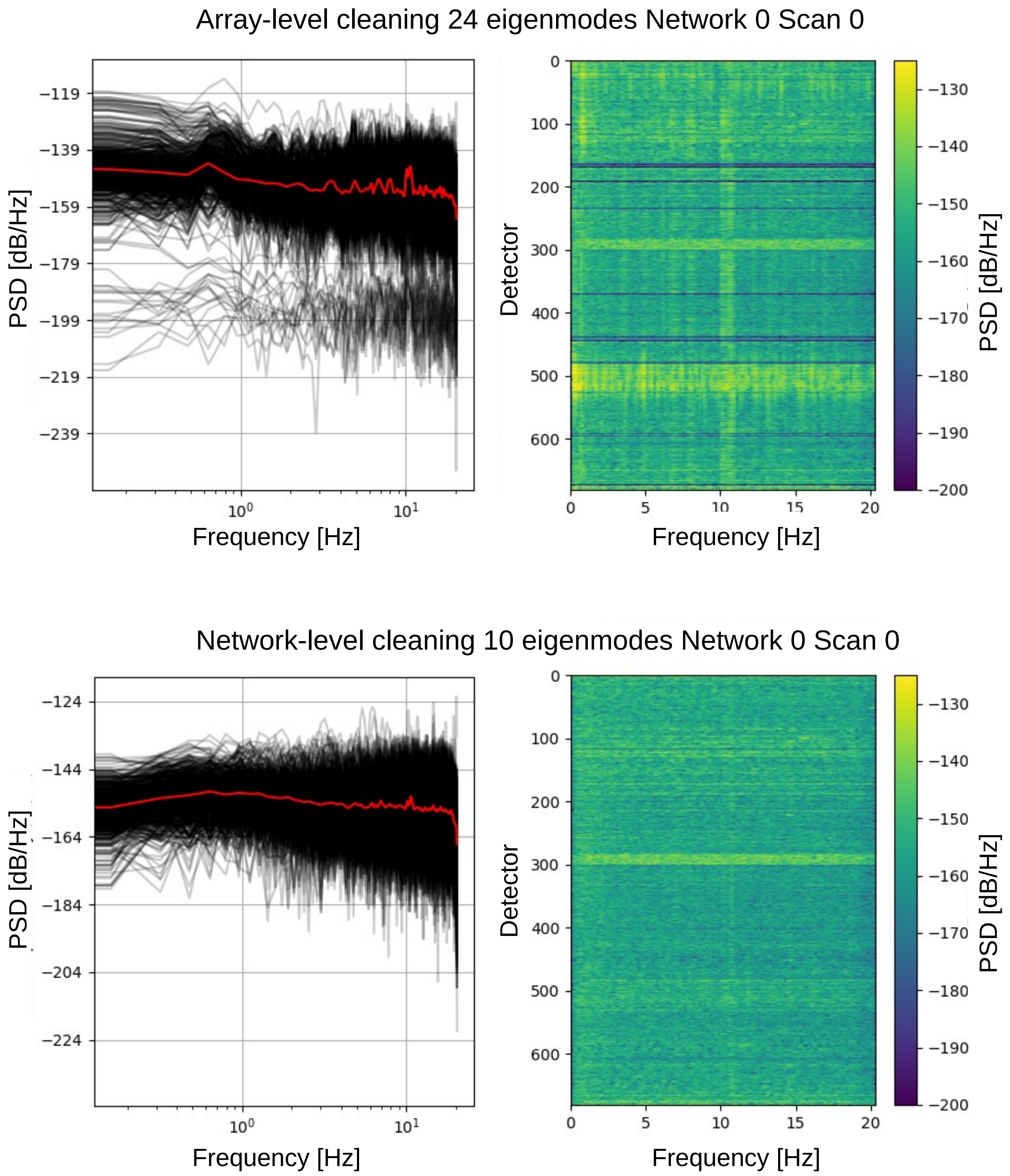
Array-level cleaning 24 eigenmodes Network 0 Scan 0

Network-level cleaning 10 eigenmodes Network 0 Scan 0

Figure 4.2: PSD of the same scan as in Fig. 4.1 for Network 0 on the 1.1 mm array. *Top*: Array-level grouping of detectors removing 24 eigenmodes. *Bottom*: Network-level grouping of detectors removing 10 eigenmodes. The red line indicates the median PSD for the entire network. The power spectra are white for the most part after PCA-cleaning.

instead of 24 eigenmodes for the array-level case, which implies that network-level grouping is more efficient. Network-level grouping also seems to help with removing the 11 Hz signal in the time stream as well as a feature at 0.5 Hz that is very prominent in the array-level cleaned data. To further study the effect of PCA on time-ordered data we can compute the transfer function magnitude by calculating the square root of the ratio of the raw (RTC) vs. the cleaned (PTC) power spectrum as shown in Fig. 4.3.

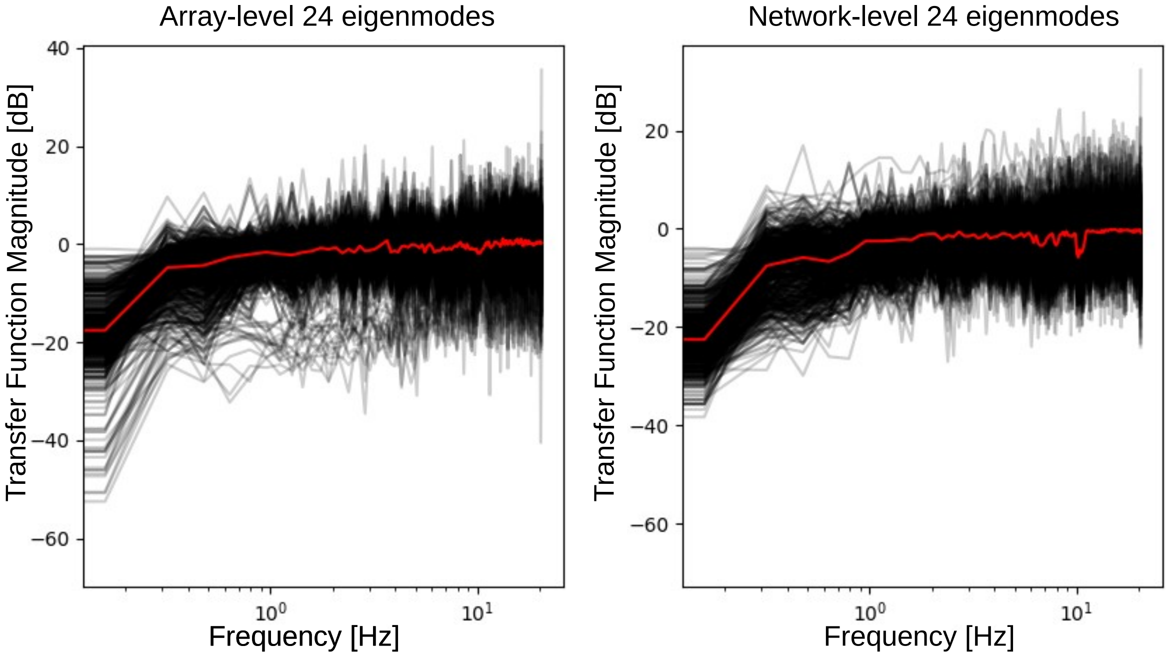

Figure 4.3: Transfer functions computed from the data in Fig. 4.1 and 4.2 for both array-level and network-level cleaning. Just as in the map-domain, PCA also acts as a high-pass filter in the time-domain. The red curve indicates the median transfer function over the entire network.

The transfer function shows that PCA cleaning effectively acts as a high-pass filter on time-ordered data in agreement with the loss in spatial scales seen in simulations. Furthermore the high-frequency white noise remains mostly unaffected by PCA preserving the non-1/f component of the noise.

To conclude network-level PCA-cleaning is more effective than array-level PCA-cleaning, in terms of the number of eigenmodes that we need to remove to achieve a certain reduction in 1/f noise. Furthermore, PCA has the expected high-pass response in the time-domain translating into a high-pass response in the map-domain through the scan speed, which we also saw in simulations.

4.1.3 Detector flagging

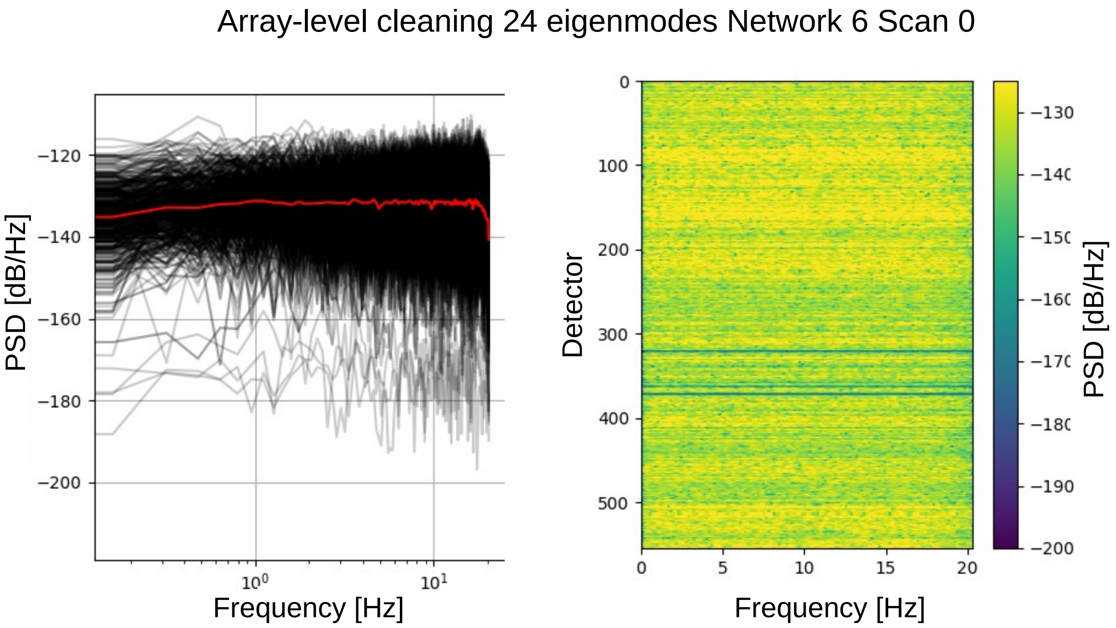

Figure 4.4: Power spectral density for Network 6 on the 1.1 mm array the noise power is about 20 dB higher than for all the other networks on the array.

During the December 2022 commissioning observations two (networks 2 and 6) of the 7 networks on the 1.1 mm array had significantly higher noise levels than expected due to faulty low noise amplifiers in the back-end (see Fig. 4.4). Furthermore one network on the 1.4 mm array was dark, that is we did not get any signal from it. Apart from this there are some detectors in the working arrays that are noisier than others and should therefore be excluded from any sort of science reduction.

The data reduction pipeline `citlali` makes detector cuts based on the time-stream signal-to-noise and the beam shape of each detector. If these parameters are outside of some range specified in the beammap reduction file the detector is flagged as bad in the array property table. An example of this flagging method can be seen in Fig. 4.5.

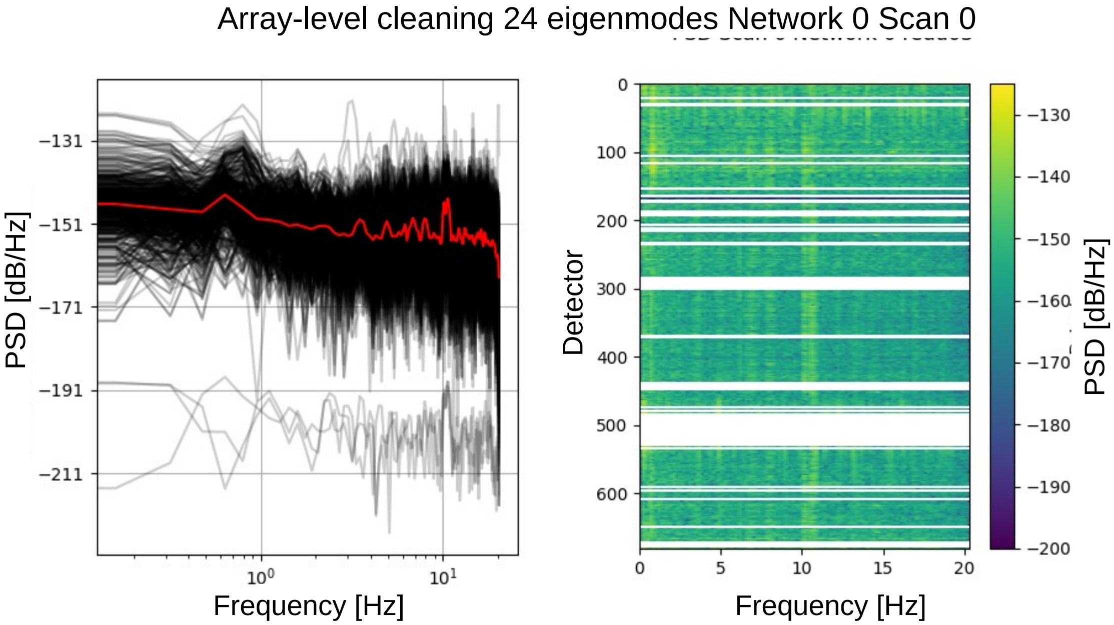

Figure 4.5: Power Spectral Density from Fig. 4.2 not showing detectors as flagged by `citlali`, based on beam shape and time-stream signal-to-noise. In this particular case detectors with a signal-to-noise of less than 3.5 were flagged and detectors with a beam full-width-half-maximum (FWHM) of less than 4″ and more than 20″ were flagged. About 13.5 % of all detectors in the network were flagged as bad.

As a quick comparison between Fig. 4.2 and 4.5 shows, the flagging routine in `citlali` is extremely robust, however it depends on a multitude of parameters that have to be specified by the user. We can greatly reduce the number of input parameters required with a different approach, making cuts based on the power spectral density.

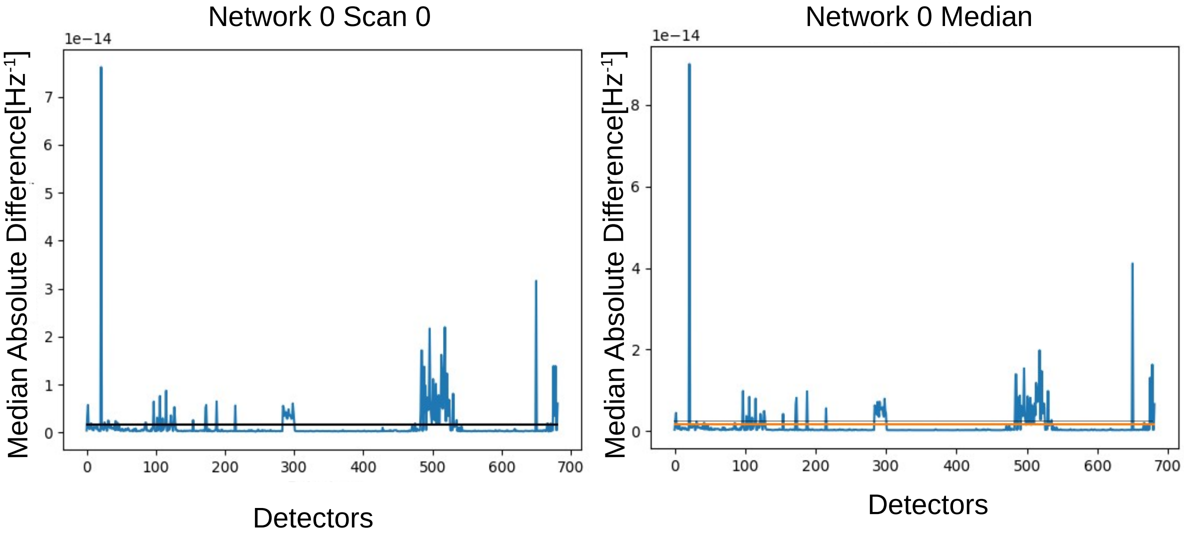

Figure 4.6: Median absolute difference for each detector in Network 0 for both a single scan (*Left*) and the median across all scans (*Right*). The black line indicates the flagging threshold of 5 MAD's across all detectors

The alternate method of flagging bad detectors that I developed is based on the fact that noisy detectors have PSD values that are orders of magnitude higher than the average detector. The first step here is to first subtract out the median PSD profile from each detector and to then consider the absolute value of this difference. We then take the median of this difference across all frequencies for each detector. Like that we get a "spectrum" of the median absolute difference over all detectors of the network (left panel in Fig. 4.6). We repeat this for each scan and then consider the median over all scans (right panel in Fig. 4.6) to ensure that we only flag consistent behavior and not sporadic behavior. Using this median detector spectrum we compute yet another median across the entire spectrum referred to as the median absolute difference (MAD) and we flag everything exceeding 5 MAD's as "bad". Note that instead of specifying three thresholds as in `citlali` we now only specify one based on Gaussian statistics (5 MAD's correspond to about 3σ for a Gaussian distribution). The result of this flagging procedure can be seen in Fig. 4.7.

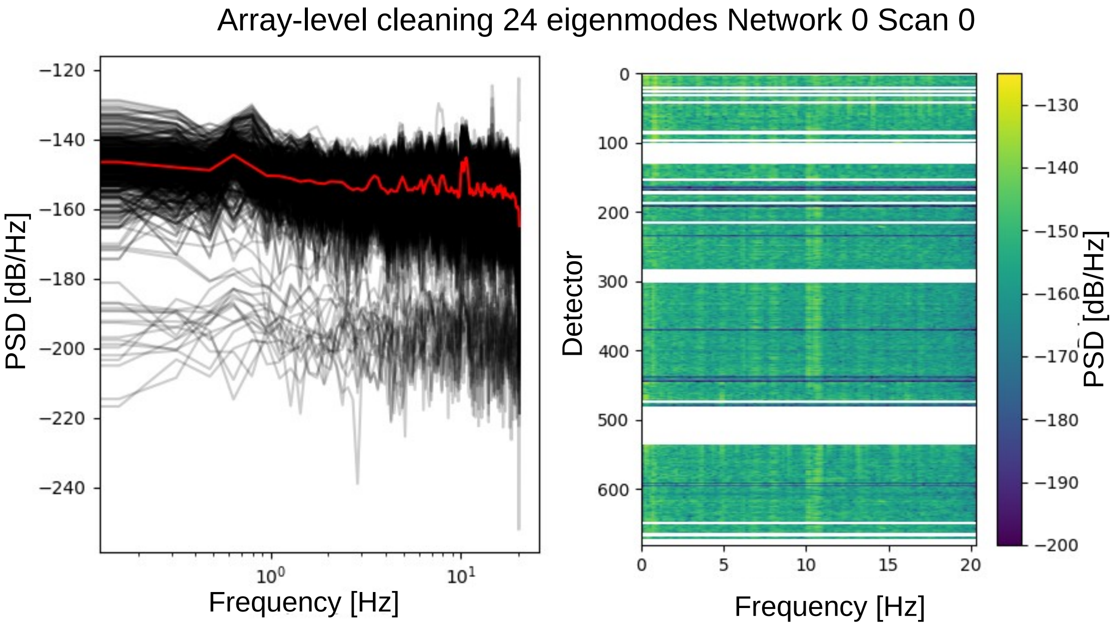

Figure 4.7: Power Spectral Density from Fig. 4.2 but not plotting all the detectors flagged by the alternate approach, using the median PSD-levels as a metric. This method flagged about 14 % of the detectors in Network 0 as bad

A quick comparison between the alternate "statistical" method proposed in this section (Fig. 4.7) and the one used by `citlali` shows that these two methods have a very similar effect on the data, however the statistical method only takes a single flagging parameter. The statistical method is deficient in flagging detectors with lower power levels mainly because they don't deviate as much from the median power spectrum than noisy detectors with abnormally high power levels (note all figures in this section have logarithmic axes). While `citlali` is better at flagging these cases the statistical approach is much more sensitive to noisy outliers.

4.2 Commissioning Maps

4.2.1 AGN observations

During the December 2022 commissioning run TolTEC observed two active galactic nuclei (AGN) 3C 147 and 3C 286. AGN are favorable first light objects for determining instrument systematics due to their extreme brightness (a few 100 mJy) at mm-wavelengths and high polarization of 10-20 % (Perley et al. 2013). Furthermore, AGN are common calibrators for most radio telescopes such as ALMA, the SMA, or the VLA and have been well measured at least in total intensity. This also means that this allows us to observe the polarization angle of these objects with a precision that is high enough to calibrate out any instrumental polarization, and to ensure that the polarization pipeline recovers polarization angles correctly.

Target	Time(UTC)	Integration time	Scan type	HWP	Usable
3C 147	Dec. 20th 4:24	5 min	Lissajous	Fixed	Yes
3C 147	Dec. 20th 4:39	10 min	Raster (V)	Rotating	No
3C 147	Dec. 20th 4:50	10 min	Raster (H)	Rotating	No
3C 147	Dec. 20th 5:01	10 min	Raster (V)	Rotating	No
3C 147	Dec. 20th 5:11	10 min	Raster (H)	Rotating	No
3C 147	Dec. 20th 5:22	10 min	Raster (V)	Rotating	No
3C 147	Dec. 20th 5:33	10 min	Raster (H)	Rotating	No
3C 147	Dec. 20th 6:07	5 min	Lissajous	Absent	No
3C 286	Dec. 20th 11:39	5 min	Lissajous	Absent	Yes
3C 286	Dec. 20th 12:09	5 min	Lissajous	Fixed	Yes
3C 286	Dec. 20th 12:20	10 min	Raster (V)	Rotating	No
3C 286	Dec. 20th 12:31	10 min	Raster (H)	Rotating	No
3C 286	Dec. 20th 12:42	10 min	Raster (V)	Rotating	No

Table 4.1: List of all AGN observations done with TolTEC in December 2022, the last column states if the observation was usable for polarization analysis or not. The HWP observations were done using a set of horizontal (H) and vertical (V) raster scans. None of these were usable due to a timing drift in the HWP rotator.

The two AGN were both observed in three modes once without the HWP using a 4′x4′ Lissajous, once with the HWP fixed at an arbitrary angle, again using a 4′x4′ Lissajous, and then multiple (the number was different for each quasar, due to time constraints) vertical and horizontal raster observations with the HWP in its continuously rotating mode. Each of the observing runs were about 5-10 minutes in duration. A list of all quasar observations is in Tbl. 4.1.

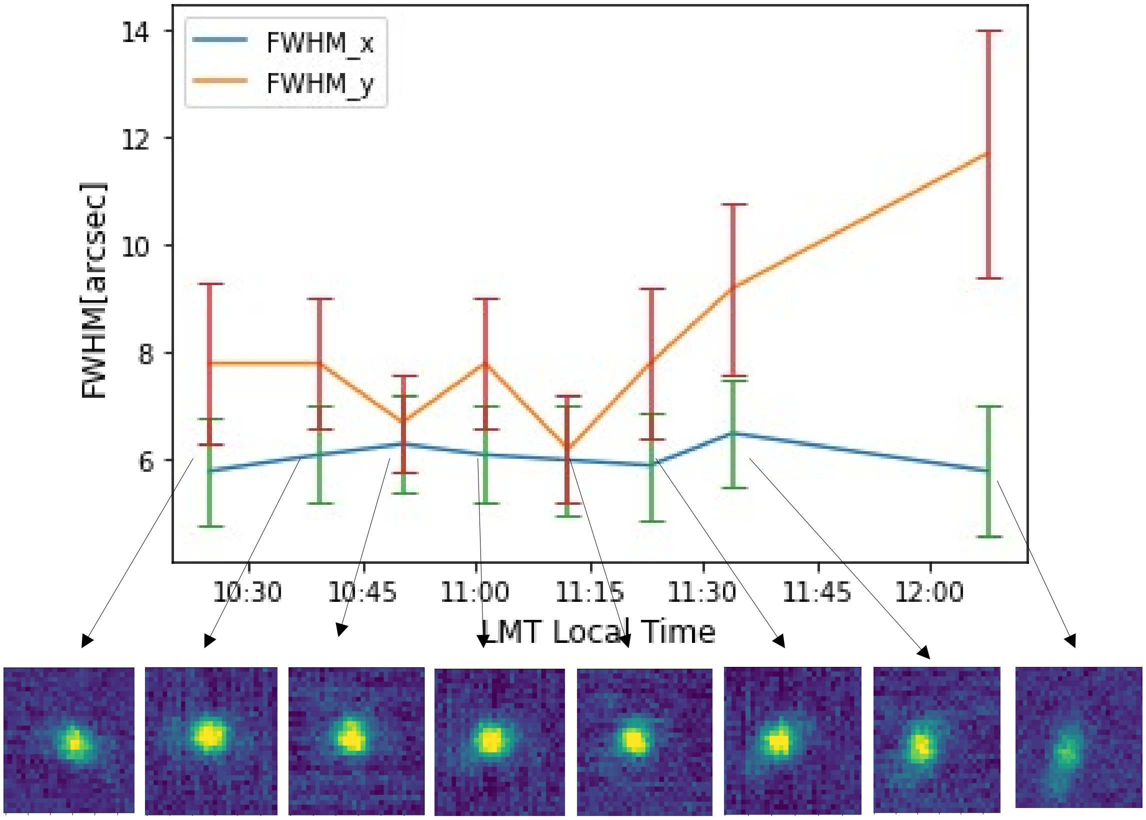

Figure 4.8: 1.1 mm beam full-width-half-maximum (FWHM) as a function of time for the observation of 3C 147. The degrading focus manifests itself in an increasing beam eccentricity and decreasing source flux. The x-major-axis was defined as the smaller axis. All values were obtained from least-squares fitting to each map of 3C 147. The first observation was done with the HWP fixed at an arbitrary angle and the last observation was done without any HWP. All others were done in HWP spinning mode.

Due to a timing drift in the HWP rotator the portion of the data with the continuously rotating HWP could not be used to recover polarized signal. Furthermore for 3C 147, the telescope lost focus over the course of the observing session (see Fig. 4.8) likely due to the telescope dish still thermalizing causing increased astigmatism, making only the first observation (with the HWP fixed) of this quasar usable for further polarimetric analysis. While most of the data for this object were not usable, this did indicate that data should be taken later during the night to let the dish thermalize. Furthermore, the total intensity data of this object demonstrated the ability of the Lissajous pattern (first and last observations of 3c 147) to reduce 1/f-streaking as compared to the raster scan (the middle six observations in Fig. 4.8).

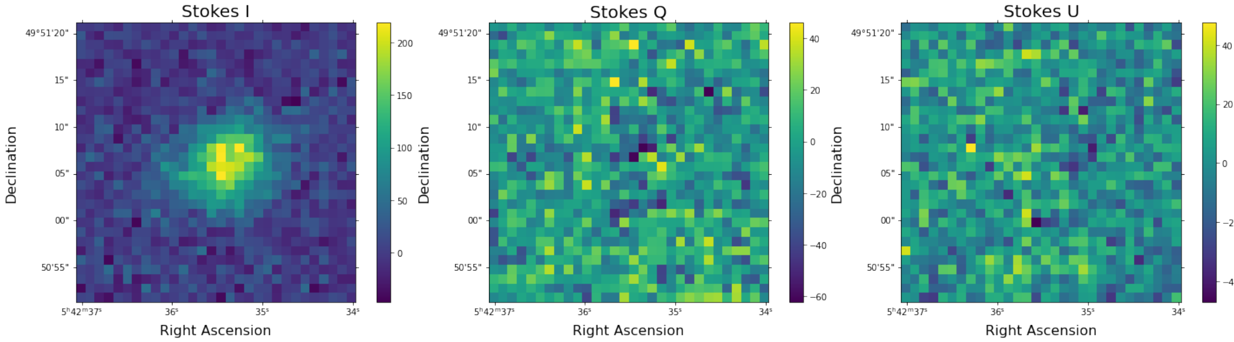

Figure 4.9: `citlali` polarization reduction applying PCA to all linear Stokes parameters for the 1.4 mm observation of 3C 147. There is no signal visible in the Stokes parameters. Given the trend in the polarization fraction at large wavelengths as measured by Perley et al. 2013, we would expect a polarization fraction of about 10% which should give a significant detection in these maps.

While the version of `citlali` compatible with simulated data gave reasonable results, the version of the code that was compatible with real instrument data as of yet has not been successful at recovering polarized signal even for the brightest of targets (See Fig. 4.9). However, for small targets there is a work-around for this, by noting that the Stokes parameters are recovered by differencing detectors with orientations orthogonal to each other. Therefore, with data that were taken with the HWP in a fixed state or removing the HWP entirely, this allows us to determine the Stokes parameters in the TolTEC array frame by computing

$$\begin{cases} Q_a = \frac{1}{2}(I_0 - I_{90}) \\ U_a = \frac{1}{2}(I_{45} - I_{135}) \end{cases} \tag{4.1}$$

where I_0, I_{90}, I_{45} and I_{135} are the total intensity measurements of the four different detector orientations of TolTEC. The factor of 2 in the denominator arises from the fact that `citlali` calibrates the output Stokes I maps under the assumption that the source is completely unpolarized and hence adds a factor of two to the timestreams.

The next step is then to rotate the polarization angle as defined in Eq. 2.3 from the array frame to the (universal) equatorial frame. Under the assumption that the parallactic angle (the angle between the azimuthal and equatorial coordinate systems) and elevation angle is constant over the course of the observation the polarization angle in the equatorial frame for TolTEC without the HWP is given by (as per private communication with Giles Novak)

$$\phi_{eq} = -\phi_a + \phi_{EL} + \phi_{PA} \tag{4.2}$$

where ϕ_a is the angle in the array frame, ϕ_{EL} is the elevation angle and ϕ_{PA} is the parallactic angle. The sign in front of the array-frame polarization angle arises from the odd number of mirrors in the optical path of TolTEC and the elevation angle is included here to account for the Nasmyth mount of the telescope which rotates the observed field by the elevation angle. If we include the stationary HWP then we have to mirror ϕ_a around the axis of the

HWP before plugging it into Eq. 4.2.

		I (mJy)	Q_a (mJy)	U_a (mJy)	$P = \sqrt{Q_a^2 + U_a^2}$ (mJy)	$p = P/I(\%)$
No HWP	1.1 mm	158 ± 2	-29 ± 3	-9 ± 4	30 ± 3	19 ± 2
	1.4 mm	169 ± 3	-30 ± 4	-4 ± 5	30 ± 3	18 ± 3
	2.0 mm	268 ± 2	-65 ± 3	-18 ± 3	67 ± 3	25 ± 2
HWP Fixed	1.1 mm	153 ± 2	5 ± 3	30 ± 4	30 ± 4	20 ± 3
	1.4 mm	167 ± 4	11 ± 4	31 ± 6	33 ± 6	20 ± 4

Table 4.2: Total intensity and array-frame polarized fluxes for the AGN 3C 286 as determined by Hailin Wang. The polarization fractions are in good agreement with Agudo et al. 2012 who report a polarization fraction of 14.4 ± 1.8 % at 1 mm.

	1.1 mm	1.4 mm
HWP fixed	-83 ± 4 deg (97 ± 4 deg)	-87 ± 5 deg (93 ± 4 deg)
no HWP	38 ± 4 deg (-140 ± 4 deg)	37 ± 5 deg (-143 ± 4 deg)

Table 4.3: TolTEC array frame polarization angles of 3C 286 as determined by Hailin Wang. The measured polarization fractions (see Tbl. 4.2) were in good agreement with Agudo et al. 2012. Given the difference in angle between observations with and without the HWP, we can say that the HWP axis (there is no way of telling which one is the fast and the slow axis) was located at an angle of 67 deg at 1.1 mm and 65 deg at 1.4 mm. The angle in brackets has been rotated by 180 degrees, to account for the absence of directional polarization information.

Work done by Hailin Wang on the commissioning data for 3C 286 (see Tbl. 4.2 for a full breakdown of all the fluxes), which had usable data for both the fixed and no HWP case demonstrated that the HWP axis was rotated about 67° at 1.1 mm and 65° at 1.4mm for all observations (the fixed orientation of the HWP was kept the same for both 3C 147 and 3C 286). Given that the uncertainty in the angle in Tbl. 4.3 is a few degrees these two angle measurements are in good agreement with each other. A measurement at 2.0 mm was not obtained because the HWP only works at the 1.1 and 1.4 mm bands. Only the observation with the HWP fixed at an angle was usable for the above analysis due to an increase in astigmatism in the telescope optics. Images of the quasar in the three Stokes parameters can be seen in Fig. 4.10. In order to determine the flux in Stokes I, Q and U, aperture photometry was applied to each of the maps (the apertures used for flux and background

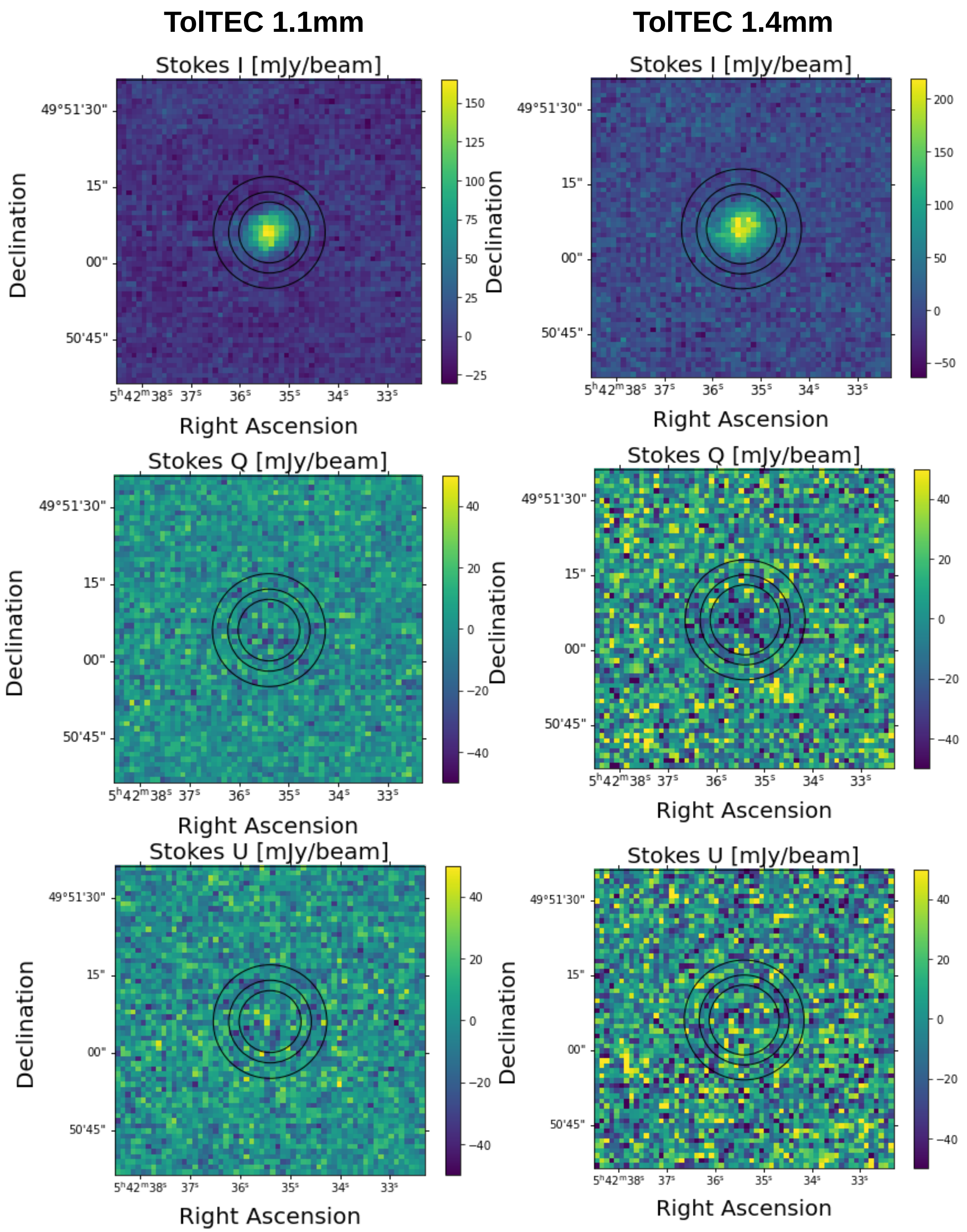

Figure 4.10: Map of the AGN 3C 147 at two of the three TolTEC bands. The 2.0 mm data is not shown because it is beyond the operating range of the HWP, which is installed at an arbitrary angle for this observation. The Stokes Q and U parameters were computed as in Eq. 4.1 and therefore show the polarization as seen by the array rather than the on-sky polarization. the black rings depict the aperture and annulus used to do the aperture photometry. Unlike the `citlali` reduction in Fig. 4.9 there is a faint feature in Stokes Q at 1.4 mm.

information are denoted by black rings in Fig. 4.10) and from there the angle in the array frame as well as the polarization fraction was determined.

	I (mJy)	Q_a (mJy)	U_a (mJy)	$P = \sqrt{Q_a^2 + U_a^2}$ (mJy)	$p = P/I(\%)$
1.1 mm	160 ± 4	-8 ± 4	4 ± 5	9 ± 5	6 ± 3
1.4 mm	184 ± 4	-17 ± 6	0 ± 6	17 ± 6	9 ± 3

Table 4.4: Aperture photometry results for the 3C 147 reduction presented in Fig. 4.10. Q_a and U_a are the Stokes Q and U measured in the frame of the TolTEC array.

The array-frame Stokes parameters Q_a and U_a for 3C 147 as well as the polarized intensity P and the polarization fraction p can be seen in Tbl. 4.4. For the 1.1 mm array there is a 2σ detection of the polarization and at 1.4 mm the detections are barely 3σ. One important thing to note here is that according to the SMA calibrator list [1] we should expect a flux of 360 mJy this hence points to a calibration error, nonetheless we can still expect to recover the correct polarization fraction and angle as any kind of calibration is divided out in those calculations. The same holds true for 3C 286 Agudo et al. 2012 report a point source flux of 0.30 ± 0.03 Jy at 1 mm which is about a factor of two higher than the 158 ± 2 mJy reported by Hailin Wang.

The angles in the array frame and equatorial frame for 3C 147 can be seen in Tbl. 4.5. While the uncertainty ranges of the angles overlap mainly due to the low-σ detections on the polarized intensity for this dataset further observation is required to improve the signal-to noise and give a more conclusive answer.

Unlike 3C 286 which is a primary polarization calibrator for most radio facilities whose flux is well measured in the millimetre (Agudo et al. 2012), the polarized flux for 3C 147 is unknown for wavelengths shorter than 7 mm. Perley et al. 2013 report a polarization fraction

---

[1] `http://sma1.sma.hawaii.edu/callist/callist.html`

	Pol. Angle (array frame, deg)	Pol. Angle (equatorial frame, deg)
1.1 mm	77 ± 16 (-103 ± 16)	-135 ± 16 (45 ± 16)
1.4 mm	-88 ± 10 (92 ± 10)	60 ± 10 (-120 ± 10)

Table 4.5: Polarization angle for the 3C 147 data presented in Fig. 4.10 in both the array frame and the equatorial frame. The angles in brackets are the polarization angles shifted by 180°, to account for degeneracy induced by the absence of the directional information of the polarization vector. All angles are defined on $(-180°, 180°)$ where $(0°)$ is North in equatorial coordinates or "up" in azimuthal coordinates. The observations were taken at a mean parallactic angle of -134 degrees and a mean elevation of 52 degrees.

of 5.2% at 7 mm with an increasing trend towards shorter wavelength and an angle of 86 degrees, again, with an increasing trend towards the millimetre range. While the polarization fractions found by TolTEC may be realistic under the assumption that the trend in Perley et al. 2013 continues beyond 7 mm (and is expected to reach about 10% in the TolTEC bands), the 3σ threshold on these detections is barely reached and we should therefore not consider them significant. The polarization angle measurement, which does not seem to reconcile well with the increase reported by Perley et al. 2013, should therefore also be disregarded as the uncertainty in the angle can be related to the signal-to-noise in the polarized intensity by Eq. 3.8. To conclude, we need more observations to make a more definite statement on the polarization of 3C 147 at millimetre wavelengths.

4.2.2 The Crab Nebula

So far in this section I have mostly focused on point sources rather than extended emission. However, since two of the legacy surveys (the Fields in Filaments Survey and the Clouds to Cores survey) require detailed maps of extended emission, it is important to study this aspect as well. During the December 2022 commissioning run TolTEC also observed the supernova remnant M1 also known as the Crab nebula.

One important study to apply to these maps is Fourier Analysis to study the recovery of spatial scales. By the time TolTEC resumed commissioning in December 2022 there was a significant effort by Joey Golec to use the maximum-likelihood map-maker `minkasi`[2] (written by Jonathan Sievers) on TolTEC data. Unlike the naive map-making approach which just assigns pixels to data and takes a weighted average, the maximum likelihood map-maker uses a naive map as a prior to find the likeliest map given the raw data, and will therefore give different results from the simple naive approach combined with PCA cleaning. It hence is instructive to compare the naive map-making approach in `citlali` with `minkasi` in the Fourier plane and to compare the recovered spatial scales. A comparison between the two map-making approaches can seen in Fig. 4.11.

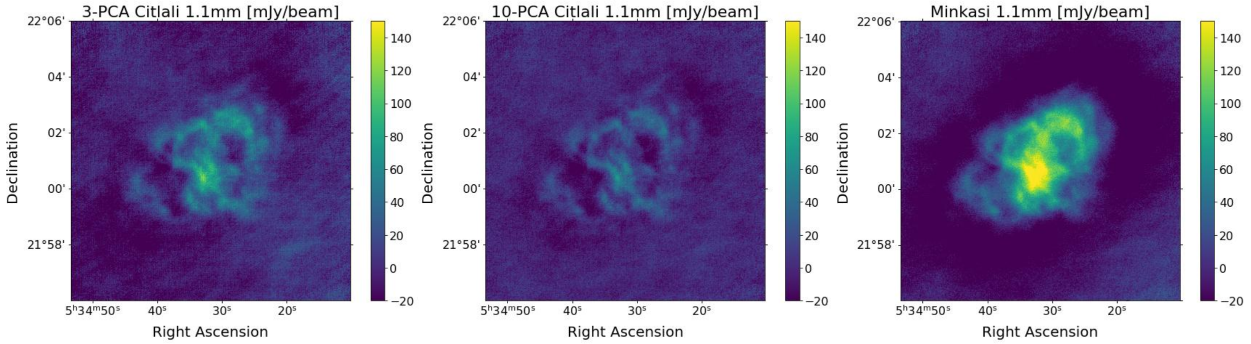

Figure 4.11: *Left*: `citlali` 1.1 mm map of M1 removing 3 eigenmodes network-level when applying PCA. The streaking in the map is an artefact produced by 1/f noise in combination with the raster scan (Reduced by: Michael McCrackan, Felix Thiel). *Middle*: The same M1 map as reduced by `citlali` however, this time removing 10 eigenmodes network-level, note the reduction in flux and the increased spatial filtering (Reduced by: Michael McCrackan, Felix Thiel). *Right*: 1.1mm map of M1 using `minkasi` as a mapmaker. Note the absence of the streaking features and the presence of large scale extended emission (Reduced by: Joey Golec). About 22.5 minutes of data went into these maps, which are a co-addition of raster scans at 0°,45°,90° and 135°

Radial Fourier spectra for both the `citlali` and `minkasi` maps can be seen in Fig. 4.12. Just as in the maps in Fig. 4.11 there are more recovered large spatial scales in the `minkasi`

---

[2] `https://github.com/sievers/minkasi`

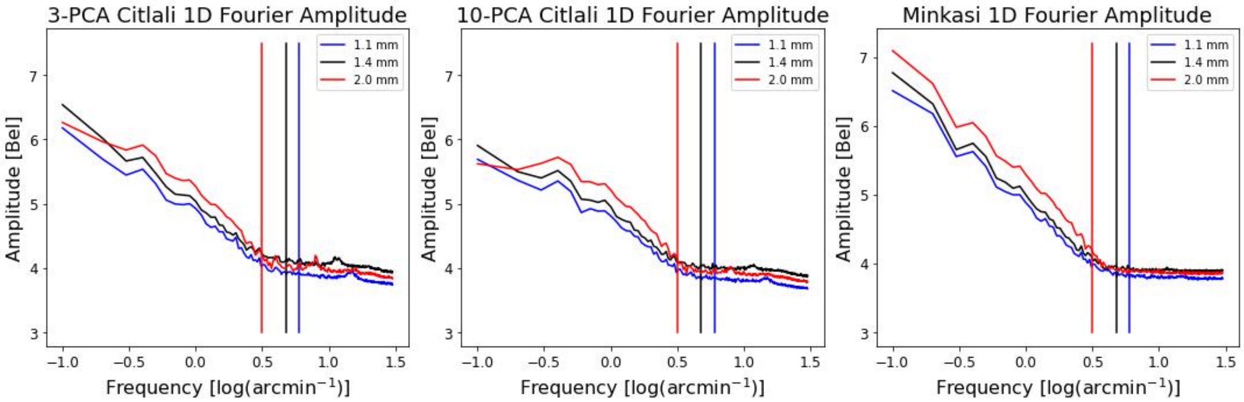

Figure 4.12: Average radial Fourier Amplitude for both the `citlali` (*Left* and *Middle*) and `minkasi` (*Right*) maps in Fig. 4.11 at the three TolTEC bands at 1.1 mm (blue) 1.4 mm (green) and 2.0 mm (red), the vertical lines indicate the theoretical TolTEC beams at the respective bands. The noise levels of the 1.4 and 2.0 mm bands are higher than the 1.1mm band because there are less detectors in those arrays. The 1.4 mm band is the highest because one network on this array was dark for commissioning.

maps. The `minkasi` maps contain about 5 dB more large scale structure than the 3-eigenmode `citlali` map and about 10 dB nore than the 10-eigenmode maps. As was demonstrated in Sec. 3.1.2, using simulations, an increase in the removed number of eigenmodes during PCA increases the spatial filtering of the final data product.

We have to be careful however what this large scale structure is attributed to, as only 3 eigenmodes were removed for one of the `citlali` reductions the large spatial scales may be artificially blown up by residual atmospheric 1/f noise. The high-frequency end of the `citlali` spectra hints at this residual 1/f noise power by the presence of a slight slope in the noise levels along with spikes from the streaking that is visible in Fig. 4.11. For the `minkasi` maps however, the high-frequency noise level is flat and the spikes are barely visible anymore (there is a slight bump in the 1.1mm spectrum). The maximum-likelihood approach therefore seems to be much more efficient at mitigating 1/f noise than the naive approach in `citlali`. Futhermore, in order to acheive noise properties that are even remotely similar to that of the `minkasi` map we lose a lot more spatial scales in the equivalent `citlali` map.

All in all, `minkasi` seems to be better at recovering spatial scales than `citlali`, computing a cutoff spatial scale as in Sec. 3.1.2 is not possible because we don't have a "truth" to compare our results to. The maximum-likelihood mapmaker performs a lot better when it comes to reducing 1/f-noise seen by the absence of streaking features from the mapping pattern. Lastly, the relative performance of `citlali` to `minkasi` will depend on the number of eigenmodes that are removed at the PCA-cleaning stage. While we cannot constrain cutoff frequencies using the same method as in Sec. 3.1.2, the overall trend of increased spatial filtering with increased eigenmode removal is at least qualitatively consistent with simulations. Future work will have to involve reducing simulations such as those in Sec. 3.1.2 with `minkasi` for a more quantitative comparison.

4.3 Next Steps for TolTEC

After December 2022, observing with TolTEC came to a stop due to a forest fire on Sierra Negra in Febuary 2023, a series of power outages throughout the winter, as well as a volcanic eruption of Popocatépetl near Mexico City in May 2023. Any further commissioning efforts are set to resume in the Fall of 2023 due to the typically humid atmospheric conditions in the Summer. Nonetheless improvements to the instrument could be made most importantly the timing drift of the HWP rotator was resolved in the meantime.

On the observational end, next steps include more observations of 3C 286 with the HWP in spinning mode, to determine the reduction of 1/f noise using this technique. This will also allow us to better constrain instrumental polarization. Furthermore, while significant efforts by the TolTEC polarization working group are underway to recover polarized signal due to synchrotron emission (Ritacco et al. 2018, and references therein) from the M1 observations, it will be instructive to observe fainter extended targets like perhaps NGC 1333 using the HWP in spinning mode to test the sensitivity limits of the instrument. Lastly, more observations of 3C 147 would help confirm or disprove the low signal-to-noise polarization detection of 3C 147 demonstrated in Sec. 4.2. Further observation of this quasar would make for an excellent science case as its polarization properties have never been observed at these wavelengths.

The analysis in Sec. 4.2 is only scratching the surface and there is still more work to be done, in particular when it comes to the polarization pipeline which to date is not giving reasonable answers when trying to reduce polarized signals. Furthermore, as demonstrated by the analysis on AGN in Sec. 4.2 we are still missing a factor of about 2 in point source calibration, this issue will have to be investigated in the future. Finally, while the current naive map-making approach may be sufficient for point source recovery, maximum-likelihoood mapmakers like `minkasi` may be a better option for recovering extended Stokes I emission especially for the Fields in Filaments survey. Nonetheless, further investigation is required to determine how much of this large scale structure is cosmic signal for both the map-making approach in `citlali` and `minkasi`. In the future it will also be helpful to compare the `minkasi` results to the maximum-likelihood mapmaker in the TOAST3 module.

The lessons learned from commissioning TolTEC will be extremely valuable when it comes to reducing science ready maps for the Fields in Filaments legacy survey. These maps will hopefully provide useful insights at unprecedented resolution into critical densities as well as critical scales on which the gas motion is dominated by the gravitational force rather than the magnetic field.

Chapter 5

Improving VLBI with BVEX

In the previous chapters we have seen an example of a single dish experiment using incoherent detectors that directly measure power rather than the electric field. In this chapter I will be discussing an experiment currently under development that will make use of Very Long Baseline Interferometry (VLBI) to observe a target, this requires recording wave-forms and therefore requires a heterodyne receiver, which measures electric field rather than power. I will be giving an overview of the science background and motivation for this experiment as well as design requirements and challenges. I will also be discussing my design for the K-band receiver.

5.1 Motivation

In 2019 the Event Horizon Telescope (EHT) released the first ever image of the black hole at the centre of M87 (see rightmost plot in Fig. 5.3), followed by yet another observation of Sagitarius A* the black hole of our own galaxy (Event Horizon Telescope Collaboration

2019; Event Horizon Telescope Collaboration 2022). In order to do this the EHT made use of a technique called Very Long Baseline Interferometry (VLBI) at a frequency of 230 GHz (1.3 mm) using different radio telescopes all over the world.

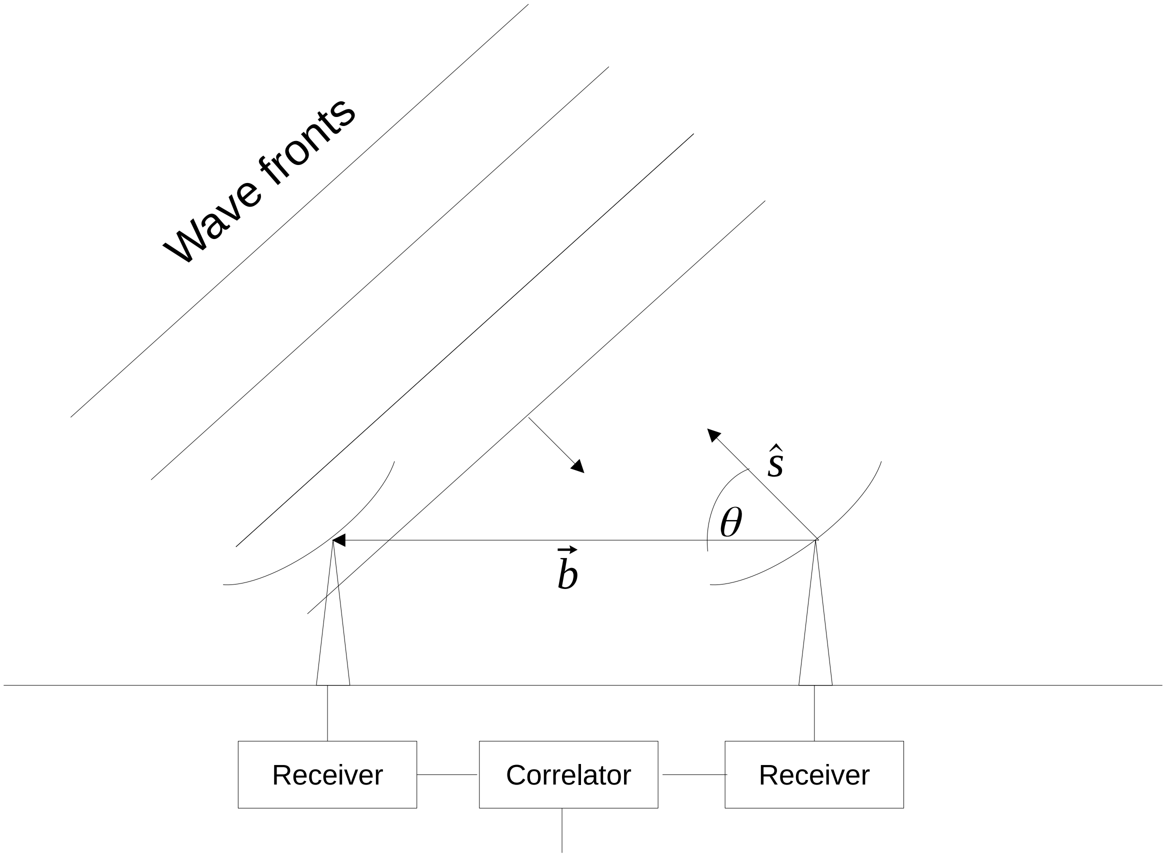

Figure 5.1: Schematic of a 2-element interferometer. The wavefronts from a distant point source will reach the two telescopes at different times set apart by the delay $\Delta t = \left(\vec{b} \cdot \hat{s}\right) / c = b \cos(\theta) / c$. Depending on the elevation angle θ of the telescopes the signals will either interfere constructively or destructively, giving a sinusoidal power pattern on the sky. The telescopes will therefore measure one Fourier component of the sky signal (a point source in real space appears as a sine wave in Fourier space). To fully reconstruct the signal we would need multiple dishes at different baselines which themselves have different orientations with respect to the source to better sample the Fourier plane (Figure adapted from Condon et al. 2016).

When conducting VLBI we observe a target simultaneously using multiple single dish telescopes (see Fig. 5.1). The wave-forms are then recorded by the receiver and correlated after observation. Unlike a single dish this does not yet give us an image. For the two-element interferometer in Fig. 5.1 the signals will phase into and out of existence due to inteference as the telescopes move across the sky to track the source. The power pattern on the sky therefore is sinusoidal and not Gaussian as for a single dish telescope. Hence, one baseline gives us one Fourier component of the actual image. The measured Fourier transform of the image is also called the visibility which for a monocromatic two-element interferometer (on a flat surface) is given by

$$\mathcal{V} = \int I(\hat{s}) \exp\left(i2\pi\vec{b}\cdot\vec{\hat{s}}/\lambda\right)\, d\Omega \tag{5.1}$$

where λ is the observing wavelength, $\vec{b}$ is the baseline vector and $\hat{s}$ is the vector of the telescope pointing.

Because a single baseline only gives us a single spatial scale at a given time we generally need multiple telescopes to better sample the Fourier plane. For another, the orientation of the baseline on the sky determines the direction in which features are recovered. We therefore define a set of new coordinates u and v which correspond to the East-West and North-South components of the baseline on the plane of the sky respectively (which is why the Fourier plane in this context is often referred to as the u-v plane). These coordinates are dimensionless as they are typically given in terms of wavelengths. The visibility in terms of these coordinates (for observing small regions) is given by:

$$\mathcal{V}(u,v) = \int\int \frac{I_\nu(l,m)}{\sqrt{1-l^2-m^2}} \exp\left(-i2\pi(ul+vm)\right)\, dl\ dm \tag{5.2}$$

where l, and m are direction cosines related to the declination by

$$\sin(\delta) = \sqrt{1 - l^2 - m^2}. \tag{5.3}$$

Because the sky is a spherical surface this formalism is an approximation for mapping regions smaller than a radius of $\sqrt{\lambda/b}$ where b is the longest projected baseline and λ is the observing wavelength. The on-sky brightness distribution can then be recovered by taking an inverse Fourier transform of the visibility. The expression in Eq. 5.2 also tells us that the smallest scale in the final image will be dominated by the longest baseline and is therefore given by Eq. 1.1 where the length d is given by the longest projected baseline of the array. At the same time (unlike single dish telescopes) we also have a largest scale which is set by the shortest baseline and can again be determined using Eq. 1.1 by replacing d with the shortest baseline. Interferometers therefore are spatial filters: If the individual stations are drawn apart we recover more small scales and less large scales resulting in a decrease in signal-to-noise.

Similarly if we move the individual stations closer together we will recover more large scales and fewer small scales resulting in an increase in signal-to-noise. It is therefore important to have long and short baselines in multiple directions to get good coverage of the u-v plane. The other way to get good u-v coverage is to use the rotation of the earth to sample different parts of the plane in a process called Earth-rotation aperture synthesis. As shown in Fig. 5.2 the on-sky orientation of an east-west baseline changes to north-south as the earth rotates, and therefore traces out an ellipse in the u-v plane.

The EHT as it stands right now is limited in resolution due to two factors. If the longest

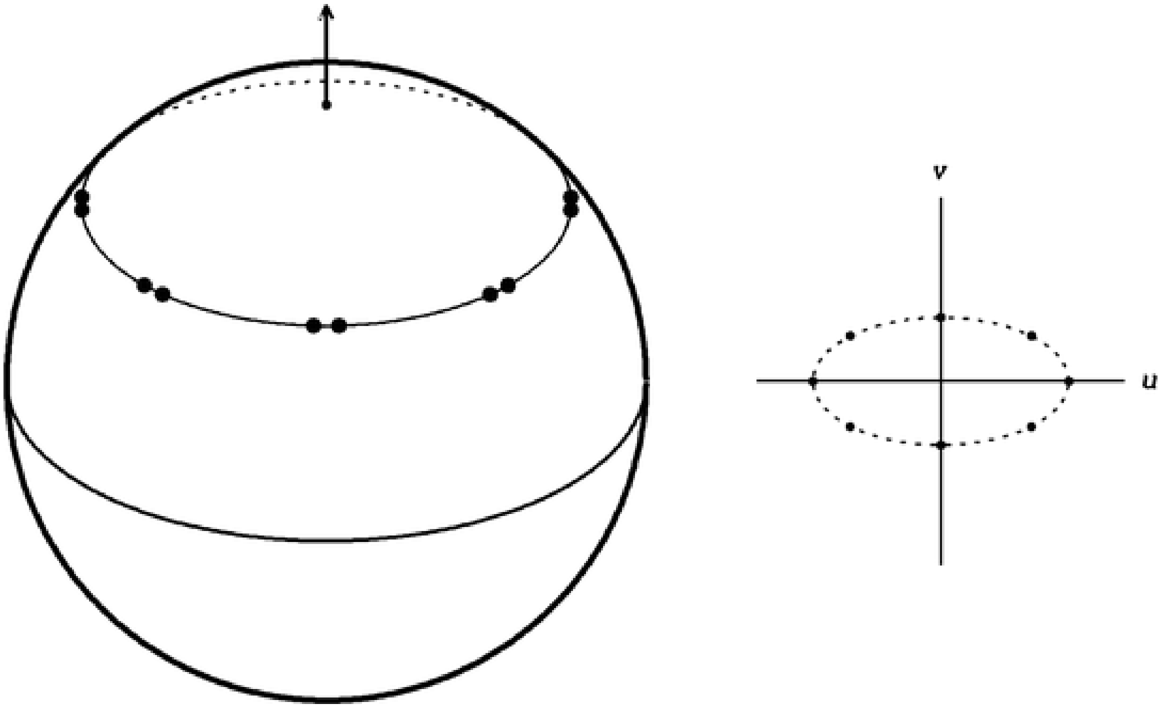

Figure 5.2: Schematic reproduced with permission from Condon et al. 2016 demonstrating Earth-rotation aperture synthesis: The on-sky orientation of an east-west-baseline slowly changes from east-west to north-south and therefore traces out an ellipse in the u-v plane.

baseline of the interferometer already is the size of the Earth, it can only be improved by moving VLBI stations into space. The second way we can increase the resolution is to observe at a shorter wavelength (or higher frequency), however, at higher frequencies molecular absorption makes science-quality observations close to impossible in most ground-based locations impacting the u-v coverage. This would again, require the need for space-based VLBI. Because space missions are extremely costly the other option for observing at shorter wavelengths (or higher frequencies, which effectively increases the resolution) is to observe from a stratospheric balloon cruising at altitudes of about 20-40 km where most of the atmosphere is below the telescope. At 690 GHz (assuming a 10^{-2} Jy sensitivity) this would allow us to image about 5 times as many black holes as with the current configuration of EHT (see leftmost panel of Fig. 5.3) (Johnson et al. 2019).

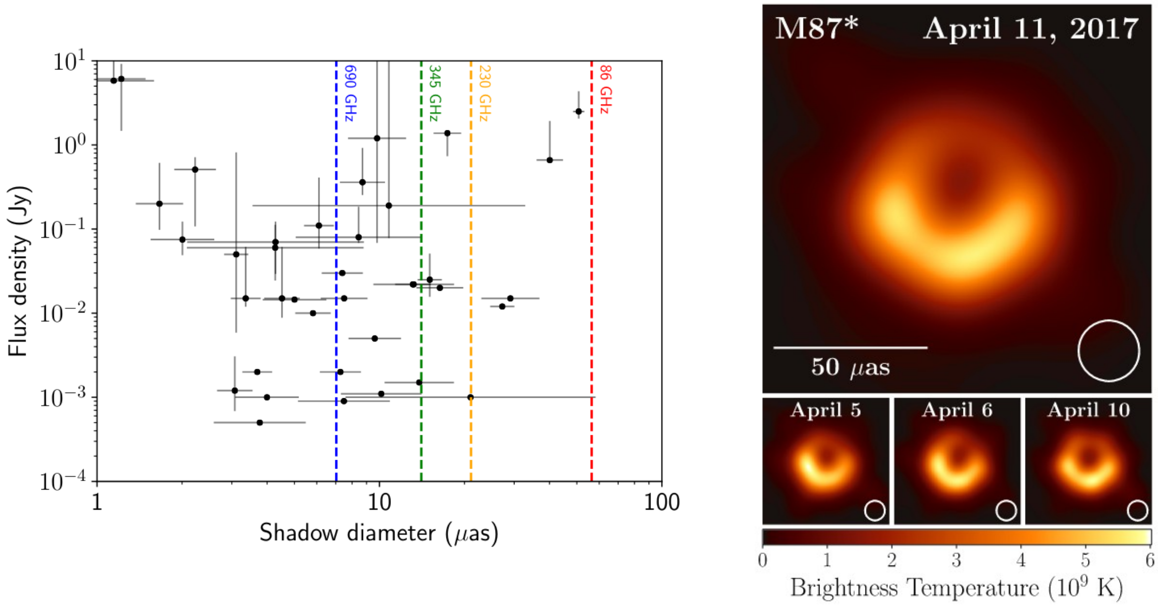

Figure 5.3: *Left*: Plot of the black hole brightness as a function of shadow diameter from Johnson et al. 2019. The vertical lines indicate the resolution of an EHT-sized interferometer at 86 (red), 230 (yellow), 345 (green), and 690 GHz (blue). The current operating frequency of EHT is 230 GHz. *Right*: First ever image of the black hole M87* from Event Horizon Telescope Collaboration 2019.

The aim for a balloon-borne VLBI station will therefore be to increase the resolution by increasing the observing freqeuncy rather than the baseline as would be the case for space VLBI. Lastly, the current EHT is mostly relying on Earth-rotation aperture synthesis to sample the u-v plane. A balloon-borne VLBI station could therefore give access to many different locations on the u-v plane which currently are inaccessible due to the fact that it is a non-stationary environment.

5.2 BVEX: The Balloon-borne VLBI Experiment

In order to demonstrate VLBI from a balloon-borne platform the Balloon-borne VLBI Experiment (BVEX) will be launched from the Canadian Space Agency's scientific balloon base in Timmins, Ontario, Canada in 2025. This balloon-borne telescope will be a prototype operating at K-band (22 GHz, 1.3 cm), whose goal will be to make significant detections of interference fringes by partnering with a ground based station and to demonstrate that the baseline to the partner station can be tracked accurately enough to conduct VLBI at 230 GHz, which is the current EHT operating frequency. BVEX will consist of a 36 inch (91 cm) K-band radio telescope with a collecting area of about 0.43 m^2 and 2 GHz of bandwidth. A detailed break-down for the high-level radio telescope specifications can be seen in Tbl. 5.1.

Dish diameter	91 cm
Radio telescope beamsize	1°
Central operating frequency	22 GHz
Bandwidth	2 GHz
On-axis collecting area	0.43 m^2
Aperture efficiency	66%

Table 5.1: Specifications of the radio telescope that is part of the BVEX payload.

5.2.1 Design Requirements and Challenges

In radio astronomy we often measure signals in both units of flux (i.e. Jy) and temperature (i.e. K). One important quantity to consider is the noise temperature of the telescope, which is the temperature equivalent to the noise power per unit bandwidth that would be generated by an impedance matched resistor connected to the receiver input. In other words, if we were to attach a 50 Ω resistor to a 50 Ω receiver then the noise temperature seen by the receiver will be the physical temperature of the resistor. The flux-equivalent of this is the system equivalent flux density (SEFD) defined as

$$SEFD = \frac{2kT_{sys}}{A_0} \tag{5.4}$$

where T_{sys} is the system noise temperature and A_0 is the on-axis collecting area. In other words, the SEFD is the flux of a point source generating the same amount of power as the noise. The RMS of a measurment on a given baseline between two VLBI stations is then given by

$$\sigma_{rms} = \eta_Q^{-1}\sqrt{\frac{SEFD_1 SEFD_2}{2\Delta\nu\tau}} \tag{5.5}$$

where η_Q is an efficiency that arises from quantization of the wave-forms, $SEFD_1$ and $SEFD_2$ are the SEFD's of the two stations as defined in Eq. 5.4, $\Delta\nu$ is the bandwidth and τ is the integration time (typically 1s for VLBI). The sensitivity of an interferometer therefore depends on the geometric average of the SEFD's of the individual VLBI stations. This therefore allows us to reduce the dish diameter of one of the telescopes down to a scale that will fit on the gondola of a stratospheric balloon, so long as the ground-based station has a dish that is sufficiently large to bring down the overall RMS. Because the IF-backends for BVEX will be re-quantizing the recorded wave forms to 2-bits in order to stay compatible with the correlator software we will be assuming $\eta_Q = 0.88$ (Thompson et al. 2017). Furthermore, we conservatively assume that we lose half our bandwidth to radio frequency interference and will therefore assume a bandwidth of 1 GHz as far as sensitivity is concerned. As of this point we don't have a good measure of spillover for the BVEX dish, which is a phenomenon where the side-lobes of the dish pick up thermal radiation from the ground. This effect will have to be quantified, and perhaps even controlled (through the use of a baffle) in the future. In the stratosphere we expect the atmospheric noise to be negligible compared to the cosmic microwave background with $T_{CMB} = 2.73$ K. Under these assumptions the over-all system noise temperature for BVEX will be given by

$$T_{sys} = T_r + T_{CMB} \tag{5.6}$$

where T_r is the receiver noise temperature. Combining Eq. 5.4,5.5 and 5.6 we can then determine an upper bound for the BVEX receiver temperature assuming a given partner station and source.

Because interferometry spatially filters signals it is therefore advisable to observe compact and bright point sources. More specifically we plan to observe distant active galactic nuclei (AGNs) due to their radio brightness, which are used as calibrators by the Very Long Baseline Array (VLBA) to ensure that these sources will appear as point sources on our baseline. Generally the flux seen on a particular baseline decreases with increasing baseline length. To be conservative we hence set an upper bound of 5000 km for our observations. BVEX will launch from Timmins, Ontario and therefore, in order to keep the baseline below this 5000 km limit we will partner with telescopes on the North American continent. The two candidates for this are the Green Bank Telescope (GBT) with a 17 Jy SEFD [1] giving an initial baseline of about 1100 km and one of the VLBA stations with a 640 Jy SEFD[2], preferably the station in Hancock, New Hampshire giving an initial baseline of about 950 km. However

---

[1] `https://www.gb.nrao.edu/scienceDocs/GBTpg.pdf`

[2] `https://science.nrao.edu/facilities/vlba/docs/manuals/oss/bands-perf`

this latter baseline could increase depending on the availability of VLBA stations at launch and weather conditions. A list of upper bounds on the receiver noise temperature, assuming that we want a $> 3\sigma$ detection with 1 GHz of bandwidth in 1 s, for a variety of targets can be found in Tbl. 5.2.

	3C 454.3	3C 279	3C 84*	3C 273*
GBT	9.6×10^4 K	1.3×10^5 K	4.2×10^3 K	1.4×10^4 K
VLBA	2.5×10^3 K	3.4×10^3 K	1.0×10^2 K	3.8×10^2 K

Table 5.2: Upper bound for the BVEX receiver temperature assuming a 3σ detection of the given target using the GBT or the VLBA station as a partner station. All of these sensitivity calculations were done using fluxes on a 5000 km baseline from the VLBA calibrator search tool (`https://obs.vlba.nrao.edu/cst/`). The asterisk indicates the use of Ku-band (2 cm) fluxes.

The upper bounds in Tbl. 5.2 demonstrate that when partnering with the right telescope the sensitivity requirement for BVEX is extremely flexible, and can easily be achieved with off-the-shelf components. The receiver was therefore designed based on the best available components that would fit within the budget. This is also due to the fact that K-band is rarely used for satellite communications due to the water maser absorption line at 22.35 GHz, this naturally limits the options for readily available off-the-shelf components.

Another more challenging design consideration, arises from the fact that BVEX will not be a stationary VLBI station because it is suspended from a stratospheric balloon. The baseline to a ground based station therefore also is constantly changing. In order to keep the error in the phase shift to less than a radian the baseline needs to be tracked to a precision of

$$|\vec{r}| < \frac{\lambda}{2\pi} \tag{5.7}$$

where λ is the observation wavelength. Therefore at K-band we need a precision of at least

2 mm and at 230 GHz (1.3mm) a precision of at least 0.2 mm. BVEX will therefore use a set of accelerometers whose signals will be integrated to track changes in position. This data will then be fused with attitude solutions from the star camera along with gyroscope and GPS data to determine the initial velocity and position and to transform from the gondola's frame to the celestial frame. While the problem of position tracking is an interesting problem on its own, the remainder of this section will focus on my design of the K-band receiver and future work.

5.2.2 The K-band Receiver

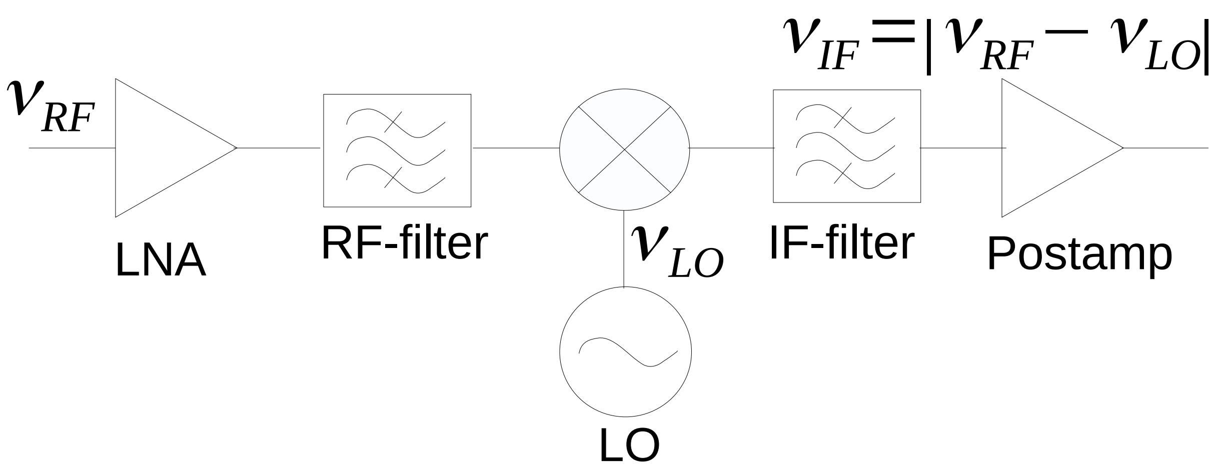

Figure 5.4: High-level schematic of a heterodyne receiver. The radio frequency (ν_{RF}) is amplified by the low-noise amplifier (LNA) and filtered by the bandpass filter, this signal is then mixed with the Local Oscillator (LO) signal at frequency ν_{LO} which gives two frequencies $\nu_{RF} + \nu_{LO}$ (which is filtered off by the IF-bandpass) and $|\nu_{RF} - \nu_{LO}|$ which is also known as the intermediate frequency (IF).

The backends for most radio telescopes use the same receiver setup called a heterodyne receiver (Fig. 5.4): The incoming cosmic signal is focused onto the antenna by the telescope dish, this signal is then converted to current by the antenna and amplified by a low-noise amplifier (LNA). Because most radio signals are too high in frequency to be sampled directly and to avoid significant amounts of attenuation the signal is then mixed with a sinusoidal signal from a local oscillator (LO), this splits the signal into two bands at frequency $|\nu_{LO} - \nu_{RF}|$ and $\nu_{LO}+\nu_{RF}$, the latter is filtered off, leaving the difference between the radio frequency (RF) and LO frequency which is much easier to sample than the RF, this frequency is called the intermediate frequency (IF). Therefore, when designing a heterodyne receiver there are multiple design considerations, such as operating frequencies, receiver noise temperature, and overall receiver gain. In particular, for BVEX we want a receiver built from cheap off-the-shelf components that has noise properties below the bounds in Tbl. 5.2 and the best possible phase stability that fits into the budget for the experiment.

Image rejection

As mentioned in the previous paragraph a heterodyne receiver takes the input radio frequency ν_{RF} and down-converts the signal to an intermediate frequency ν_{IF} using the local oscillator with frequency ν_{LO}. The desired ν_{IF} and ν_{LO} primarily depend on the ν_{RF} and the receiver bandwidth $\Delta\nu$, which is bounded from above by the Nyquist frequency. In other words if we sample at frequency f_{smp} the highest bandwidth we can achieve is $\Delta\nu = f_{smp}/2$.

In the case of a receiver with an ideal RF-filter (of bandwidth $\Delta\nu$) we would down-convert to base-band, that is, to $\nu_{IF} = (0, \Delta\nu)$. For real RF-filters we have to be more careful. Note, that the IF frequency is given by the absolute difference between the RF and the IF-frequency and we therefore have two RF-bands that get mapped into the same

IF-frequency $\nu_{LO} + \nu_{IF}$ and $\nu_{LO} - \nu_{IF}$ which are referred to as the upper side-band and lower side-band respectively. The side-band that does not coincide with the desired RF-frequency is also referred to as the image. Now, if the IF-frequency is base-band these two frequency-bands are adjacent to each other. In the case of an ideal RF-filter one of the side-bands will be rejected. However, in the case of a non-ideal RF-filter there will be leakage from beyond the operating frequency, and part of the image will get mapped into the IF frequency (see

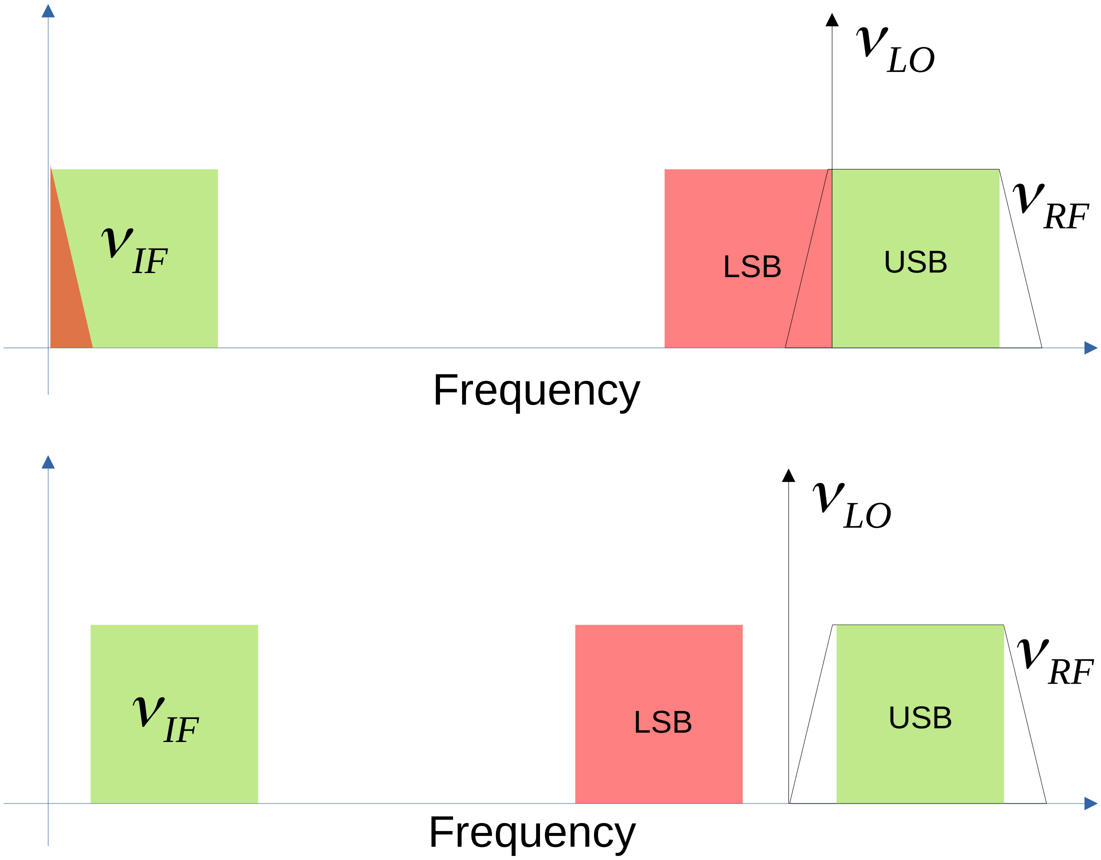

Figure 5.5: Image rejection in an upper side-band receiver. If we try to down-convert directly to base-band (*Top*) using a non-ideal RF-bandpass (Trapezoidal shape) part of the lower side-band (LSB, in this case the image) will leak into the IF-frequency. However, if we drop the LO frequency (*Bottom*) we won't be down-converting to baseband (hence the higher IF) and we only get the desired upper side-band (USB).

Fig. 5.5). Therefore, direct down-conversion to base-band is not feasible in practice because it does not completely reject the image. We therefore have three options. The first is to receive both side-bands in two different IF-outputs and build a system as in Finger-Camus 2013. While this doubles the bandwidth of the receiver it is extremely expensive as we need roughly twice the amount of components. Furthermore,we would have to store twice the amount of data which is challenging when operating from a balloon. The second option is to down-convert twice as is the case for most research grade telescopes that were built in the 20th century. This approach first down-converts to a level where the image is easily rejected and then takes that signal and down-converts to base-band using a second mixing chain. The third option is to not down-convert to base-band but rather some higher IF-frequency in the receiver and to digitally down-convert in the back-end via the Nyquist-Shannon sampling theorem. This is relatively cheap and has become more feasible with an increased presence of high-frequency circuit-boards on the market.

BVEX will be using the Xilinx RFSoC 4x2 as an IF-backend. This board samples at a maximum of 5 GHz which means it can handle a maximum bandwidth $\Delta\nu$ of 2.5 GHz. The highest frequency that the SubMiniature version A (SMA, not to be confused with the Sub-millimetre Array) connectors on this circuit board can take without significant attenuation is about 7.5 GHz. The BVEX receiver will receive signals from 21 to 23 GHz and will be an upper side-band receiver. With an LO frequency of 19 GHz, this will place the IF frequency at 2-4 GHz and will give fairly good image rejection as the lower side-band in this case runs from 15 to 17 GHz which is beyond the frequency range of the antenna.

Receiver Noise

The other main design consideration is the receiver noise-temperature, which for BVEX will ultimately determine the overall sensitivity. Each component in the receiver signal chain will contribute to the total noise temperature based on its individual noise properties. In order to compute the noise temperature of a signal chain containing components with noise temperature T_i and linear gain G_i we use the Friis noise-equation given by

$$T_{tot} = T_0 + \frac{T_1}{G_0} + \frac{T_2}{G_0 G_1} + \frac{T_3}{G_0 G_1 G_2} + \cdots \tag{5.8}$$

where T_0 and G_0 are the noise temperature and gain of the first component in the signal chain, T_1 and G_1 are the noise temperature and gain of the second component continuing all the way to the last component. This means that the receiver noise will be dominated by all components up to and including the first amplifier. At the same time lossy components don't only contribute to the overall noise budget but also increase the noise contribution of all following components. It is therefore important that we amplify as early in the signal chain as possible to keep losses in front of the amplifier minimal. The noise contribution of any amplifier is given by the noise figure defined as

$$NF(\mathrm{dB}) = 10 \log \left(\frac{T_n + T_0}{T_0} \right) \tag{5.9}$$

where T_n is the noise temperature and T_0 is set at 290 K. Therefore, an amplifier with a 3 dB noise figure will have a noise temperature of about 290 K. For components that attenuate the signal the noise temperature is given by

$$T_n = (L - 1)T_{phys} \tag{5.10}$$

where $L = 1/G$ is the linear loss of the cable and T_{phys} is the physical temperature of the component. For high-frequency radio components the loss is generally high which is why they generally have to be cooled to keep the noise temperature low. However, BVEX operates at K-band where the losses still are low enough to operate at ambient temperatures.

All in all, it is important to keep the amplifier noise low, which is why BVEX will be using two low-gain and low noise amplifiers, rather than one high-gain amplifier which will have a higher noise figure. Furthermore, it is also important to keep losses at a minimum before the amplifier to avoid increasing the noise contribution of the amplifier itself. The K-band receiver for BVEX will therefore be split up into two stages, the amplification stage (containing all the components before the mixer in Fig. 5.4) and the mixing stage (containing all the components after the mixer in Fig. 5.4). The amplification stage will be located right behind the antenna feed to minimize losses. After amplification the signal will then be passed through a transmission line leading to the mixing chain which is located inside a pressure vessel for reasons of local oscillator stability.

The Final Receiver Design

A high-level schematic of the receiver diagram for BVEX can be seen in Fig. 5.6 (with preliminary CAD models in Fig. 5.7). The receiver is split into two stages, an amplification stage and a down-conversion stage. The amplification stage will be located behind the antenna feed to minimize losses and hence the noise leading up to the first 25 dB LNA. The down-conversion stage will be located inside a room-temperature pressure vessel in order to keep the local oscillator stable in low pressure atmospheric environments. For mechanical and vibrational reasons the pressure vessel cannot be mounted behind the antenna feed and hence will be connected to the amplification stage via a long transmission line somewhere on the gondola.

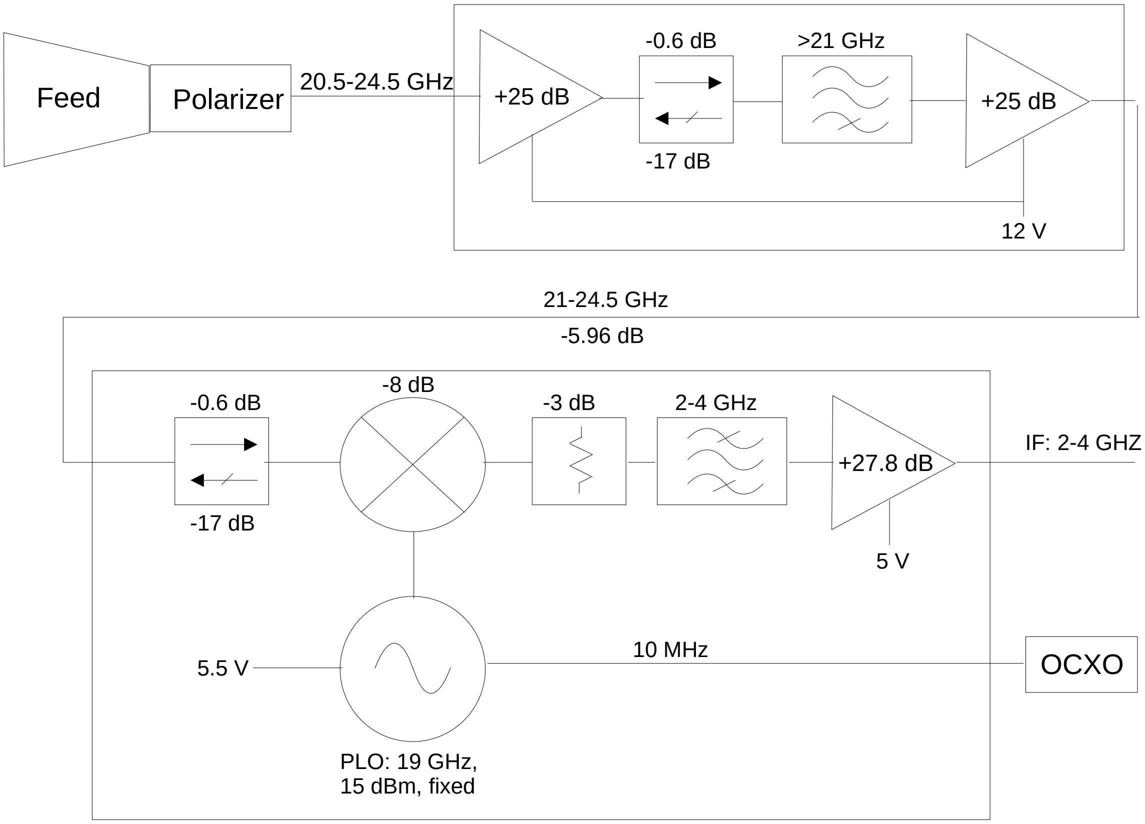

Figure 5.6: High-level block diagram of the BVEX K-band receiver. Not all losses are shown in this diagram for formatting purposes, the overall gain of the receiver is expected to be about 54 dB. The receiver is split up into two stages, amplification and down-conversion. The amplification stage will be located behind the antenna feed to minimize losses in front of the first amplifier. The mixing stage will be located inside a pressure vessel to keep the mixer and local oscillator stable. The isolators and attenuator were added to attenuate RF-filter reflections and to reduce local oscillator leakage back into the RF signal chain.

The antenna (a 36 inch Mi-Wave 223K-36/.396/595 Cassegrain dish) will be most sensitive to frequencies ranging from 20.5 to 24.5 which after entering the polarizer reach the first 25 dB LNA. Then the signals are high-passed at 21 GHz to ensure a clean response and image rejection. After this, the signals are amplified by another 25 dB LNA. The purpose of this dual amplification scheme was to again minimize the addition of noise as described by Eq. 5.8. While higher gain commercial-off-the-shelf (COTS) LNA's are available they often also have a higher noise figure, it hence is more favorable to gradually amplify the signal.

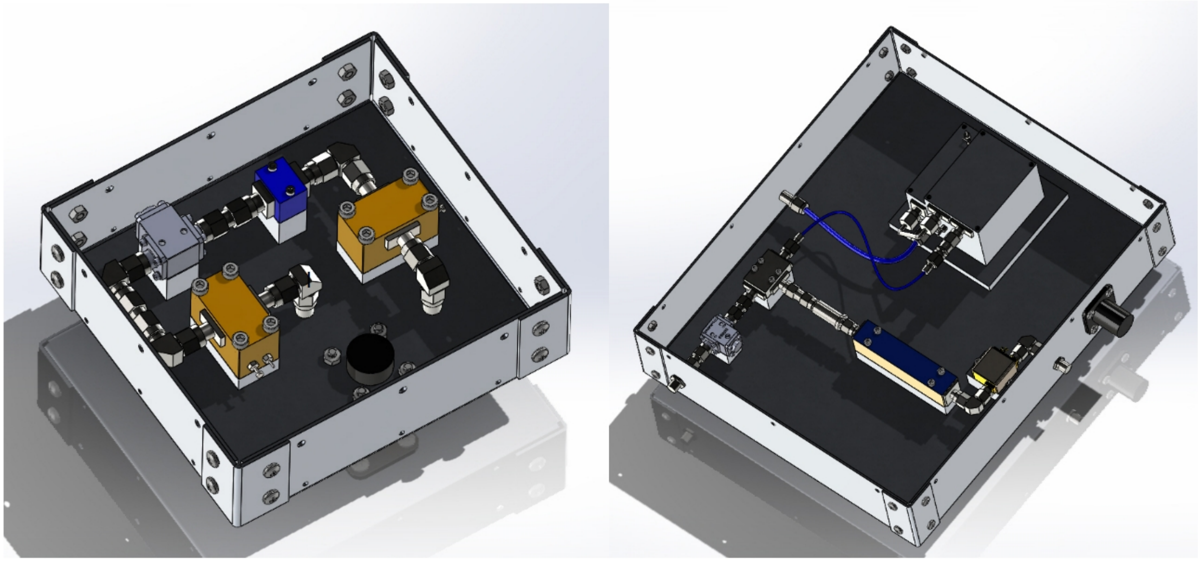

Figure 5.7: CAD models of the boxes containing the receiver electronics, for both the amplification stage (*Left*) that will be located behind the telescope feed and the mixing chain (*Right*)which will be located inside a pressure vessel. Power distribution circuits are not shown.

After the amplification stage the signal (now running from 21-24.5 GHz is injected into the down-conversion stage and is mixed with a 19 GHz signal from a phase-locked local oscillator. Unlike more conventional voltage-controlled local oscillators where the output frequency is controlled by an applied control voltage, phase-locked local oscillators use a reference signal to produce the RF output improving the overall phase-stability. In this case the reference will be a 10 MHz signal provided by a Rakon RK-409 oven-cooled crystal oscillator (OCXO). Following the mixer the signal will range from 2-5.5 GHz, therefore, to limit the bandwidth to 2 GHz for sampling at 4 GHz, the signal is then injected into a 2-4 GHz bandpass making the receiver only sensitive to signals ranging from 21-23 GHz. Finally, the signal is amplified once more to make up for lost signal and to bring the output RMS voltage of the receiver well above the RFSoC least-significant-bit voltage of 60 μV. In order to minimize the effect of reflections at both the IF and RF filter an attenuator and isolator was included respectively. A second isolator was placed at the RF port of the mixer to improve LO-RF isolation (i.e. to prevent local oscillator leakage back into the amplification stage). A breakdown of all the major receiver components can be seen in Tbl. 5.3.

Component	Manufacturer and P/N	Specifications
25 dB Low Noise Amplifier	Erzia ERZ-LNA-2100-2700-25-2	NF: 2 dB
21 GHz High-pass	Minicircuits ZHSS-K21G+	Loss: 1 dB
Mixer	Fairview Microwave FMMX1030	13 dBm LO, Loss: 9 dB
19 GHz Local Oscillator	Luff Research PLDRO 19000-10	Power: +15 dBm
2-4 GHz Bandpass	Minicircuits ZBSS-3G-S+	Loss: 1.5 dB
27.8 dB IF amplifier	Minicircuits ZX60-63GLN+	NF: 0.8 dB

Table 5.3: Specifications and part numbers of all the major BVEX receiver components.

Overall the BVEX K-band receiver is expected to have a total gain of 54 dB. In order to estimate the receiver noise-temperature we assume that the down-conversion stage inside the pressure vessel is kept at room-temperature and the amplification stage is kept at a temperature of 258 K (-15 °C). This was (conservatively) assumed to be the average temperature experienced by the amplifiers in the stratosphere, however it is not yet known how realistic this assumption may be and in how far regulating the frontend at this temperature is possible given that the temperatures on a stratospheric balloon can drop as low as -50 °C. This is something that will have to be investigated using thermal modelling software on designs of the complete radio telescope in the future to make a more accurate assumption. Nonetheless under the above assumptions the total receiver noise temperature is expected to be about 367 K, which is well within the requirements outlined in Tbl. 5.2. For instance, one possible target for BVEX will be 3C 454.3 due to its night-time availablity in the late summer from the Northern hemisphere. The upper-bound on the receiver temperature for this quasar is 9.6×10^4 using the GBT and 2.5×10^3 K using a VLBA station. The BVEX receiver temperature is orders of magnitude below these estimates and we therefore are extremely flexible with our choice of a partner station.

5.3 Future Work

In this chapter we have restricted ourselves to receiver designs and requirements for BVEX. The next logical step will be to characterize each of the receiver components that is determine/verify its gain, noise temperature and if applicable its phase noise properties, and finally to assemble the receiver components and test the entire signal chain. An unknown quantity in the sensitivity calculations presented in this section is spillover, i.e. noise contribution due to the side-lobes of the dish. It is therefore important to determine the power-pattern of the BVEX radio dish.

In order to test position tracking BVEXtracker, a piggy-back sensor package containing a GPS unit, accelerometer, gyroscope, magnetometer and IMU unit will be flown in the

Summer of 2023 to characterize the vibrational environment of a balloon gondola and to determine the ability to reconstruct position and velocity. This experiment still requires the proper implementation of a post-flight position reconstruction pipeline as well as some sort of simulator to test this pipeline for bugs. Together with ground-based tests of the radio telescope this will make a strong basis when applying for VLBI-related telescope time with the GBT or VLBA.

On top of all the aspects related to the radio telescope there is a variety of key systems that still have to be designed for BVEX. The first one being the elevation mount, since the Canadian Space Agency will be responsible for azimuthal pointing we require an elevation mount for the radio dish. The design process for this has already begun but will still require iteration on vibrational, thermal and mechanical properties. Secondly, systems like thermal control, pointing control as well as data storage and power distribution still need to be worked out, together with the implementation of flight software.

Chapter 6

Conclusions: A View Into the Future

Modern day astrophysics requires us to not only study the universe in a multi- wavelength manner but also in a multi-scale manner we therefore have to make use of both single dish telescopes as well as interferometers to get a complete picture. This is especially important for star-formation which is a process happening on all spatial scales, from giant molecular clouds down to protostellar and protoplanetary disks. In this work I have discussed two experiments, TolTEC which traces intermediate length scales and BVEX which will be a proof of concept for observing the smallest scales. For TolTEC I have designed possible observing strategies for the TolTEC Fields in Filaments survey using TolTEC simulations. I have also studied the loss of spatial scales due to atmospheric removal for both TolTEC simulations and observations using Fourier analysis. For BVEX, I have demonstrated that it is possible to design a receiver made up of commercial off-the-shelf components that can be used for K-band VLBI of bright calibrators on a balloon-borne platform.

Once TolTEC has completed commissioning, it will be one of the most powerful millimetre-wave instruments, with its 4 arcminute field-of-view and resolution of up to $5''$. Its polarization capabilities will be unprecedented compared to current instruments like POL-2 on the JCMT and NIKA-2 on the IRAM 30m telescope, due to its ability to fill in spatial scales between Planck and ALMA. These properties make it an ideal instrument to map the cold filamentary structures of the ISM which are sites of active star formation, at high resolution and sub-parsec scales. The 100 h Fields in Filaments survey will provide much needed legacy data that will serve as a basis for star-formation and ISM science to the entire community. While the trend in millimetre and sub-millimetre astronomy has been to continuously improve VLBI, an experiment like TolTEC clearly demonstrates that the era of single dish astronomy has not come to an end yet, and that there is still a necessity for these kinds of experiments.

Unlike TolTEC which is an instrument that was built to deliver science-ready data products, BVEX will be a proof of concept and prototype for future instruments. While TolTEC is a single-dish experiment, BVEX will aim to perform VLBI from the stratosphere, with the ultimate goal to demonstrate the detection of fringes at K-band. BVEX will make an excellent case for building a future millimetre balloon-borne VLBI station that could serve as an outrigger station for the EHT, filling in parts of the uv-space that were previously inaccessible but also improve the sensitivity of EHT observations. The balloon-borne platform is also an excellent laboratory for testing the space-readiness of technology due to the near-space conditions of the stratosphere. As is the case with many balloon-missions, future versions of BVEX apart from delivering high-resolution science, will therefore also serve as prototypes for achieving space VLBI.

Bibliography

Agudo, I. et al. (2012). "3C 286: a bright, compact, stable, and highly polarized calibrator for millimeter-wavelength observations". In: *Astronomy and Astrophysics* 541, A111. DOI: `10.1051/0004-6361/201218801`. URL: `https://doi.org/10.1051/0004-6361/201218801`.

Andersson, B. -G. et al. (Aug. 2015). "Interstellar Dust Grain Alignment". In: *Annual Review of Astronomy and Astrophysics* 53, pp. 501–539. DOI: `10.1146/annurev-astro-082214-122414`.

André, P. et al. (Jan. 2014). "From Filamentary Networks to Dense Cores in Molecular Clouds: Toward a New Paradigm for Star Formation". In: *Protostars and Planets VI*. Ed. by Henrik Beuther et al., pp. 27–51. DOI: `10.2458/azu_uapress_9780816531240-ch002`. arXiv: `1312.6232 [astro-ph.GA]`.

Arzoumanian, D. et al. (Mar. 2021). "Dust polarized emission observations of NGC 6334. BISTRO reveals the details of the complex but organized magnetic field structure of the high-mass star-forming hub-filament network". In: *Astronomy and Astrophysics* 647, A78, A78. DOI: `10.1051/0004-6361/202038624`. arXiv: `2012.13060 [astro-ph.GA]`.

Betti, S. K. et al. (Dec. 2021). “The Robustness of Synthetic Observations in Producing Observed Core Properties: Predictions for the TolTEC Clouds to Cores Legacy Survey”. In: *The Astrophysical Journal* 923.1, 25, p. 25. DOI: `10.3847/1538-4357/ac2666`. arXiv: `2109.06916 [astro-ph.GA]`.

Bij, Akanksha (2022). “The Interplay Between Magnetic Fields and Stellar Feedback in RCW 36”. English. Copyright - Database copyright ProQuest LLC; ProQuest does not claim copyright in the individual underlying works; Last updated - 2023-03-06. PhD thesis, p. 158. ISBN: 9798371935632. URL: `https://proxy.queensu.ca/login?url=https://www.proquest.com/dissertations-theses/interplay-between-magnetic-fields-stellar/docview/2778644490/se-2`.

Catalano, A. et al. (Sept. 2014). “Performance and calibration of the NIKA camera at the IRAM 30 m telescope”. In: *Astronomy and Astrophysics* 569, A9, A9. DOI: `10.1051/0004-6361/201423557`. arXiv: `1402.0260 [astro-ph.IM]`.

CCAT-Prime Collaboration (Jan. 2023). “CCAT-prime Collaboration: Science Goals and Forecasts with Prime-Cam on the Fred Young Submillimeter Telescope”. In: *The Astrophysical Journal Supplement* 264.1, 7, p. 7. DOI: `10.3847/1538-4365/ac9838`. arXiv: `2107.10364 [astro-ph.CO]`.

Choi, S. K. et al. (Mar. 2020). “Sensitivity of the Prime-Cam Instrument on the CCAT-Prime Telescope”. In: *Journal of Low Temperature Physics* 199.3-4, pp. 1089–1097. DOI: `10.1007/s10909-020-02428-z`. arXiv: `1908.10451 [astro-ph.IM]`.

Condon, J. J. et al. (2016). *Essential Radio Astronomy*. ISBN: 9780691137797. URL: `http://www.jstor.org/stable/j.ctv5vdcww`.

Crutcher, Richard M. (Sept. 2012). "Magnetic Fields in Molecular Clouds". In: *Annual Review of Astronomy and Astrophysics* 50, pp. 29–63. DOI: `10.1146/annurev-astro-081811-125514`.

Crutcher, Richard M. et al. (Dec. 2010). "Magnetic Fields in Interstellar Clouds from Zeeman Observations: Inference of Total Field Strengths by Bayesian Analysis". In: *The Astrophysical Journal* 725.1, pp. 466–479. DOI: `10.1088/0004-637X/725/1/466`.

Dirienzo, William J. et al. (Nov. 2015). "Physical Conditions of the Earliest Phases of Massive Star Formation: Single-dish and Interferometric Observations of Ammonia and CCS in Infrared Dark Clouds". In: *The Astronomical Journal* 150.5, 159, p. 159. DOI: `10.1088/0004-6256/150/5/159`. arXiv: `1508.01700 [astro-ph.GA]`.

Event Horizon Telescope Collaboration (Apr. 2019). "First M87 Event Horizon Telescope Results. I. The Shadow of the Supermassive Black Hole". In: *The Astrophysical Journal Letters* 875.1, L1, p. L1. DOI: `10.3847/2041-8213/ab0ec7`. arXiv: `1906.11238 [astro-ph.GA]`.

— (May 2022). "First Sagittarius A* Event Horizon Telescope Results. I. The Shadow of the Supermassive Black Hole in the Center of the Milky Way". In: *The Astrophysical Journal Letters* 930.2, L12, p. L12. DOI: `10.3847/2041-8213/ac6674`.

Federrath, Christoph (July 2015). "Inefficient star formation through turbulence, magnetic fields and feedback". In: *Monthly Notices of the Royal Astronomical Society* 450.4, pp. 4035–4042. DOI: `10.1093/mnras/stv941`. arXiv: `1504.03690 [astro-ph.SR]`.

Finger-Camus, Ricardo Alberto (Jan. 2013). "Design and construction of a digital sideband separating spectrometer for the 1.2-meter southern radio telescope". PhD thesis. University of Chile.

Fissel, L. M. (Dec. 2013). “Probing the Role Played by Magnetic Fields in Star Formation with BLASTPol”. PhD thesis. University of Toronto, Canada.

Fissel, L. M. et al. (June 2019). “Relative Alignment between the Magnetic Field and Molecular Gas Structure in the Vela C Giant Molecular Cloud Using Low- and High-density Tracers”. In: *The Astrophysical Journal* 878.2, 110, p. 110. DOI: `10.3847/1538-4357/ab1eb0`. arXiv: `1804.08979 [astro-ph.GA]`.

Fissel et al. (June 2016). “Balloon-Borne Submillimeter Polarimetry of the Vela C Molecular Cloud: Systematic Dependence of Polarization Fraction on Column Density and Local Polarization-Angle Dispersion”. In: *The Astrophysical Journal* 824.2, 134, p. 134. DOI: `10.3847/0004-637X/824/2/134`. arXiv: `1509.05298 [astro-ph.GA]`.

Hensley, Brandon S. et al. (May 2023). “The Astrodust+PAH Model: A Unified Description of the Extinction, Emission, and Polarization from Dust in the Diffuse Interstellar Medium”. In: *The Astrophysical Journal* 948.1, 55, p. 55. DOI: `10.3847/1538-4357/acc4c2`. arXiv: `2208.12365 [astro-ph.GA]`.

Hoffman, Melissa et al. (Sept. 2018). *Correcting ALMA 12-m Array Data for Missing Short Spacings Using the Green Bank Telescope*. Green Bank Telescope Memorandum 300, North American ALMA Science Center Memo 116, September 28, 2018, 17 pages.

Holland, W. S. et al. (Apr. 2013). “SCUBA-2: the 10 000 pixel bolometer camera on the James Clerk Maxwell Telescope”. In: *Monthly Notices of the Royal Astronomical Society* 430.4, pp. 2513–2533. DOI: `10.1093/mnras/sts612`. arXiv: `1301.3650 [astro-ph.IM]`.

Irfan, Melis O. et al. (Feb. 2023). “MeerKLASS simulations: Mitigating 1/f noise for auto-correlation intensity mapping measurements”. In: *arXiv e-prints*, arXiv:2302.02683, arXiv:2302.02683. DOI: `10.48550/arXiv.2302.02683`. arXiv: `2302.02683 [astro-ph.CO]`.

Johnson, Michael et al. (Sept. 2019). “Studying black holes on horizon scales with space-VLBI”. In: *Bulletin of the American Astronomical Society*. Vol. 51, 235, p. 235. DOI: `10.48550/arXiv.1909.01405`. arXiv: `1909.01405 [astro-ph.IM]`.

Kennicutt Robert C., Jr. (Sept. 1989). “The Star Formation Law in Galactic Disks”. In: *The Astrophysical Journal* 344, p. 685. DOI: `10.1086/167834`.

Kovács, Attila (July 2008). “Scanning strategies for imaging arrays”. In: *Millimeter and Submillimeter Detectors and Instrumentation for Astronomy IV*. Ed. by William D. Duncan et al. Vol. 7020. Society of Photo-Optical Instrumentation Engineers (SPIE) Conference Series, 702007, p. 702007. DOI: `10.1117/12.790272`. arXiv: `0806.4888 [astro-ph]`.

Krumholz, Mark R. et al. (Jan. 2012). “A Universal, Local Star Formation Law in Galactic Clouds, nearby Galaxies, High-redshift Disks, and Starbursts”. In: *The Astrophysical Journal* 745.1, 69, p. 69. DOI: `10.1088/0004-637X/745/1/69`. arXiv: `1109.4150 [astro-ph.CO]`.

Lazarian, A. (July 2007). “Tracing magnetic fields with aligned grains”. In: *Journal of Quantitative Spectroscopy and Radiative Transfer* 106, pp. 225–256. DOI: `10.1016/j.jqsrt.2007.01.038`. arXiv: `0707.0858 [astro-ph]`.

Lee, Dennis et al. (Aug. 2022). “The TolTEC camera: polarimetric commissioning and performance of the continuously rotating half-wave plate”. In: *Millimeter, Submillimeter, and Far-Infrared Detectors and Instrumentation for Astronomy XI*. Ed. by Jonas Zmuidzinas et al. Vol. 12190. Society of Photo-Optical Instrumentation Engineers (SPIE) Conference Series, 121901O, 121901O. DOI: `10.1117/12.2627725`.

Li, Pak Shing et al. (June 2019). “Magnetized interstellar molecular clouds - II. The large-scale structure and dynamics of filamentary molecular clouds”. In: *Monthly Notices of the*

Royal Astronomical Society 485.4, pp. 4509–4528. DOI: `10.1093/mnras/stz653`. arXiv: `1901.04593 [astro-ph.GA]`.

Lunde, Emily et al. (Dec. 2020). “The optical design and performance of TolTEC: a millimeter-wave imaging polarimeter”. In: *Society of Photo-Optical Instrumentation Engineers (SPIE) Conference Series*. Vol. 11453. Society of Photo-Optical Instrumentation Engineers (SPIE) Conference Series, 114534A, 114534A. DOI: `10.1117/12.2562798`.

Ma, Zhiyuan (2022). *TolTEC Passband Data*. Version V1. DOI: `10.5072/FK2/UKYHBX`. URL: `https://doi.org/10.5072/FK2/UKYHBX`.

Ma, Zhiyuan et al. (Dec. 2020). “The TolTEC data analysis pipeline and software stack”. In: *Society of Photo-Optical Instrumentation Engineers (SPIE) Conference Series*. Vol. 11452. Society of Photo-Optical Instrumentation Engineers (SPIE) Conference Series, 114522O, 114522O. DOI: `10.1117/12.2560735`.

McCrackan, Michael et al. (Aug. 2022). “The TolTEC camera: the citlali data reduction pipeline engine”. In: *Society of Photo-Optical Instrumentation Engineers (SPIE) Conference Series*. Vol. 12189. Society of Photo-Optical Instrumentation Engineers (SPIE) Conference Series, 121891H, 121891H. DOI: `10.1117/12.2629095`.

Nakamura, Fumitaka et al. (Nov. 2008). “Magnetically Regulated Star Formation in Three Dimensions: The Case of the Taurus Molecular Cloud Complex”. In: *The Astrophysical Journal* 687.1, pp. 354–375. DOI: `10.1086/591641`. arXiv: `0804.4201 [astro-ph]`.

Novak, G. et al. (Feb. 1989). “A 100-micron Polarimeter for the Kuiper Airborne Observatory”. In: *Publications of the Astronomical Society of the Pacific* 101, p. 215. DOI: `10.1086/132425`.

Pascale et al., E. (Sept. 2012). "The balloon-borne large-aperture submillimeter telescope for polarimetry-BLASTPol: performance and results from the 2010 Antarctic flight". In: *Ground-based and Airborne Telescopes IV*. Ed. by Larry M. Stepp et al. Vol. 8444. Society of Photo-Optical Instrumentation Engineers (SPIE) Conference Series, 844415, p. 844415. DOI: `10.1117/12.927211`.

Perley, R. A. et al. (June 2013). "Integrated Polarization Properties of 3C48, 3C138, 3C147, and 3C286". In: *The Astrophysical Journal Supplement* 206.2, 16, p. 16. DOI: `10.1088/0067-0049/206/2/16`. arXiv: `1302.6662 [astro-ph.IM]`.

Pineda, Jaime E. et al. (May 2022). "From Bubbles and Filaments to Cores and Disks: Gas Gathering and Growth of Structure Leading to the Formation of Stellar Systems". In: *arXiv e-prints*, arXiv:2205.03935, arXiv:2205.03935. DOI: `10.48550/arXiv.2205.03935`. arXiv: `2205.03935 [astro-ph.GA]`.

Planck Collaboration (Sept. 2016a). "Planck 2015 results. I. Overview of products and scientific results". In: *Astronomy and Astrophysics* 594, A1, A1. DOI: `10.1051/0004-6361/201527101`. arXiv: `1502.01582 [astro-ph.CO]`.

— (Dec. 2016b). "Planck intermediate results. XL. The Sunyaev-Zeldovich signal from the Virgo cluster". In: *Astronomy and Astrophysics* 596, A101, A101. DOI: `10.1051/0004-6361/201527743`. arXiv: `1511.05156 [astro-ph.CO]`.

— (Feb. 2016c). "Planck intermediate results. XXXV. Probing the role of the magnetic field in the formation of structure in molecular clouds". In: *Astronomy and Astrophysics* 586, A138, A138. DOI: `10.1051/0004-6361/201525896`. arXiv: `1502.04123 [astro-ph.GA]`.

— (Sept. 2020). “Planck 2018 results. XII. Galactic astrophysics using polarized dust emission”. In: *Astronomy and Astrophysics* 641, A12, A12. DOI: `10.1051/0004-6361/201833885`. arXiv: `1807.06212 [astro-ph.GA]`.

Qian, Lei et al. (Sept. 2015). “A New Method for Constraining Molecular Cloud Thickness: A Study of Taurus, Perseus, and Ophiuchus”. In: *The Astrophysical Journal* 811.1, 71, p. 71. DOI: `10.1088/0004-637X/811/1/71`. arXiv: `1508.04220 [astro-ph.GA]`.

Ritacco, A. et al. (Aug. 2018). “NIKA 150 GHz polarization observations of the Crab nebula and its spectral energy distribution”. In: *Astronomy and Astrophysics* 616, A35, A35. DOI: `10.1051/0004-6361/201731551`. arXiv: `1804.09581 [astro-ph.CO]`.

Roy, A. et al. (Feb. 2014). “Reconstructing the density and temperature structure of prestellar cores from Herschel data: A case study for B68 and L1689B”. In: *Astronomy and Astrophysics* 562, A138, A138. DOI: `10.1051/0004-6361/201322236`. arXiv: `1311.5086 [astro-ph.GA]`.

Simard-Normandin, M. et al. (Nov. 1980). “Rotation measures and the galactic magnetic field.” In: *The Astrophysical Journal* 242, pp. 74–94. DOI: `10.1086/158445`.

Tahani, M. et al. (June 2018). “Helical magnetic fields in molecular clouds?. A new method to determine the line-of-sight magnetic field structure in molecular clouds”. In: *Astronomy and Astrophysics* 614, A100, A100. DOI: `10.1051/0004-6361/201732219`. arXiv: `1802.07831 [astro-ph.GA]`.

Thompson, A. Richard et al. (2017). *Interferometry and Synthesis in Radio Astronomy, 3rd Edition*. DOI: `10.1007/978-3-319-44431-4`.